Sputter Deposition Synthesis and Characterization of Thin Films: Amorphous Carbon and TiNi Shape Memory Alloys

By

Dujiang Wan

B.E. (Tsinghua University, P. R. China) 1990
M.E. (Tsinghua University, P. R. China) 1993

A dissertation submitted in partial satisfaction of the

requirements for the degree of

Doctor of Philosophy

in

Engineering-Mechanical Engineering

in the

GRADUATE DIVISION

of the

UNIVERSITY OF CALIFORNIA, BERKELEY

Committee in charge:

Professor Kyriakos Komvopoulos, Chair
Professor David B. Bogy
Professor Ronald Gronsky

Fall 2004

The dissertation of Dujiang Wan is approved:

Chair Date

Date

Date

University of California, Berkeley

Fall 2004

Sputter Deposition Synthesis and Characterization of Thin Films:
Amorphous Carbon and TiNi Shape Memory Alloys

Copyright © 2004

By

Dujiang Wan

To my parents, ***Zhong Wan*** & ***Mingxia Yin***

my wife, ***Yalin Tang***

and

my son, ***Eric***

ACKNOWLEDGMENTS

This work is largely a product of the interest and effort of my research advisor, Professor Kyriakos Komvopoulos. I would like to thank Professor K. Komvopoulos for his academic guidance, financial support, and all opportunities he has given me throughout my graduate study at University of California at Berkeley.

I am also grateful to Professor David B. Bogy for his sitting on my dissertation committee. Many thanks to Professor Ronald Gronsky for his sitting on my dissertation committee and lots of suggestions in the field of transmission electron microscopy (TEM) technique, and his class in TEM. He also helped me to improve my dissertation in English.

I like to thank Professor Lisa A. Pruitt, Professor David A. Dornfeld, Professor Arunava Majumdar, and Professor Constance Chang-Hasnain for their assistance in my academic progress. My thanks go to Professor Timothy D. Sands for his class in thin film sciences and technology, and Professor Michael A. Lieberman for his class in weakly ionized plasma. I also like to thank Professor Ted Bennett in University of California at Santa Barbara who opened a new world to me.

I like to thank Dr. Wei Lu for training me how to run the sputtering system, and how to do nano-tribology tests. We had a lot of discussions about carbon films and nano-tribology. Many thanks also go to Dr. Christian Kisielowski, Mr. ChengYu Song, Dr. Weiqiang Han, and my friend Xiayu Xu from the Lawrence Berkeley National Laboratory for training me how to prepare TEM samples , how to use high resolution

transmission electron microscope, and how to do EELS analysis, and Dr. Ji Zhu for training me how to use XPS.

Thanks also go to my fellow graduate students and friends, Ning Ye, Phil Mai, Jian Yan, Rui Xu, Zhongqing Gong, Yong Liu, Lei Yuan, Jianfeng Luo, Deyu Li, Yang Zhao, Jin Zhou, Rong Fan, to list just a few, who helped define my graduate experience, and let my graduate life at Berkeley much enjoyable. My best wishes to the next generation of our lab.

It is my pleasure to thank my parents in China for their patience, encouragement and support. It is not easy to survive from the graduate school of University of California at Berkeley. I really appreciate my wife Yalin Tang for her incredible dedication and support. I like to thank my baby Eric who will come to the World in next March. He gives me great hope for future.

This research was supported by the Surface Engineering and Tribology Program of the Nation Science Foundation, the Computer Mechanics Laboratory at the University of California at Berkeley, and the National Center for Electron Microscopy at the Lawrence Berkeley National Laboratory.

TABLE OF CONTENTS

LIST OF FIGURES

Chapter 2

Chapter 4

Chapter 5

Chapter 6

Chapter 7

Chapter 8

LIST OF TABLES

Chapter 3

Chapter 4

Chapter 5

Chapter 6

CHAPTER 1

Introduction

Carbon is of both scientific and practical significance since it can exist in three different bonding configurations, i.e., tetrahedral (sp^3), trigonal (sp^2), and linear (sp^1), and it may form various crystalline and disordered structures. The most common carbon crystalline allotropes are graphite (stable phase) (Kelly, 1981) and diamond (metastable phase) (Field, 1993). The development of diamondlike carbon (DLC) films and the discoveries of ball-shaped C_{60} (Rohlfing, et al, 1984) and carbon nanotubes (Iijima, 1991) have made new progress in the science of carbon over the past two decades.

Diamondlike carbon containing a significant fraction of sp^3 bonds is a metastable form of amorphous carbon (*a*-C). Since the synthesis of DLC films by ion beam deposition (Aisenberg and Chabot, 1971), numerous techniques have been developed to produce DLC films with properties varying between those of the two most common carbon allotropes – graphite and diamond. When used as protective coatings DLC films exhibit excellent mechanical and tribological properties, such as high hardness, low friction coefficient, and high wear resistance (Lu and Komvopoulos, 1999, 2001; Ma, et al, 2003) and have resulted in intensive studies largely due to their desirable properties (Tsai and Bogy, 1987; Lifshitz, 1997; Robertson, 2002). An important characteristic of DLC films is the sp^3 carbon content, which depends strongly on the deposition technique and associated conditions. Nonhydrogenated *a*-C films with sp^3 content greater than 50 at.%, referred to as tetrahedral amorphous carbon (*ta*-C) films (McKenzie, 1996), can be produced from energetic carbon ions using different techniques, such as mass-selected

ion beam (MSIB) deposition (Ishikawa, et al, 1987; Lifshitz, et al, 1990; Lifshitz, et al 1997), filtered cathodic vacuum arc (FCVA) deposition (McKenzie, et al, 1991; Fallon, et al, 1993; Jungnickel, et al, 1994; Silva, et al, 1996), and laser ablation (Kovarik, et al, 1993). The precursors of film formation are carbon ions with high kinetic energy (hundreds of eV to keV). The sp^3 hybridization in *ta*-C films due to the bombardment of energetic carbon ions is a physical process that can be explained by the subplantation model (Lifshitz, Kasi and Rabalais, 1989; Lifshitz, et al, 1990; Robertson, 1994, 1996; Hofsäss, et al, 1998).

Sputtering techniques are widely used to produce different kinds of thin films with thickness ranging from a few nanometers to a few micrometers. The properties of thin films are strongly affected by the plasma conditions of the particular sputter deposition processes. The low-pressure radio-frequency (rf) sputtering technique is an efficient technique to synthesize *a*-C films, and offers some advantages to control the film properties. Less gas is incorporated into the film due to the high vacuum base pressure ($< 10^{-6}$ Torr) and the low pressure (several mTorr) both used before and during film growth. Contamination is also easily controlled because of the high vacuum conditions employed. Relatively low film growth rates are beneficial to the uniformity of the film thickness and surfaces smoothness. Ion bombardment of the growing film surface and adjustment of the substrate temperature offer control over the film properties. Hydrogen-free carbon films with sp^3 contents as high as ~ 50 at.% can be produced from low-pressure rf sputtering under optimum process conditions. The precursors of film growth are neutral carbon atoms with low kinetic energy on the order of a few eV to tens eV, which are different from those used in the other film deposition techniques mentioned above. Therefore, the

mechanism of sp^3 hybridization in *a*-C films synthesized by rf sputtering is different from the subplantation process. This is substantiated by the results of the present study.

In this work, *a*-C films are synthesized by rf sputtering under different deposition conditions, and the effects of plasma conditions on the film growth and surface topography are explored by transmission electron microscopy (TEM) and atomic force microscopy (AFM). The microstructures of the rf sputtered *a*-C films are studied by TEM and X-ray photoelectron spectroscopy (XPS). The compressive residual stresses in rf sputtered *a*-C films are also systematically investigated. Based on the experimental results, a mechanism of sp^3 hybridization in these *a*-C films is discussed.

The most important parameters significantly affecting the properties of rf sputtered *a*-C films are ion current density, ion kinetic energy, and sputter yield. The effects of process conditions, such as rf power, substrate bias voltage, working pressure and gas flow rate, on low-pressure rf discharge are described in Chapter 2, and a relationship for the ion current density is derived from energy balance considerations. In Chapter 3, the sputter deposition process is discussed, and a linear relationship between *a*-C film thickness and the product of sputtering rate and deposition time is obtained. The development of *a*-C film surface topography is studied by AFM, and the effects of film growth rate and ion bombardment on the growing film surface are discussed.

A common feature in *ta*-C or *a*-C films is the relatively high compressive residual stress. Experiments were conducted to study the effect of compressive residual stress on the tribological performance of *a*-C films deposited by magnetron sputtering (Mounier, et al, 1995; Mounier and Pauleau, 1997). In Chapter 4, the compressive residual stresses in rf sputtered *a*-C films are studied. The stress levels are evaluated using Stoney's equation

by measuring the wafer curvature before and after film deposition. Ion bombardment effects on the stress levels and the stress relaxation mechanisms such as thermal spikes and interfacial tension effect are discussed.

Transmission electron microscopy is a powerful technique for investigating the microstructure of thin films. TEM and analytical electron microscopy (AEM) are used to explore the microstructure of rf sputtered *a*-C films in Chapter 5. High-resolution cross-sectional transmission electron microscope images reveal a two-layer structure consisting of *a*-C film and an ultrathin interfacial layer (~ 35 Å in thickness), which differs from that of *ta*-C films synthesized by MSIB or FCVA deposition under much higher energetic carbon ion bombardment. The presence of a ~35 Å thick interfacial layer regardless of deposition conditions indicates that nucleation and initial growth of the *a*-C films are mainly controlled by the substrate surface condition. High-resolution cross-sectional transmission electron microscope images also reveal the presence of plate-like nanocrystallites (~35 Å in size) randomly distributed in *a*-C film and oriented with their {111} planes parallel to film surface. The possible mechanisms leading to the formation of these nanocrystalline structures are discussed.

Several experimental techniques have been used to study the microstructure in *a*-C films and related materials (Tsai and Bogy, 1987; Robertson, 1986, 2002). XPS offers surface chemical composition analysis (Chang, 1981; Briggs and Seah, 1983; Power and Seah, 1990), and has often been used to evaluate the relative concentrations of sp^2 and sp^3 sites (Schafer, et al, 1996; Ronning, et al, 1997). In Chapter 6, four series of rf sputtered *a*-C film surfaces are surveyed by a x-ray photoelectron spectroscope. C 1s core level photoelectron spectra are obtained by narrow scan XPS. The sp^3 contents in these *a*-C

films are inferred by decomposition of the C 1s core level photoelectron spectra. The effect of plasma conditions on the microstructures of the *a*-C films is discussed. The observed binding energy shift is explained in light of the compressive residual stresses in the *a*-C films.

In Chapter 7, an energetic particle collision analysis is proposed to explain the effect of ion bombardment on tetrahedral carbon hybridization (sp^3) in rf sputtered *a*-C films. The model is validated by TEM and electron energy loss spectroscopy (EELS) results that confirm the existence of a two-layer film structure consisting of an ultrathin interfacial layer and a continuous *a*-C film. Analytical results for the sp^3 carbon content in rf sputtered *a*-C films are in good agreement with similar experimental results obtained from the analysis of the C 1s photoelectron spectra.

Another research topic of this dissertation is the phase transformation phenomena occurring in sputtered TiNi shape-memory alloy (SAM) films. Since the discovery of the shape memory effect (SME) in binary titanium-nickel (TiNi) alloys (Buehler, Gilfrich and Wiley, 1963), significant attention has been devoted to SAM materials. Several applications of sputtered TiNi films can be found in Proceedings of the Shape Memory and Superelasticity Technology (SMST) from 1994 through 2003. Although the SME has been associated with a self-accommodation phase transformation, understanding of this phenomenon in nanometer-thick TiNi films is limited. Sputtered TiNi films of thickness in the range of 45-365 nm are prepared, and their phase transformation is investigated in light of electrical resistivity measurements obtained during thermal cycling in Chapter 8. The results are explained in terms of shear-like self-accommodation microstructure

changes, and the constrained phase transformation is attributed to the decrease of the film thickness.

Finally, the most important findings of the dissertation are summarized in Chapter 9.

CHAPTER 2

Effects of Sputtering Conditions on Low-Pressure RF Discharge

2.1 Introduction

Sputtering techniques are widely used to deposit thin films of thickness ranging from a few nanometers to hundreds of nanometers. Low-pressure radio-frequency (rf) discharge has been extensively studied both experimentally and theoretically (Koening and Maissel, 1970; Coburn and Kay, 1972; Keller and Pennebake, 1979; Köhler, et al, 1985; Köhler, Horne, and Coburn, 1985; Metze, Ernie and Oskam, 1986; Lieberman, 1988; Manenschijn, et al, 1991; Lieberman and Lichtenberg, 1994; Miller and Riley, 1997; Panagopoulos and Economou, 1999), and the dynamics of rf plasma sheaths have attracted significant attention due to their importance in various rf discharge applications. For all radio frequencies, there is a critical parameter, $\omega\tau_i$, that controls the ion modulation in the rf sheath, where ω is the frequency of the applied field, and τ_i is the ion transit time through the sheath. Neglecting the ion entering velocity (Bohm velocity) at the sheath edge and assuming a collisionless sheath, τ_i is given by (Panagopoulos and Economou, 1999)

$$\tau_i = 3S\sqrt{\frac{m_i}{2eV_{sh}}}, \tag{2-1}$$

where m_i is the ion mass, S and V_{sh} are the sheath thickness and sheath voltage, respectively, and e is the elementary charge. For low frequencies and/or short ion transit time ($\omega\tau_i << 1$), the variation of ion bombarding energies at both target and substrate surfaces follows the variation of the corresponding sheath voltages because the ions are

subjected to the sheath voltages occurring at the time they enter the sheaths. For high frequencies and/or long ion transit time ($\omega\tau_i >> 1$), the ions respond to time-average sheath voltages because they are subjected to various field oscillations during travel through the sheaths. In low-pressure Ar rf discharge (13.56 MHz), the ions respond only to time-average electrical fields because $\omega\tau_i >> 1$. The powers dissipated in the two electrode sheaths are the entire source of power that maintains the discharge during capacitive excitation, and the plasma bulk usually defines the boundary conditions of the sheath problem. Lieberman (1988) analyzed theoretically the capacitive rf sheath for time-independent, collisionless ion motion in the sheath and inertialess electrons ($\omega\tau_i >> 1$). The unique feature in Lieberman's model is the assumptions that the electron density is equal to the ion density at the sheath edges and zero at the electrodes. Metze et al. (1986) analyzed the sheath voltage waveforms using an equivalent circuit model of a plasma reactor for the transit time τ_i of ions through the sheath less than $1/f$, where f is the frequency of the applied voltage. In this model, the sheath thickness corresponds to the steady-state thickness related to the instantaneous voltage $V_{sh}(t)$ across the sheath. So this model is a quasi-steady-state model and is valid for frequency less than 1 MHz for Ar plasmas of ion density equal to 10^{10} cm^{-3}. Miller and Riley (1997) developed a semi-analytical model to connect both extremes.

In this chapter, A Perkin-Elmer Randex-2400 model sputtering system without magnetron shown schematically in Figure 2-1 is used to study the characteristics of low-pressure Ar rf discharge. The plasma is excited and maintained by a rf power supply through a rf coupling coil and capacitive tuning network (Figure 2-2). A bias voltage can be applied to the substrate by the substrate bias tuning technique. In low-pressure Ar rf

discharge, the target is negatively self-biased. Relationships including the rf power, substrate bias voltage, and target negative self-bias voltage are obtained for low-pressure Ar rf discharge. An expression for the ion current density is derived from energy balance considerations.

2.2 Experimental Procedures

The geometry configuration of the rf discharge in the Perkin-Elmer Randex-2400 model sputtering system is symmetric, the target surface area A_T is equal to the substrate area A_S, and the substrate is 200 mm in diameter. The spacing between the two electrodes (target and substrate) is fixed at 7 cm. During low-pressure Ar rf discharge, the temperatures of both target and substrate are maintained at room temperature by water cooling, the working pressure is set by adjusting the opening of a throttle valve (Figure 2-1), the gas flow rates are regulated by MKS flow ratio controllers, and the forward rf power generated by rf power supply is servo-stabilized in the range of 80 - 1000 W. The power that sustains the discharge is called absorbed rf power, which is usually not equal to the forward rf power due to the impedance mismatch between the rf power supply and the plasma. The power difference between them is called the reflected rf power, whose physical significance will be discussed in a later section. Both the forward and reflected rf powers are regulated during the low-pressure Ar rf discharge.

For low-pressure rf Ar gas discharge, the vacuum chamber is pumped down to a low base pressure ($< 2 \times 10^{-6}$ Torr) by a turbo molecular pump backed by a rotary mechanical pump to reduce the effects of residual air before introducing Ar gas into the chamber (Figure 2-1). The base pressure is measured by a Granville-Philips ion gauge.

During low-pressure Ar rf discharge, the substrate bias and target self-bias voltages are measured directly. The effects of forward rf power, substrate bias voltage, working pressure and Ar gas flow rate on the target self-bias voltage and ion current density are investigated experimentally and representative results are discussed in the following sections.

2.3 RF Power Dependence of Ion Current Density and Electrode Bias Potentials

Electrically, plasma sheaths generated in low-pressure rf discharge can be modeled as pure capacitors when $\omega\tau_i >> 1$, and the sheath behavior can be analyzed using an equivalent electrical circuit of the discharge (Koening and Maissel, 1970; Coburn and Kay, 1972; Keller and Pennebake, 1979; Köhler, et al, 1985; Köhler, Horne, and Coburn, 1985; Manenschijn, et al, 1991; Lieberman and Lichtenberg, 1994). For a parallel-plate capacitor, the capacitance C

$$C = \frac{\varepsilon_o \varepsilon_d A}{S}, \tag{2-2}$$

where ε_o is the electrical permittivity in vacuum (= 8.8542 x 10^{-12} F/m), ε_d is the dielectric constant of the capacitor medium, A is the plate area ($A = A_T = A_S = 324\,\text{cm}^2$ in the present sputtering system). For low-pressure rf discharge, ε_d is determined by the working gas, working pressure, and electrical power, whereas the areas of the two electrodes are fixed. The capacitance varies with time due to the oscillation of the sheath thickness $S(t)$. This oscillation produces a displacement current (displacement of electrons) which represents the reflected rf power P_r. The reflected power can overload

the power supply, and thus preventing effective delivery of the power to the discharge in the absence of an impedance matching network between the power source and the plasma. Figure 2-2 shows a schematic of the electrical power matching network used in the present sputtering system. A single power supply is used, and the rf power is split between the target and the substrate electrodes. Figure 2-3 shows the equivalent electrical circuit (Koening and Maissel, 1970).

Assuming that the ion density n_i is equal to the electron density n_e in the bulk of the plasma and that the electrons are in thermal equilibrium with the local plasma potential (Boltzmann-Maxwellian distribution), the ion current density j through the sheath can be expressed as (Smith, 1995)

$$j = 0.6 n_e e \sqrt{\frac{k_B T_e}{m_i}}, \tag{2-3}$$

where T_e is the electron temperature (degree in Kelvin) of a Boltzmann-Maxwellian distribution, k_B is the Boltzmann constant. The ion current densities in both sheaths are determined by the electron temperature and density in the plasma bulk. T_e is determined by particle conservation alone, and is independent of n_e and, therefore, input power. T_e is weakly dependent on the working pressure. n_e is determined by the total power balance in the discharge and is a function of pressure. It can be expressed as (Lieberman and Lichtenberg, 1994)

$$n_e = \frac{P_a}{e u_B A_{eff} \varepsilon_T}, \tag{2-4}$$

where P_a and $u_B = \sqrt{\frac{eT_e}{m_i}}$ are the absorbed rf power and Bohm velocity, respectively, ε_T is the total energy lost per ion lost from the system, and A_{eff} is the effective area given by (Lieberman and Lichtenberg, 1994)

$$A_{eff} = A(h_l + \frac{l}{R} h_{R)}, \tag{2-5}$$

where $l \approx 7$ cm and $R = 100$ mm are the discharge length and electrode radius, respectively, and $h_l \approx 0.86(3 + \frac{l}{2\lambda_i})^{-1/2}$ and $h_R \approx 0.80(4 + \frac{R}{\lambda_i})^{-1/2}$ represent the effects of working pressures on the ion distributions at the axial and radial sheath edges, where λ_i is the mean free path of ions. The total energy lost per ion lost from the system ε_T is given by (Lieberman and Lichtenberg, 1994)

$$\varepsilon_T = \varepsilon_C + 2T_e + \varepsilon_i, \tag{2-6}$$

where ε_C, $2T_e$, and ε_i represent the energy loss per electron-ion pair created, the mean kinetic energy lost per electron lost from the system, and the mean kinetic energy lost per ion across the sheath.

Hence, the ion current density j through the sheath is determined by the absorbed power P_a and electron temperature T_e, and can be expressed as

$$j = j_T = j_S = \frac{P_a}{\varepsilon_T} f(T_e), \tag{2-7}$$

where j_T and j_S are ion current densities into the target and substrate sheaths, respectively. The ion current density j is linearly dependent on absorbed power $\frac{P_a}{\varepsilon_T}$ for $T_e \approx$ constant.

For monatomic gas (e.g., Ar) discharge at low pressure and high power, all the absorbed power P_a is responsible for ion acceleration across the sheaths (Godyak, Piejak and Alexandrovich, 1991). For a symmetric rf discharge geometry, the absorbed power P_a is given by

$$P_a = j(\Delta V_T + \Delta V_S)A, \tag{2-8}$$

where $\Delta V_T = V_p - V_T$ and $\Delta V_S = V_p - V_S$ are voltage differences across the target and substrate sheaths, respectively, where V_p is the time-average plasma bulk voltage (≈ 10 V), and V_T and V_S are the time-average voltages at the target and substrate surfaces, respectively. From Eq. (2-8), the ion current density j can be obtained from the measured P_a, V_T, V_S, i.e.,

$$j = \frac{P_a}{A(2V_P - V_T - V_S)}, \tag{2-9}$$

where electrode area A (= 324 cm^2) is given for present sputtering system. Figure 2-4 shows the variation of the ion current density j with the absorbed rf power P_a for low-pressure Ar rf discharge under conditions of substrate bias voltage of –200 V, working pressure of 3 mTorr, and Ar gas flow rate of 20 sccm. The ion current density increases with absorbed rf power, agreeing well with the prediction of Eq. (2-7).

The time-average voltage across the sheath is given by (Lieberman and Lichtenberg, 1994)

$$\overline{V} \propto \frac{j^2}{e\varepsilon_o n_e \omega}. \tag{2-10}$$

Therefore, the time-average voltages across the target sheath can be expressed as

$$V_T = -\frac{P_a}{Aj} + 2V_P - V_S \propto \frac{u_B A_{eff}}{\varepsilon_o \omega} f^2(T_e)\frac{P_a}{\varepsilon_T}. \qquad (2\text{-}11)$$

From Eq. (2-11), it is obvious that the target is negatively self-biased because $\frac{P_a}{Aj} >> 2V_P - V_S$. For high sheath potential, $\varepsilon_T \approx \varepsilon_i$ because $\varepsilon_i >> \varepsilon_C$ and $\varepsilon_i >> T_e$. Roughly, $\varepsilon_i \approx e|V_T|$. Therefore,

$$V_T \propto \left(\frac{u_B A_{eff}}{\varepsilon_o \omega e}\right)^{1/2} f(T_e) P_a^{1/2}. \qquad (2\text{-}12)$$

The absolute value of the target self-bias voltage V_T increases with the square root of the absorbed rf power P_a for fixed substrate bias voltage V_S. Figure 2-4 also shows the variation of target self-bias voltage V_T with absorbed rf power P_a. The experimental results agree well with the prediction of Eq. (2-12).

Eq. (2-11) shows that $V_T + V_S$ is constant when the absorbed rf power P_a is fixed. Hence, the absolute value of V_T will decrease with increasing absolute value of negative V_S. Figure 2-5 shows the variation of V_T and $V_T + V_S$ with V_S for low-pressure Ar rf discharges under conditions of forward rf power P_f of 750 W, working pressure of 3 mTorr, and gas flow rate of 20 sccm. The results show that the experimental trends are in good agreement with the above interpretations for substrate bias voltages between 0 and –300 V. As shown in Figure 2-5, $V_T + V_S$ decreases with the decrease of V_S below –300 V. This is because the absorbed rf power P_a decreases when the negative substrate bias voltage is less than -300 V, as shown in Figure 2-6. The substrate is not self-biased. The negative substrate bias voltage V_S is applied independently through the substrate bias

adjuster (Figure 2-2). The change in V_S affects the impedance Z_S between the substrate and the bulk of plasma and the impedance Z_{SG} between the substrate and the ground (Figure 2-3), resulting in the change of the total impedance of the plasma, which produces a mismatch between the impedances of the rf source and the plasma. The mismatch impedances prevent the rf source from delivering efficiently power to the plasma, resulting in the decrease of the absorbed rf power P_a even though the forward rf power P_f is fixed at 750 W. Therefore, the system must be tuned to match the impedances of the rf source and the plasma. The present system is tuned to work well for substrate bias voltage in the range of 0 to -300 V. In this range, the reflected rf power P_r is less than 3% of the forward rf power P_f.

The variation of the forward rf power P_f may cause changes in the rf source impendence, which can also lead to a mismatch between the impedances of the rf source and the plasma and prevent the rf source from efficiently delivering power to the plasma. Figure 2-7 shows the effect of the forward rf power P_f on the absorbed rf power P_a for Ar rf discharges under conditions of substrate bias voltage V_S of -200 V, working pressure of 3 mTorr, and gas flow rate of 20 sccm. The ratio of P_a / P_b increases with the forward rf power P_f. For forward rf power P_f between 400 to 750 W, the absorbed rf power P_a is larger than 95% forward rf power P_f. However, when the forward rf power P_f is less than 400 W, the ratio of P_a / P_b decreases dramatically with the decrease of the forward rf power P_f.

2.4 Effects of Working Pressure and Gas Flow Rate on Low-Pressure rf Discharge

The significance of working pressure and gas flow rate on low-pressure Ar rf discharge is investigated experimentally under conditions of forward rf power P_f of 750 W and substrate bias voltage V_S of -200 V. The working pressure can be adjusted by controlling the throat valve opening (Figure 2-1). However, the adjustable range of the working pressure is limited by the Ar gas flow rate. Figure 2-8 shows the Ar gas flow rate dependence of the adjustable range of the working pressure. The adjustable range of working pressure increases with the Ar gas flow rate. Figures 2-9 - 2-11 show the variations of absorbed rf power P_a, ion current density j, and target self-bias voltage V_T, respectively, with the working pressure and Ar gas flow rate. The results show that the gas flow rate has a secondary effect on the low-pressure Ar rf discharge. However, the working pressure has a significant effect on this discharge. The absorbed rf power P_a increases with increasing working pressure continuously, reaching a maximum at ~2.5 mTorr, and then decreases above ~2.5 mTorr working pressure (Figure 2-9). Alternatively, the ion current density j increases and the target self-bias voltage V_T decreases with increasing working pressure, both reaching steady-state values for the working pressure greater than 2.5 mTorr (Figures 2-10 and 2-11).

At low pressures (<10 mTorr), the pressure effect on the sheath thickness is marginal (Pennebake, 1979). As mentioned previously, the electron temperature T_e is weakly dependent on the working pressure. However, increasing the pressure enhances both the discharge rate of Ar atoms and the recombination rate between electrons and ions due to the increase of particle collisions in the bulk plasma space. The mean free path of particles in the bulk plasma space is given by

$$\lambda = \frac{k_B T}{\sqrt{2}\pi d^2 p}, \tag{2-13}$$

where T , d , and p are the temperature of the bulk plasma, particle diameter and working pressure, respectively. Eq. (2-13) shows that the electron mean free path is significantly longer than that of the Ar ions due to the smaller size of the electrons. Hence, the increase of the recombination rate between electrons and Ar ions is less than the discharge rate of Ar atoms. This leads to an increase in the Ar ion density n_i in the bulk plasma with an increase in the working pressure, which equals the electron density n_e. In view of Eq. (2-3), the ion current density j increases with n_e. The experimental trend shown in Figure 2-10 is in good agreement with the former interpretation. The increase of the Ar ion density in the bulk plasma changes the plasma impedance, thus, producing a mismatch between the rf source and plasma impedances, which leads to the decrease of the absorbed rf power P_a. This is the reason why the absorbed rf power P_a decreases for the working pressure above 2.5 mTorr (Figure 2-9). The decrease of the absorbed rf power P_a leads to a decrease in the target self-bias voltage V_T , as indicated by Eq. (2-12).

2.5 Summary

Relationships including the forward rf power, substrate bias voltage, and target self-bias voltage are observed in experiments at different conditions of low-pressure Ar rf discharge performed in a Perkin-Elmer sputtering system without magnetron. The effects of the forward rf power, substrate bias voltage, working pressure, and Ar gas flow rate on the target self-bias voltage and ion current density are interpreted in the context of both energy balance and sheath capacitance considerations. It is found that the Ar gas flow

rate only determines the adjustable range of the working pressure, while its effect on the discharge is secondary. However, the forward rf power, substrate bias voltage, and working pressure exhibit strong effects on the plasma discharge, and the energy delivery from the rf source to the discharge is most efficient when the former parameters are in their optimized ranges. Therefore, tuning of the rf sputtering system is essential for efficient energy delivery and better control of the discharge process.

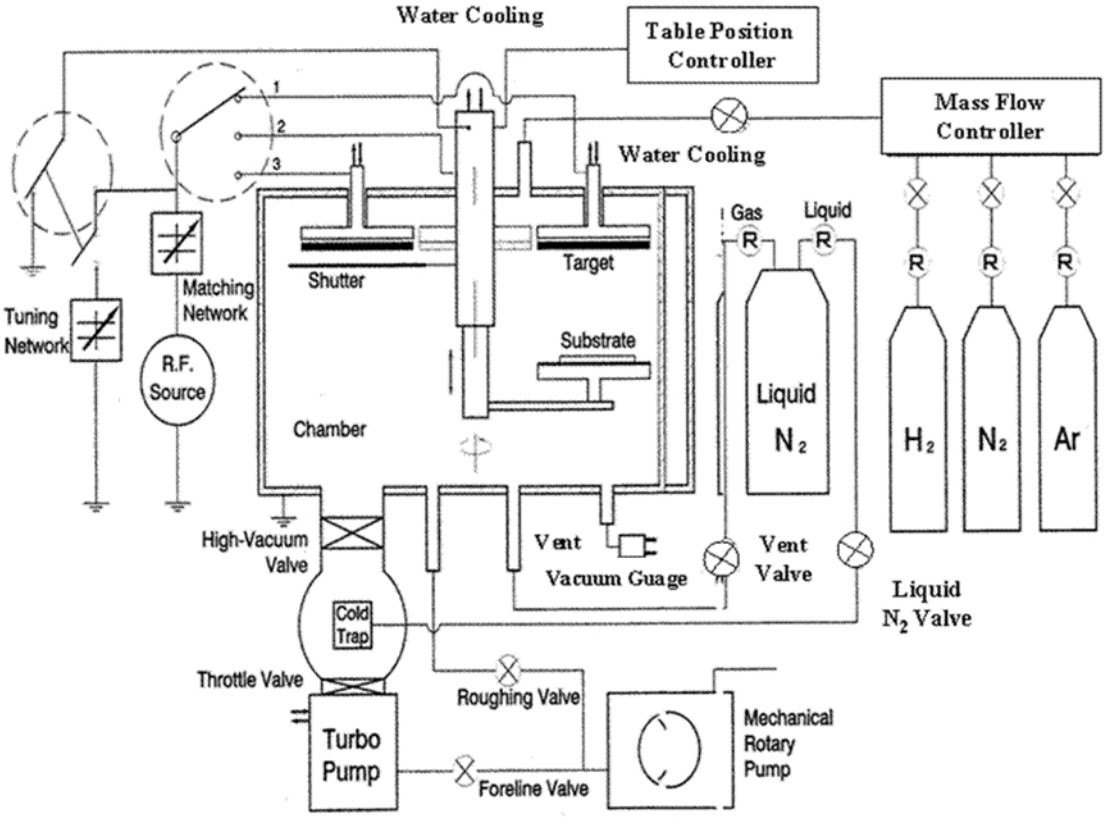

Figure 2-1 Schematic of rf sputtering system.

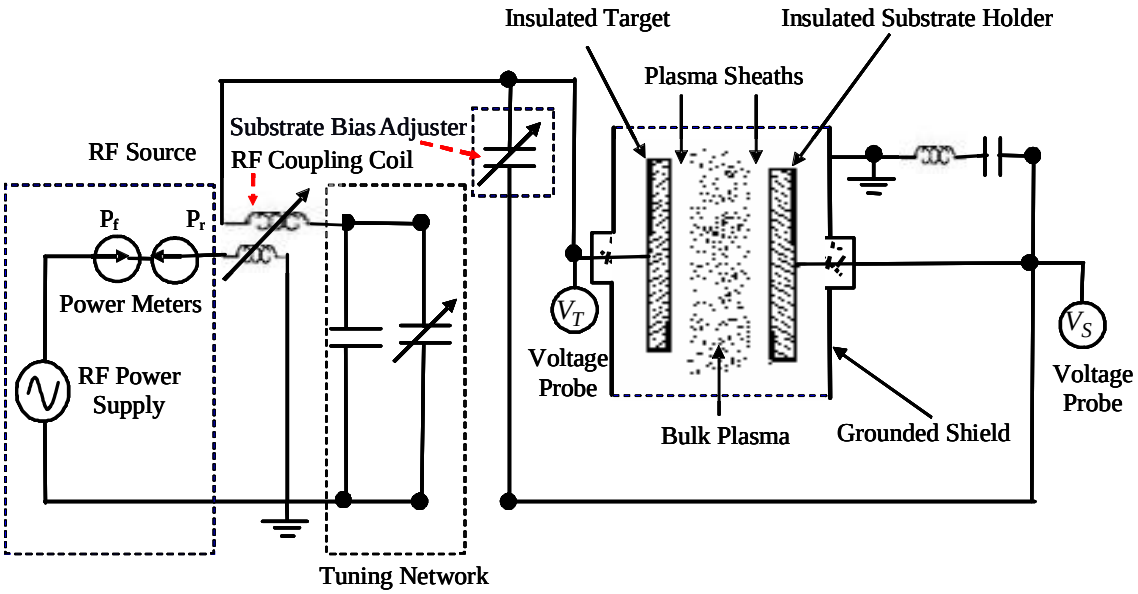

Figure 2-2 Schematic of electrical power matching network.

P_f : Forward rf power; P_r : Reflected rf power;

V_T : Target self-bias voltage; V_S : Substrate bias voltage.

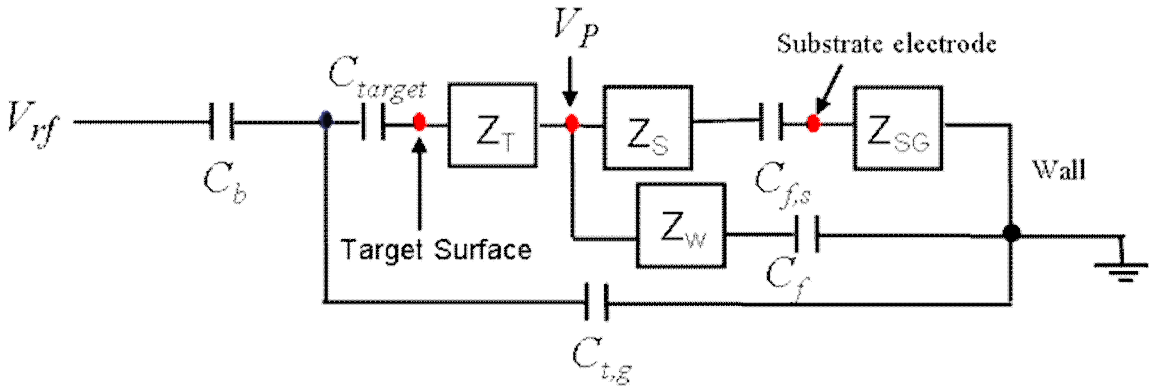

Figure 2-3 Equivalent electrical circuit of single rf power sputtering system.

Z_T : Impedance between target and plasma;

Z_S : Impedance between substrate and plasma;

Z_{SG} : Impedance between substrate and ground;

Z_W : Wall impedance

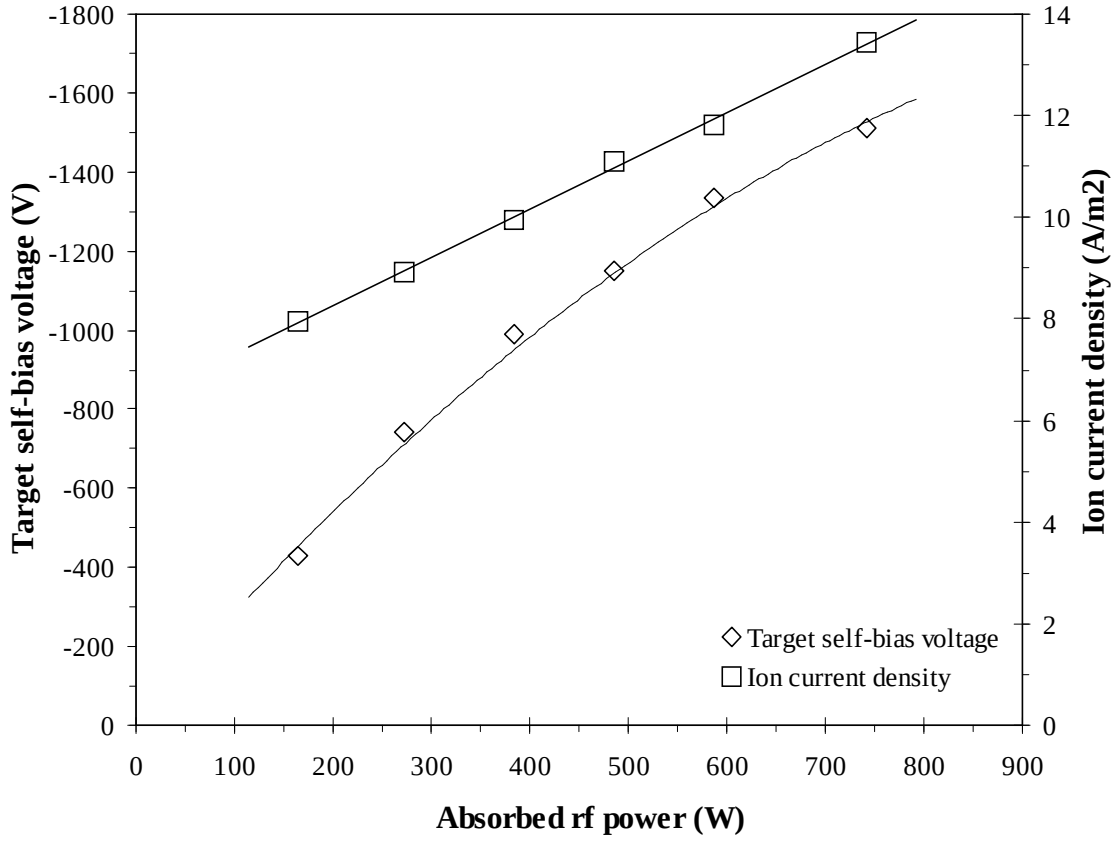

Figure 2-4 Target self-bias voltage V_T and ion current density j versus absorbed rf power P_a for low-pressure Ar rf discharge under conditions of substrate bias voltage of –200 V, working pressure of 3 mTorr, and gas flow rate of 20 sccm.

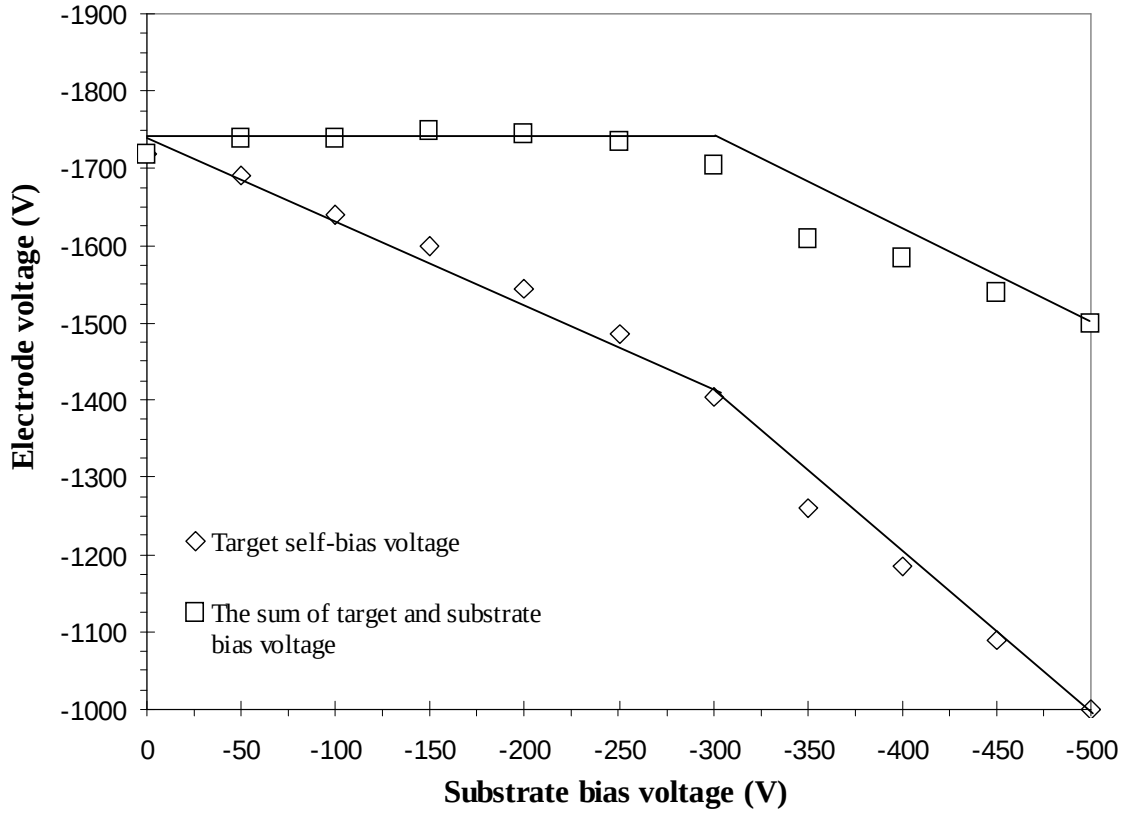

Figure 2-5 Target self-bias voltage V_T and ion current density j versus absorbed rf power P_a for low-pressure Ar rf discharge under conditions of substrate bias voltage of –200 V, working pressure of 3 mTorr, and gas flow rate of 20 sccm.

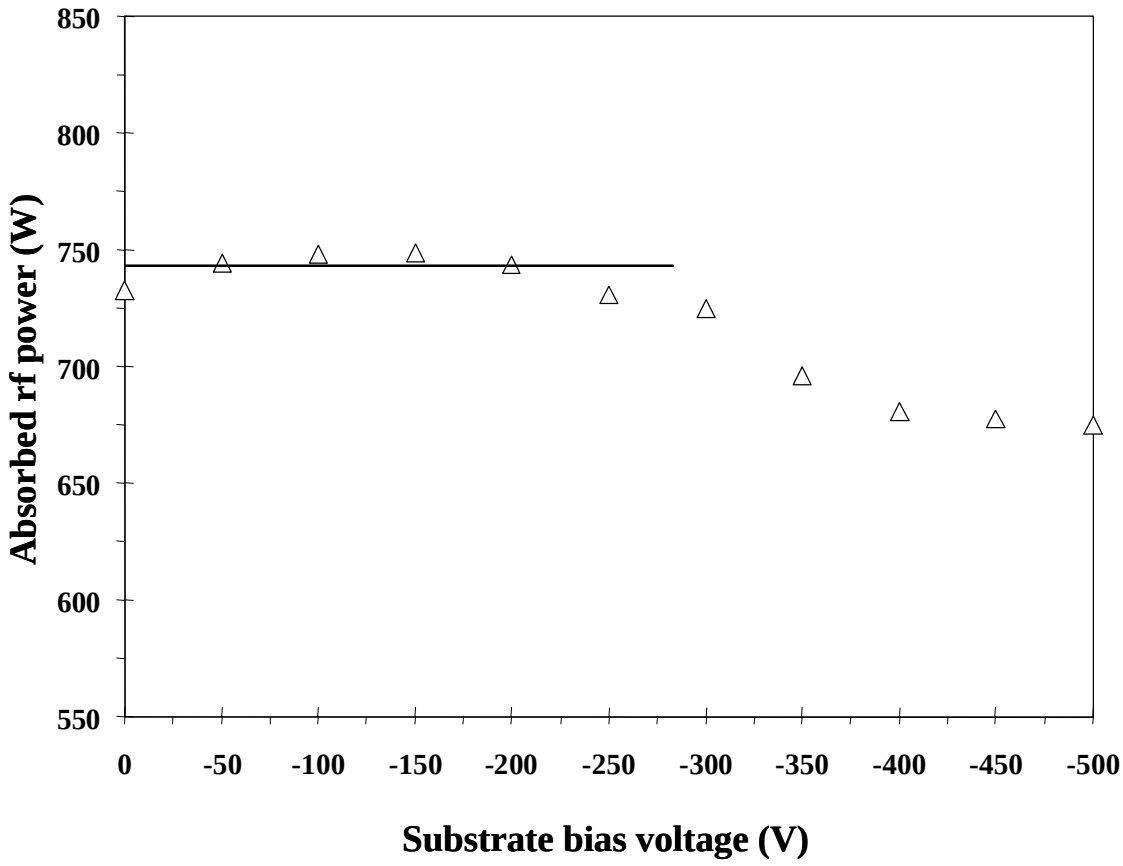

Figure 2-6 Absorbed rf power P_a versus substrate bias voltage V_S for low-pressure Ar rf discharge under conditions of forward rf power P_f of 750 W, working pressure of 3 mTorr and gas flow rate of 20 sccm. The solid line shows the well tuned range of substrate bias voltage.

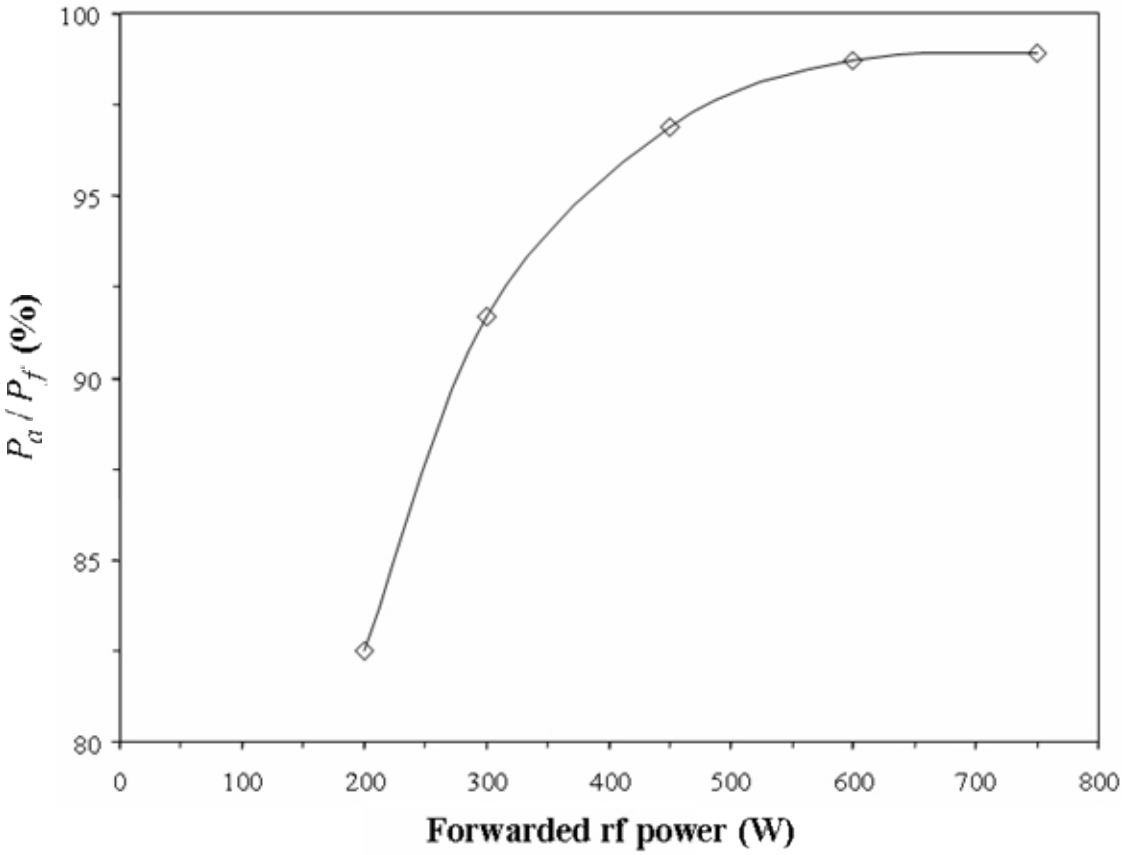

Figure 2-7 The effect of forward rf power P_f on the level of absorbed rf power P_a for low-pressure Ar rf discharge under conditions of substrate bias voltage V_S of -200 V, working pressure of 3 mTorr and gas flow rate of 20 sccm.

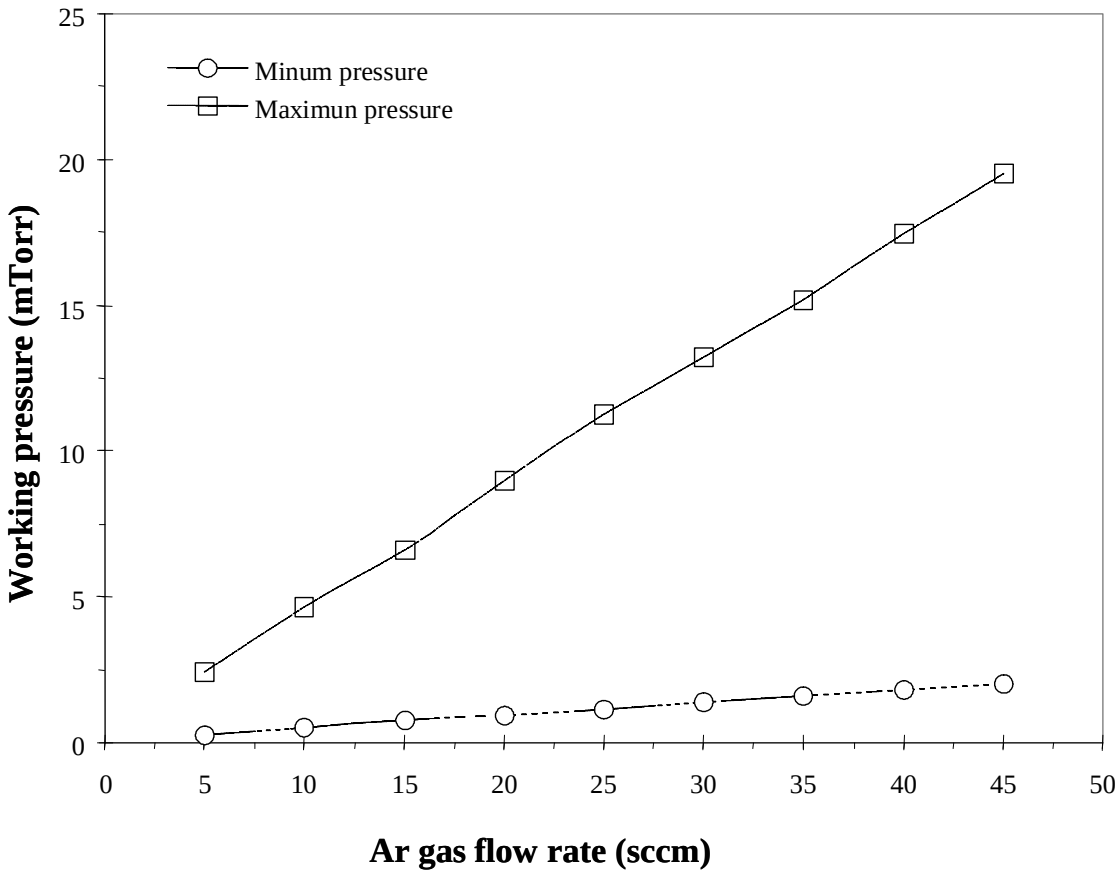

Figure 2-8 Ar gas flow rate dependence of working pressure adjustable range.

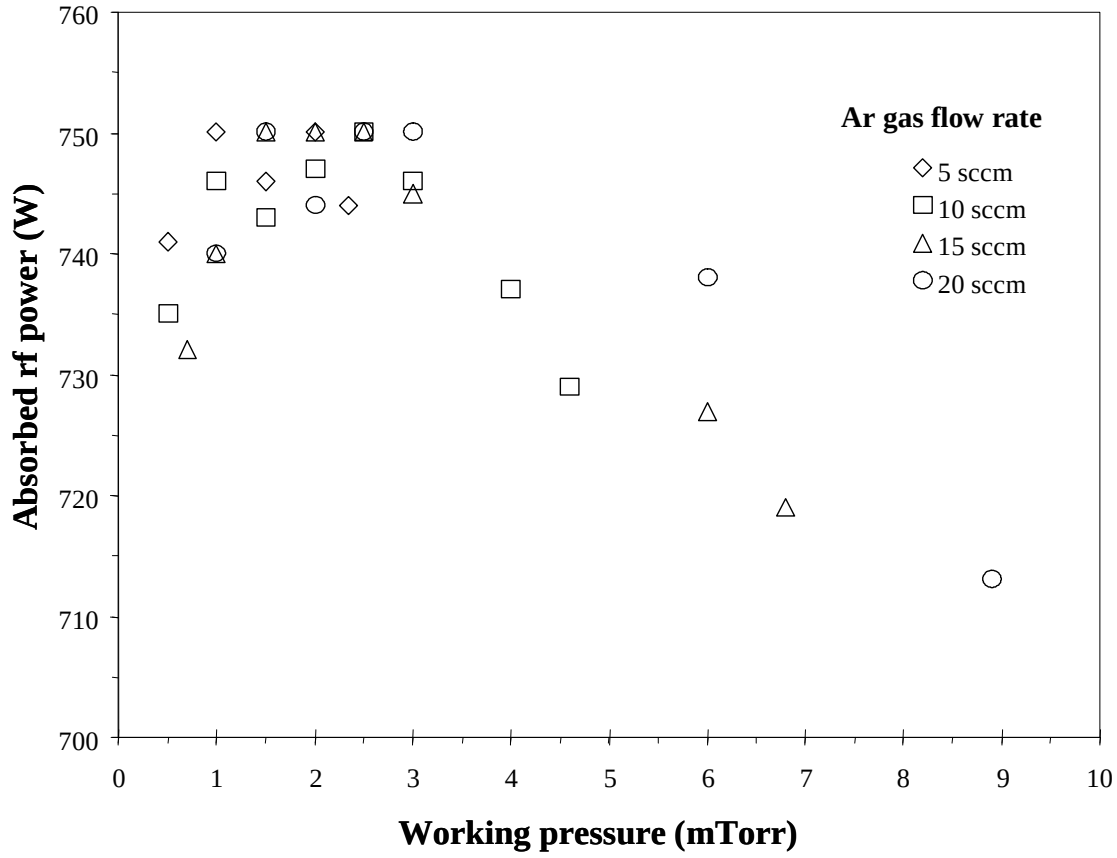

Figure 2-9 Effects of working pressure and gas flow rate on the absorbed rf power P_a for low-pressure Ar rf discharge under conditions of forward rf power P_f of 750 W, and substrate bias voltage V_S of –200 V.

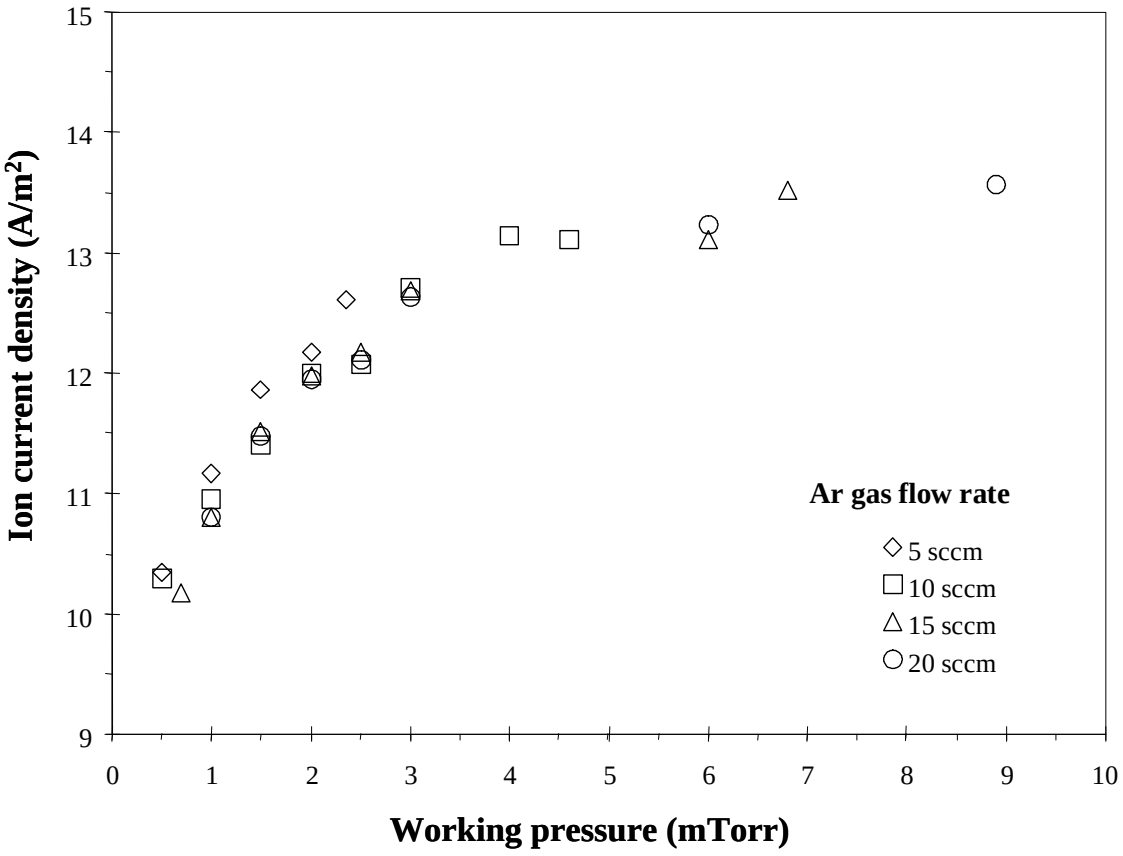

Figure 2-10 Effects of working pressure and gas flow rate on ion current density j for low-pressure Ar rf discharge under conditions of forward rf power P_f of 750 W, and substrate bias voltage V_S of –200 V.

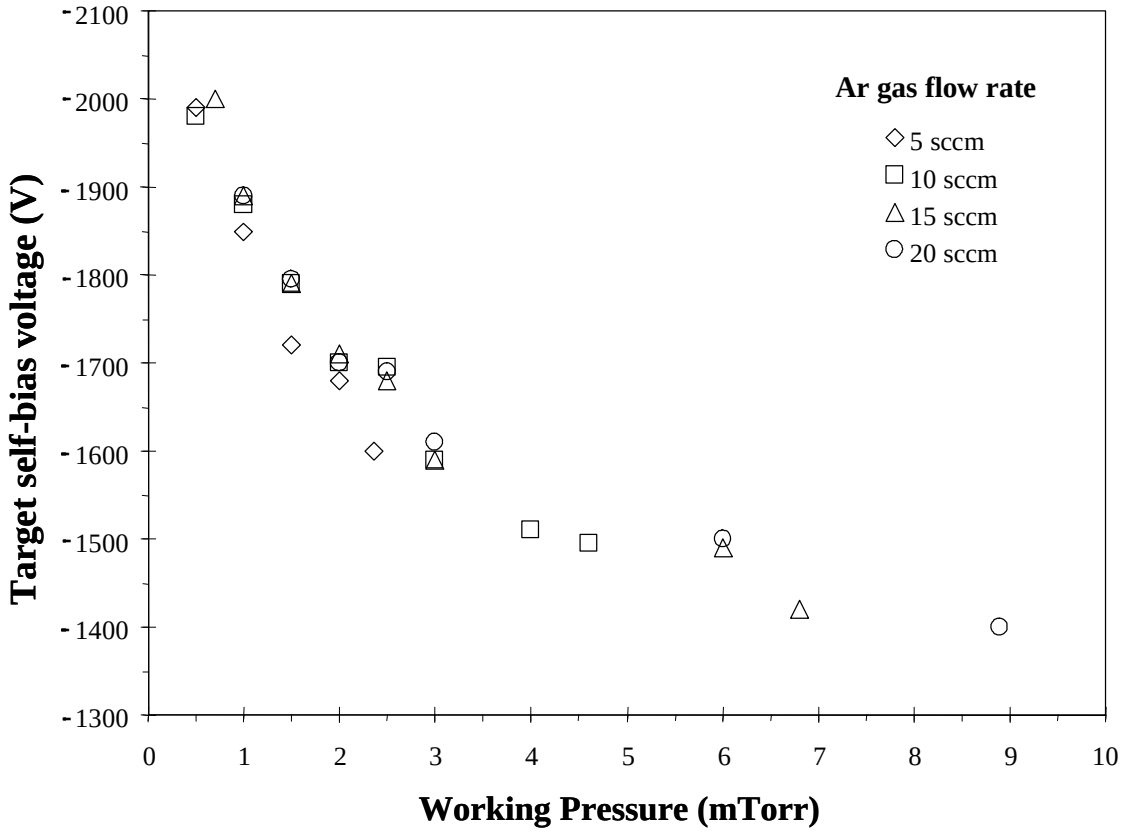

Figure 2-11 Effects of working pressure and gas flow rate on target self-bias voltage V_T for low-pressure Ar rf discharge under conditions of forward rf power P_f of 750 W, and substrate bias voltage V_S of –200 V.

CHAPTER 3

Effect of Low-Pressure RF Discharge on the Growth of Sputtered *a-C* Films

3.1 Introduction

Hydrogen-free amorphous carbon (*a-C*) films deposited by various methods exhibit excellent physical properties (Tsai and Bogy, 1987; Lifshitz, 1997; Robertson, 2002). Formation of ultrathin carbon films on a highly oriented pyrolytic graphite substrate has been accomplished by the deposition of low-energy carbon ions at temperatures from ambient to 300^{o}C (Durand, et al, 1998). Roughening due to the transition from lateral island growth to three-dimensional film growth was found to depend on the substrate temperature and ion-current density. The surface roughness, density, percentage of sp^3 tetrahedral carbon bonding, and internal compressive stresses of ultrathin *a*-C films deposited by sputtering under a positive substrate bias voltage decreased with the increase of the film thickness (Logothetidis and Stergioudis, 1997). Applying a negative bias voltage to the substrate during sputter deposition in a pure Ar atmosphere was reported to significantly increase the density as a result of the transition from trigonal (sp^2) to tetragonal (sp^3) carbon hybridizations under high compressive stress (Schwan, et al, 1997). Intense energetic particle bombardment on a growing *a*-C film surface strongly affects the compressive stress level; however, the relationship between the intense bombardment and the produced compressive stress level appears to be complex (Windischmann, 1992; Davis, 1993).

During rf sputter deposition under low working pressure (~3 mTorr), collisionless plasma sheaths are produced which increase the ion impinging fluxes on both target and

substrate surfaces. The absorbed rf power directly influences the ion density in the plasma bulk and the ion fluxes at the plasma sheath edges. The kinetic energy of the ions bombarding the growing film surface depends on the substrate bias voltage and influences the ion bombardment effect. In this chapter, the effect of low-pressure Ar rf discharge on the growth of ultrathin *a-C* films synthesized by rf sputter deposition is investigated experimentally, and the roles of the above factors are analyzed in light of experimental results obtained from sputtered *a*-C films.

3.2 Experimental Procedures

Ultrathin *a-C* films are deposited on Si(100) substrates by Ar^+ sputtering of a pure graphite target using a Perkin-Elmer Randex-2400 model sputtering system without magnetron (Figure 2-1). The vacuum chamber is first pumped down to a low base pressure ($< 2\times10^{-6}$ Torr) to reduce the effect of residual gases before introducing the Ar gas into the process chamber. Before film deposition, the graphite target is sputter cleaned for 3-20 minutes, depending on the previous time of exposure of the chamber to the atmosphere, and the Si(100) substrate is sputter etched for 3 minutes to remove a surface layer of thickness ~40 nm. The precleaning process is carried out at 250 W forward rf power, 3 mTorr working pressure, and 20 sccm argon gas flow rate.

Ultrathin *a-C* films are synthesized under conditions of forward rf power in the range of 200-750 W, substrate bias voltage between 0 and -500 V, working pressure of 3 mTorr, gas flow rate of 20 sccm, and deposition time in the range of 3-11 minutes. Film surface roughness measurements are obtained from 1 μm^2 surface area images obtained with an atomic force microscope (Digital Instruments, NanoScope II), and the root-mean-

square (rms) surface roughness is calculated as the average of five rms values obtained from different surface area images of the same film sample. The film thickness is measured directly from cross-sectional images taken at different positions of the same sample using a high-resolution transmission electron microscope (Philip CM300FEG/UT).

3.3 Ar Ion Impinging Flux and Ar-Ion-Induced Sputtering Yield of Graphite

Figure 3-1 shows schematically the processes of *a*-C film deposition by Ar^+ sputtering involving three sequential processes: (i) sputtering of carbon atoms from graphite target by energetic Ar^+, (ii) carbon atom transport through the plasma space between the target and the substrate, and, (iii) surface diffusion of arriving carbon atoms on the substrate surface to form stable chemical bonds with other carbon atoms. The growth rate of the *a-C* film depends on the carbon atom flux at the substrate surface, carbon atom resputtering rate from the surface, and carbon atom redeposition from the residual carbon layer deposited on the substrate holder surface (Figure 3-1). However, the later effect can be neglected because the surface area of the Si(100) substrate is much smaller than that of the substrate holder and the moving directions of resputtered carbon atoms from the residual carbon layer are random. The flux of the carbon atoms at the substrate surface is directly related to the Ar^+ impinging flux J_{Ar^+} and sputtering yield of carbon γ, which is defined as the number of carbon atoms ejected from the bombarded target surface per incident energetic Ar^+.

Based on energy balance consideration and the ion current density j given by Eq. (2-9), the Ar^+ impinging flux J_{Ar^+} can be expressed as

$$J_{Ar^+} = \frac{P_a}{eA(2V_p - V_T - V_S)}, \tag{3-1}$$

where e is the electron charge. J_{Ar^+} increases with the absorbed rf power P_a when the working pressure is maintained constant (Eq. 2-7).

Sputtering of the target by energetic Ar^+ is essentially a process involving cascades of atomic collisions. Sigmund (1969) proposed a theory to calculate the sputtering yield of amorphous and polycrystalline materials based on the assumption of random slowing down of the ions in an infinite medium. The sputtering yield of a solid is a function of the energy of the incident ions. Matsunami et al. (1984) compiled the available experimental data graphically, and developed an empirical formula of the energy dependent ion-induced sputtering yields of monatomic solids for various ion-target combinations, given by:

$$\gamma = 0.42 \frac{\alpha^* Q K s_n(\varepsilon)}{U_s[1 + 0.35 U_s s_e(\varepsilon)]} [1 - (\frac{E_{th}}{E})^{1/2}]^{2.8}, \tag{3-2}$$

where α^*, Q, E_{th} are empirical parameters, U_s is the target sublimation energy (eV), E is the energy of incident ions, s_n and s_e are Lindhard's elastic and inelastic reduced stopping cross sections, respectively, and ε is the reduced energy. For graphite target, Q =3.1 ± 0.9 and U_s =7.37 eV. The express for the reduced energy is:

$$\varepsilon = \frac{0.03255}{Z_1 Z_2 (Z_1^{2/3} + Z_2^{2/3})^{1/2}} \frac{M_2}{M_1 + M_2} E \text{ (eV)}. \tag{3-3}$$

The elastic and inelastic reduced stopping cross sections are given by:

$$s_n = \frac{3.44\sqrt{\varepsilon} \ln(\varepsilon + 2.718)}{1 + 6.355\sqrt{\varepsilon} + \varepsilon(-1.708 + 6.882\sqrt{\varepsilon})}, \tag{3-4}$$

and

$$s_e = 0.079 \frac{(M_1 + M_2)^{3/2}}{M_1^{3/2} M_2^{1/2}} \frac{Z_1^{2/3} Z_2^{1/2}}{(Z_1^{2/3} + Z_2^{2/3})^{3/4}} \sqrt{\varepsilon} \,. \tag{3-5}$$

In Eqs. (3-3) - (3-5), Z_1 and Z_2 are the atomic numbers of the incident ions and target atoms, and M_1 and M_2 are their mass numbers, respectively. The empirical parameter α^* is expressed as:

$$\alpha^* = 0.08 + 0.164 (\frac{M_2}{M_1})^{0.4} + 0.0145 (\frac{M_2}{M_1})^{1.29} \,. \tag{3-6}$$

The empirical parameter E_{th} is given by:

$$\frac{E_{th}}{U_s} = 1.9 + 3.8 (\frac{M_2}{M_1})^{-1} + 0.134 (\frac{M_2}{M_1})^{1.24}, \tag{3-7}$$

under the condition of $K s_n(\varepsilon) > 2.5$ eV-cm^2/10^{15} atoms to avoid the influence of nonlinear effect on the empirical parameters, where K is the conversion factor in units of eV-cm^2/10^{15} atoms defined as:

$$K = \frac{S_n}{s_n} = 8.478 \frac{Z_1 Z_2}{(Z_1^{2/3} + Z_2^{2/3})^{1/2}} \frac{M_1}{M_1 + M_2} \,. \tag{3-8}$$

The sputtering yields of the graphite target are calculated using the above equations under different Ar^+ bombarding conditions. Figure 3-2 shows that the sputtering yield γ and Ar^+ impinging flux J_{Ar^+} increase with the forward rf power for substrate bias voltage V_S and working pressure fixed at –200 V and 3 mTorr, respectively. Figure 3-3 shows that the sputtering yield γ decreases with the increase of the negative substrate bias voltage for forward rf power and working pressure maintained at 750 W and 3

mTorr, respectively. However, the impinging flux J_{Ar^+} is nearly independent of the substrate bias voltage, which is in agreement with previous interpretations (Eq. 2-7).

3.4 Effect of Process Conditions on the Growth of *a*-C Films

The effect of process conditions in low-pressure Ar rf discharge on the growth of *a*-C films is investigated experimentally at working pressure of 3 mTorr and gas flow rate of 20 sccm. All the results are given in Tables 3-1 through 3-3. Table 3-1 shows the effect of absorbed rf power P_a on the *a*-C film thickness and roughness for substrate bias voltage of -200 V and 0 V and deposition time of 3minutes. The absorbed rf power P_a varies in the range of 170-742 W. Table 3-2 shows the effect of substrate bias voltage V_S varied between 0 and -500 V on the *a*-C film thickness and roughness for forward rf power equal to 750 W and deposition time equal to 3 minutes. Table 3-3 shows the effect of deposition time varied from 3 to 11 minutes on the *a*-C film thickness for forward rf power of 750 W and substrate bias voltage of -200 V. All of the film thickness data listed in the above tables are obtained directly from high-resolution cross-sectional transmission electron microscope images. Figure 3-4 shows a transmission electron microscope image of an *a*-C film deposited under forward rf power of 750 W, substrate bias voltage of –200 V, working pressure of 3 mTorr, gas flow rate 0f 20 sccm and deposition time of 3 minutes.

As discussed previously, the *a*-C film thickness depends on the number of carbon atoms arriving at the substrate surface and the number of resputtered carbon atoms removed from the surface. There are two competing factors that determine the number of carbon atoms arriving at the substrate surface: the sputtering rate β, defined as the

number of atoms sputtered off from a unit area of the target surface per unit time, and the scattering effect of carbon atoms during transport through the target-substrate plasma space. The sputtering rate β is proportional to the sputtering yield γ and Ar^+ impinging flux J_{Ar^+},

$$\beta = \gamma J_{Ar^+}. \tag{3-9}$$

The scattering effect is inversely proportional to λ / L, where L is the distance between the target and the substrate, and λ is the mean free path of the particles given by

$$\lambda = \frac{k_B T}{\sqrt{2}\pi d^2 p}, \tag{3-10}$$

where T is the bulk plasma temperature, which is significantly higher than the room temperature (300 K) (Lieberman and Lichtenberg, 1994), d is the particle diameter (< 3 Å), and p is the working pressure. The target-substrate distance L in the present sputtering system is fixed at 7 cm. For p=3 mTorr (0.4 Pa), the mean free path λ of the particles is larger than 10 cm. Therefore, $\lambda / L > 1$ and the scattering effect on the film growth is marginal in the present experiments.

The number of resputtered carbon atoms from the growing film surface depends on the intensity of the Ar^+ bombardment. Assuming that the Ar^+ induced sputtering yield of the *a*-C film surface is equal to the Ar^+ induced sputtering yield of the graphite, the sputtering yield γ_S of the *a*-C film due to Ar^+ bombardment can be determined from Eq. (3-2). The relationship between ratio $\frac{\gamma_S}{\gamma}$ and absorbed rf power P_a for the substrate bias voltage equal to -200 V is shown in Figure 3-5. The ratio $\frac{\gamma_S}{\gamma}$ is less than 10% for the

absorbed rf power P_a larger than 200 W. Hence, the resputtering effect due to Ar^+ bombardment on the growing *a*-C film surface is secondary in film growth.

In view of the aforementioned, it may be concluded that the *a*-C film thickness t_f depends mainly on the sputtering rate β and deposition time t for fixed room temperature deposition, i.e.,

$$t_f \propto t\beta . \tag{3-11}$$

Figure 3-6 shows the relationship between the measured film thickness data and the product of the sputtering rate β and deposition time t. This linear relationship result is excellent agreement with the above interpretation (Eq. (3-11).

3.5 Effect of Process Conditions on *a*-C Film Surface Roughness

Ar^+ bombardment exhibits a significant effect on the *a*-C film surface roughness. Figure 3-7 shows the effect of the substrate bias voltage on the *a*-C film surface roughness. The films are deposited at room temperature in a pure Ar plasma atmosphere under conditions of forward rf power of 750 W, working pressure of 3 mTorr, gas flow rate of 20 sccm, and deposition time of 3 minutes. In the absence of substrate bias voltage, film growth is mainly controlled by the flux of impinging carbon atoms, surface temperature, and surface diffusion. At room temperature deposition, the previous deposition conditions lead to a relatively high content of trigonal carbon bonding (sp^2) and rough surface topography (typical rms surface roughness is ~1.13 nm). Applying a negative bias voltage to the substrate promotes Ar^+ bombardment on the growing film surface, which promotes random surface motion of the carbon atoms. This effect enhances more carbon atoms to form strong tetrahedral bonds (sp^3) and produces a

smooth surface. The smoothest *a*-C films are deposited under substrate bias voltage of –200 V. These film exhibit an rms roughness of only ~0.12 nm. At relatively high bias voltages (i.e., intensive Ar^+ bombardment), irradiation damage and roughening of the film surface occur due to intensification of the resputtering and Ar^+ implantation effects.

The effect of the forward rf power on the film surface roughness is also investigated by depositing *a*-C films under conditions of working pressure of 3 mTorr, gas flow rate of 20 sccm, deposition time of 3 minutes, and varied forward rf power. In the presence of Ar^+ bombardment during film deposition due to substrate bias voltage of -200 V, the surface rms roughness varies in a narrow range for forward rf power between 250 and 750 W (Figure 3-8). Hence, the effect of the forward rf power on the film surface roughness is secondary because the random motions of the carbon atoms at the growing film surface are controlled by the Ar^+ bombardment. However, the film surface roughness is strongly affected by the forward rf power in the absence of Ar^+ bombardment during film deposition (zero substrate bias) (Figure 3-8). The rms roughness increases from 0.32 nm to 1.13 nm as the forward rf power increases from 300 to 750 W. The increase of the forward rf power in this range results in the increase of both the Ar^+ impinging flux and film growth rate from 5.16×10^{15} to 8.08×10^{15} ions/s·cm^2 (Table 3-1) and 0.81 to 1.89 Å/s, respectively. The increase of the density of carbon atoms arriving at the film surface prevents the surface diffusion of carbon atoms, producing a thick and rough *a*-C film. Therefore, in the absence of Ar^+ bombardment, the film growth rate exhibits significant correlation with the *a*-C film surface roughness.

The effect of the Ar gas flow rate is investigated for conditions of forward rf power of 750 W, substrate bias voltage of –200 V, working pressure of 3 mTorr, and

deposition time of 3 minutes. Figure 3-9 shows that the rms roughness varies in the narrow range of 0.1-0.2 nm with the Ar gas flow rate. This shows a marginal effect of the Ar gas flow rate on the *a*-C film surface roughness.

3.6 Summary

The effect of low-pressure Ar rf discharge on the growth of rf sputtered *a*-C films is investigated experimentally. It is found that the film thickness is a linear function of the product of the sputtering rate and deposition time. The effects of resputtering of carbon materials from the growing film surface by impinging Ar^+ and scattering during carbon atom transport through the plasma space between the target and the substrate on the film thickness are shown to be secondary. The principal factors affecting the film surface roughness are the film growth rate and the intensity of the Ar^+ bombardment. In the absence of energetic ion bombardment, the faster film growth the rougher the film surface. However, in the presence of energetic ion bombardment on the growing film surface, the *a*-C film surface roughness is controlled by the intensity of ion bombardment. Energetic particle bombardment on the growing film surface at ~210 eV enhances carbon atom random motion at the surface, and promotes the growth of the smoothest *a*-C film. However, for ion bombardment energy above ~210 eV, the surface roughness increases due to the combined effects of increases resputtering and, especially, high irradiation damage.

Table 3-1 Effect of absorbed rf power on *a*-C film thickness and surface roughness*

Absorbed rf power (W)	Impinging flux ($\times 10^{15}$ ions/s·cm^2)	Ar^+ kinetic energy on target (eV)	Ar^+ kinetic energy on substrate (eV)	Thickness (nm)	Surface rms roughness (nm)
172	4.61	509	210	5.6	___
285	5.43	800	210	10.9	0.09 ± 0.01
388	6.12	1010	210	15.6	___
500	6.78	1210	210	18.9	0.09 ± 0.01
600	7.04	1350	210	23.1	0.15 ± 0.01
739	7.99	1570	210	28.7	0.12 ± 0.01
298.5	5.16	1005	10	14.6	0.32 ± 0.07
401	5.89	1300	10	19.1	0.46 ± 0.04
496.5	6.73	1410	10	23.2	0.74 ± 0.06
595	7.30	1560	10	27.1	0.97 ± 0.11
741.5	8.08	1755	10	34.1	1.13 ± 0.14

* Deposition time = 3 minutes; Working pressure = 3 mTorr; Ar gas flow rate = 20 sccm.

Table 3-2 Effect of substrate bias on *a*-C film thickness and surface roughness*

Substrate bias voltage (V)	Absorbed rf power (W)	Impinging flux ($\times 10^{15}$ ions/s·cm^2)	Ar^+ kinetic energy on target (eV)	Thickness (nm)	Surface rms roughness (nm)
0	741.5	8.08	1755	34.1	1.13 ± 0.14
-50	746.5	8.22	1695	32.2	0.60 ± 0.04
-100	747.5	8.10	1640	30.8	___
-150	744.5	8.13	1610	29.6	0.21 ± 0.02
-200	739	7.99	1570	28.7	0.12 ± 0.01
-300	715	8.26	1355	25.4	0.36 ± 0.07
-400	675	8.44	1130	___	0.35 ± 0.07
-500	672	8.56	1000	___	0.21 ± 0.02

*Deposition time = 3 minutes; Working pressure = 3 mTorr; Ar gas flow rate = 20 sccm.

Table 3-3 Effect of deposition time on *a*-C film thickness*

Deposition Time (min)	Absorbed rf Power (W)	Impinging flux ($\times 10^{15}$ ions/s·cm^2)	Ar^+ kinetic energy on target (eV)	Thickness (nm)	Surface rms roughness (nm)
3	739	7.99	1570	28.7	0.12
5	749	8.21	1545	46	___
7	746	8.19	1543	67	___
9	746	8.11	1560	85	___
11	747	8.12	1560	100	___

* Substrate bias voltage = -200 V; Working pressure = 3 mTorr;

Ar gas flow rate = 20 sccm.

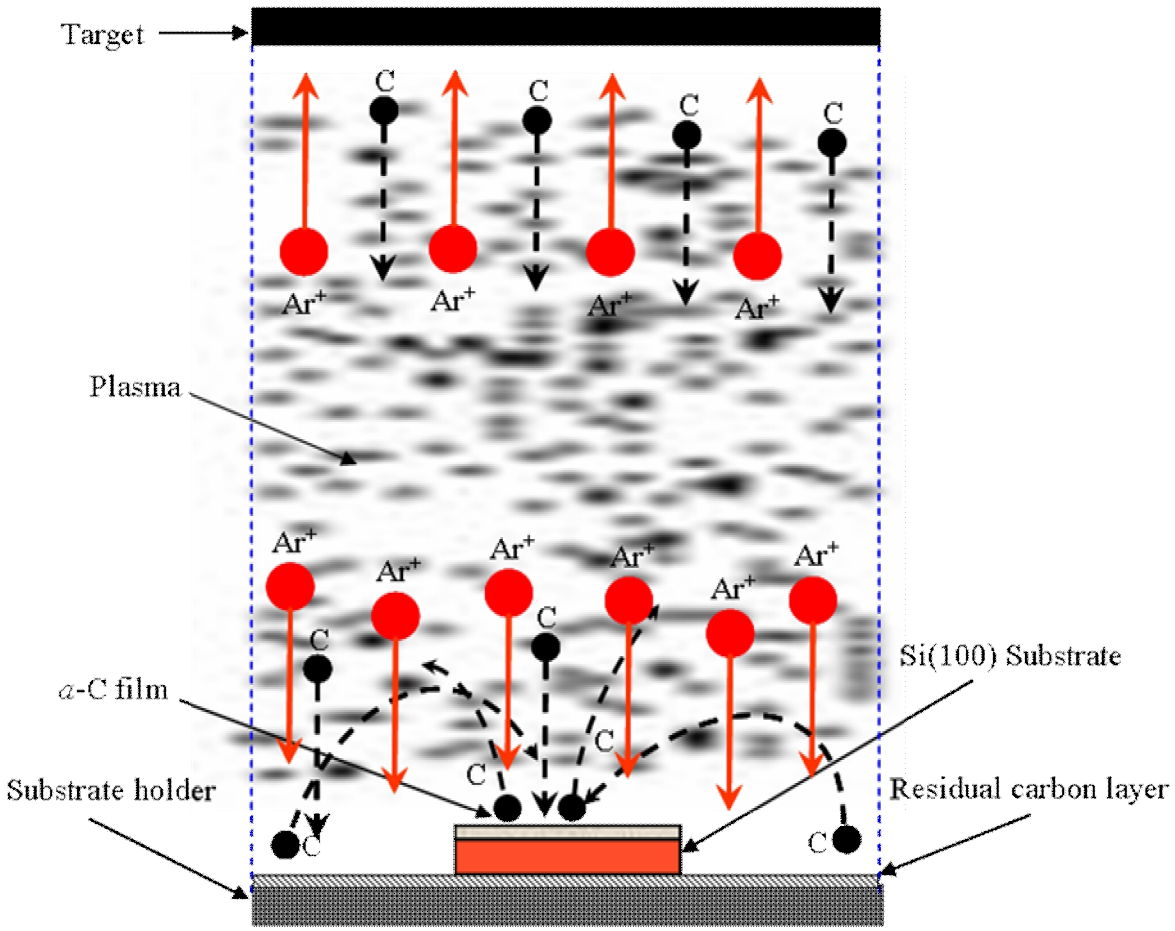

Figure 3-1 Schematic of *a*-C film deposition by Ar^+ sputtering showing carbon atom sputtering from the graphite target, carbon atom arrival to the substrate surface after transport through the plasma space between the target and the substrate, and carbon atom surface diffusion on the substrate surface leading to the formation of stable chemical bonds with other carbon atoms.

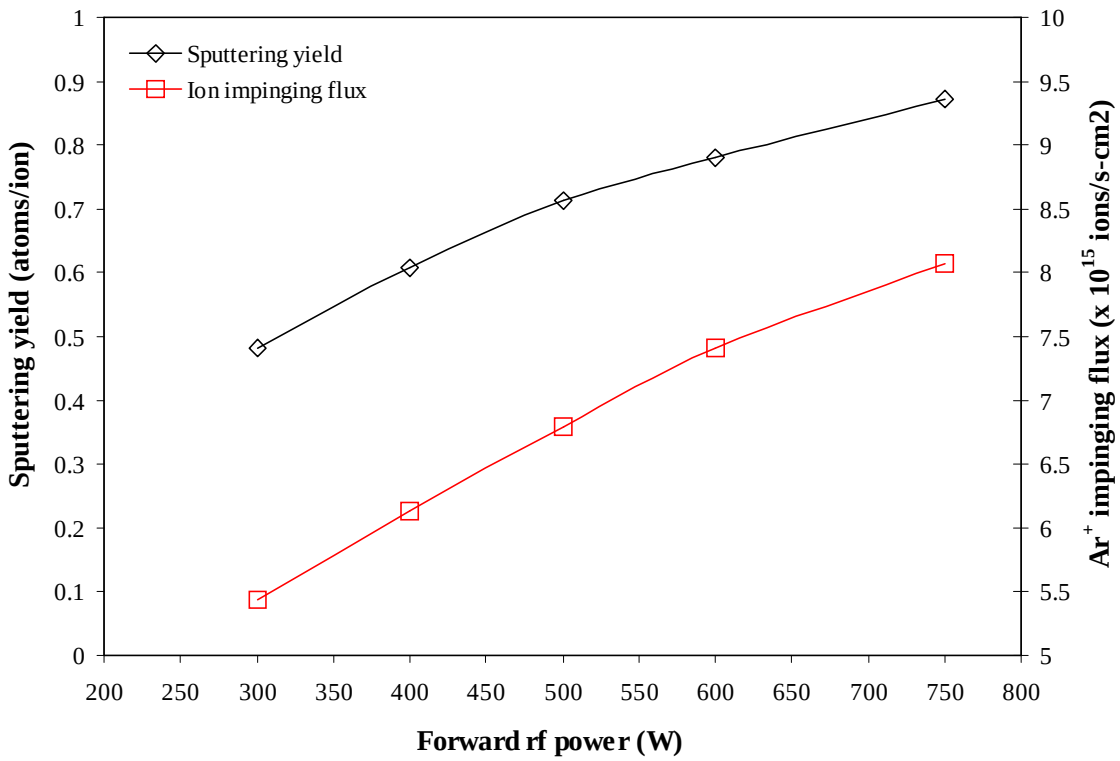

Figure 3-2 Sputtering yield γ of graphite target due to Ar^+ bombardment and Ar^+ impinging flux J_{Ar^+} versus forward rf power under conditions of substrate bias voltage of –200 V, working pressure of 3 mTorr, and gas flow rate of 20 sccm.

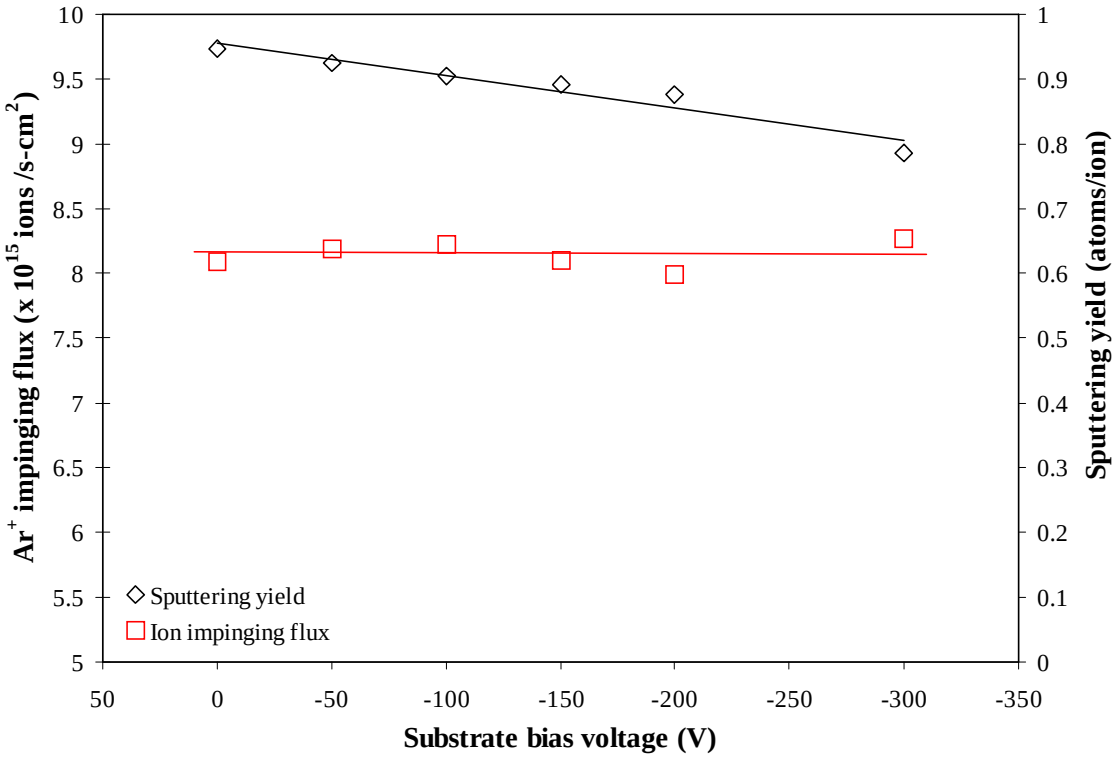

Figure 3-3 Sputtering yields γ of graphite target bombarded by Ar^+ and Ar^+ impinging flux J_{Ar^+} versus substrate bias voltage under conditions of forward rf power of 750 W, working pressure of 3 mTorr, and gas flow rate of 20 sccm.

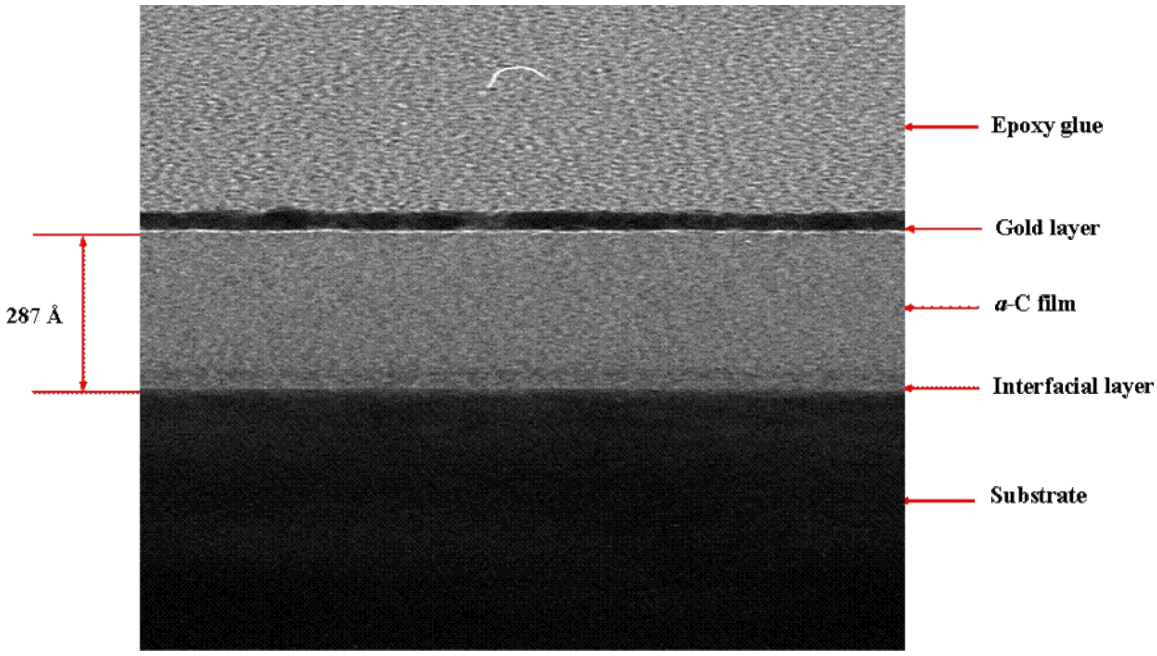

Figure 3-4 Cross-sectional transmission electron microscope image of an *a*-C film deposited under conditions of forward rf power of 750 W, substrate bias voltage of –200 V, working pressure of 3mTorr, gas flow rate of 20 sccm, and deposition time of 3 minutes.

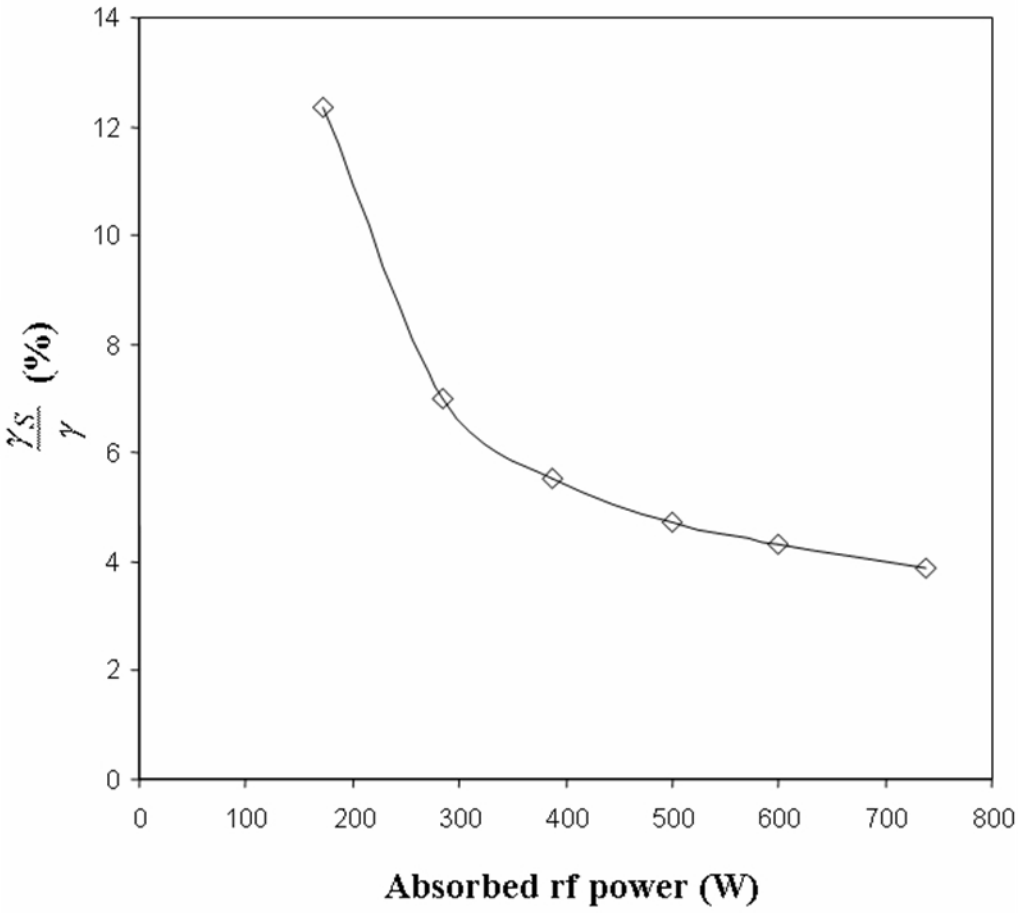

Figure 3-5 Ratio γ_S / γ versus absorbed rf power (Substrate bias voltage fixed at -200 V).

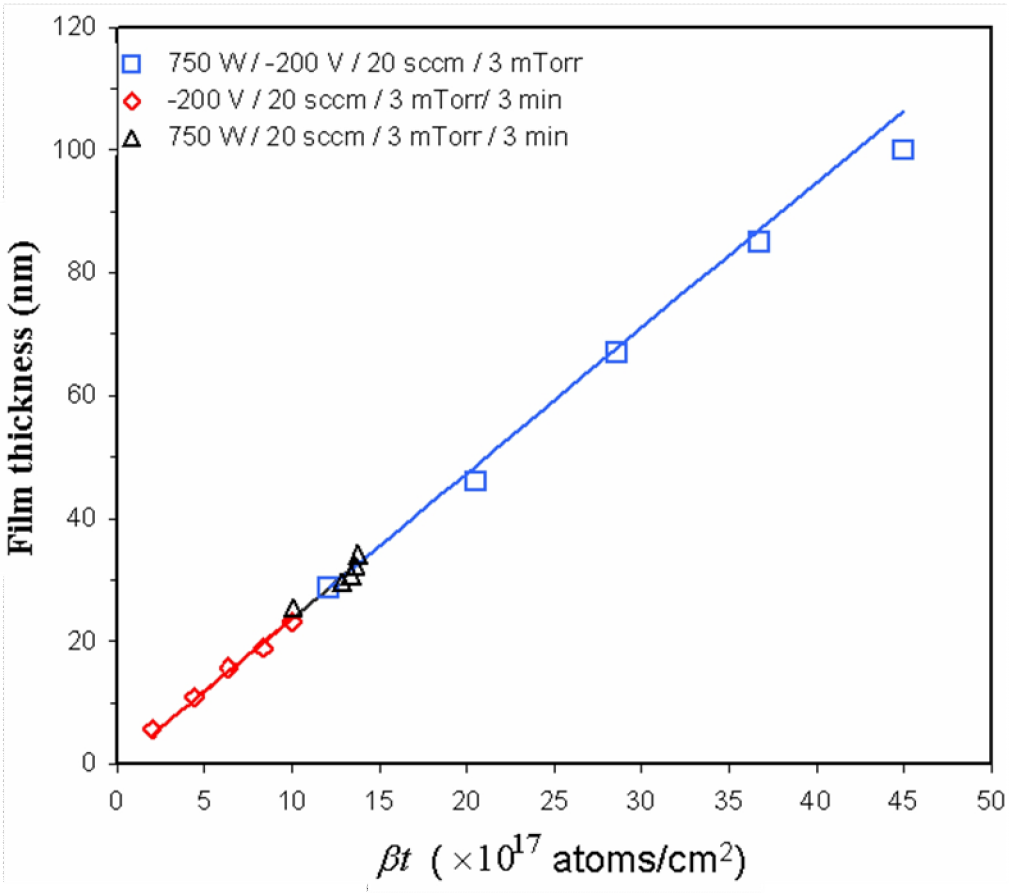

Figure 3-6 Relationship between film thickness and product of sputtering rate and deposition time βt for different deposition conditions. The values of the process parameters fixed in each set of data are listed at the top of the figure.

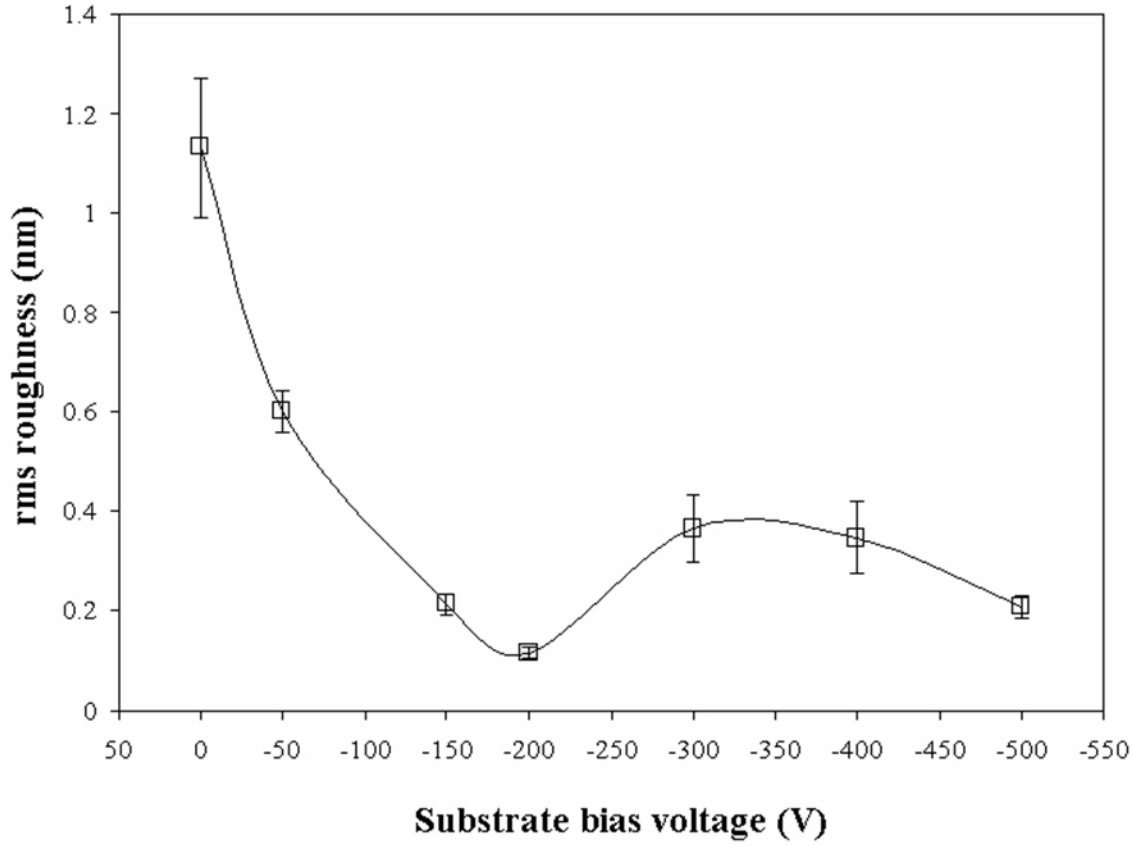

Figure 3-7 Effect of substrate bias voltage on *a*-C film surface roughness for forward rf power of 750 W, working pressure of 3 mTorr, gas flow rate of 20 sccm, and deposition time of 3 minutes.

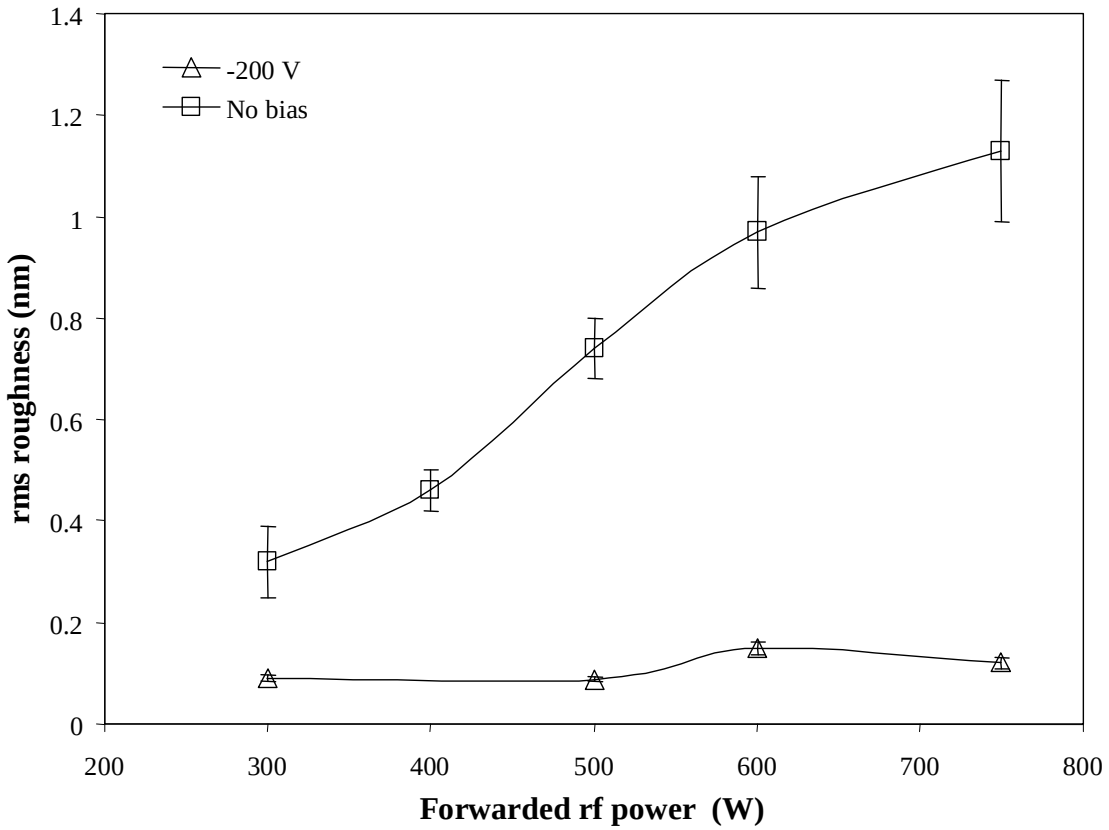

Figure 3-8 Effect of forward rf power on *a*-C film surface roughness for substrate bias voltage equal to -200 W and 0 V, working pressure of 3 mTorr, Ar gas flow rate of 20 sccm, and deposition time of 3 minutes.

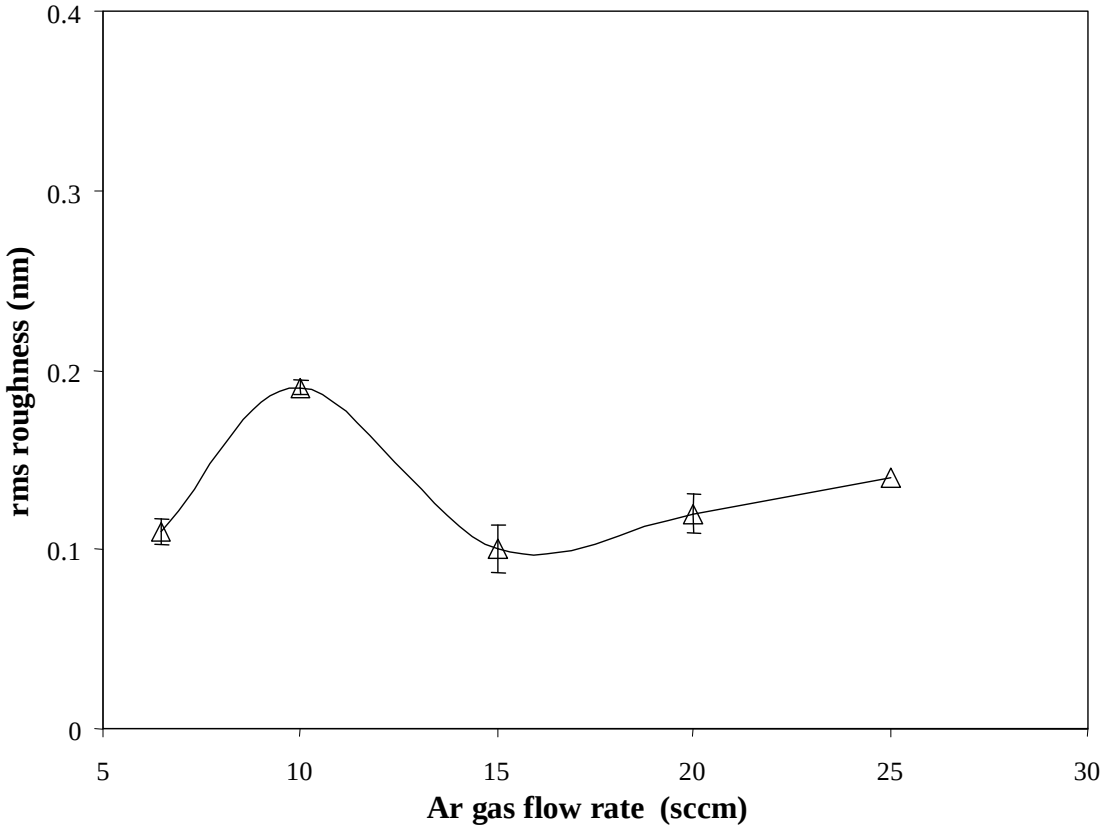

Figure 3-9 Effect of Ar gas flow rate on *a*-C film surface roughness for forwarded rf power of 750 W, substrate bias voltage of -200 W, working pressure of 3 mTorr, and deposition time of 3 minutes.

CHAPTER 4

Compressive Residual Stresses in Sputtered *a*-C Films

4.1 Introduction

Large compressive residual stresses are usually produced in *a*-C films deposited by low-pressure rf sputtering. The effect of compressive residual stresses on the tribological performance of *a*-C films deposited by magnetron sputtering as a protective coating has been studied experimentally (Mounier, et al, 1995; Mounier and Pauleau, 1997). Severe damage and formation of wear debris were attributed to the high level of compressive residual stress in the *a*-C films. The residual stress effect on the tribological performance of thin films has also been examined in theoretical and numerical studies (Hills and Ashelby, 1982; Ye, 2002). Intense Ar^+ bombardment on the growing film surface controls the magnitude of the compressive stress. However, the relationship between Ar^+ bombardment and the compressive residual stress is complicated (Windischmann, 1992; Davis, 1993). Various theories have been proposed to explain the origin and magnitude of the residual stresses in thin films (Machlin, 1995). Numerous techniques have been used to measure the residual stress in thin films (Nix, 1989), such as X-ray diffraction, optical inteferometry, and laser scanning. However, these routine techniques may not be suitable for ultrathin films of thickness of the order of a few nanometers. Small amounts of Ar atoms implanted in the film as stress-sensing probes has been proposed to evaluate residual stresses in ultrathin films (Lu and Komvopoulos, 2000), which is based on the effect of the residual stress on the binding energy shift of Ar atoms.

Compressive residual stresses in rf sputtered *a*-C films deposited on Si(100) substrates under different conditions are systematically studied by experiments in this chapter. The residual stresses are determined by measuring the wafer curvature before and after film deposition. The effect of energetic ion bombardment on the residual stress and the stress relaxation mechanisms, such as thermal spikes and interfacial tension effect, are discussed in the context of the obtained experimental results.

4.2 Experimental Procedures

Five groups of *a*-C films are deposited on 3-inch Si(100) wafers by Ar^+ sputtering of a pure graphite target using a Perkin-Elmer sputtering system without magnetron (Figure 2-1). Before film deposition, the substrate surface is sputter etched for 3 minutes to remove the native oxide layer. All the *a*-C films are synthesized under 3 mTorr working pressure and 20 sccm gas flow rate. The substrate temperature is maintained at room temperature by a cooling system. The details of *a*-C film deposition procedures have been described in section 3.2. Film deposition are performed at five different combinations of forward rf power P_f, substrate bias voltage V_S, and deposition time t: (i) 200 W $\leq P_f \leq$ 750 W, V_S = -200 V, t = 3 minutes; (ii) P_f = 750 W, 0 V $\geq V_S \geq$ -300 V, t = 3 minutes; (iii) P_f = 200 W, 0 V $\geq V_S \geq$ -300 V, t = 3 minutes; (iv) P_f = 750 W, V_S = -200 V, 2 minutes $\leq t \leq$ 11 minutes; (v) P_f = 200 W, V_S = -200 V, 2 minutes $\leq t \leq$ 11 minutes. Hereafter, films produced under these deposition parameters will be referred to group I through V, respectively.

The film thickness t_f is measured directly from cross-sectional images obtained by a high-resolution transmission electron microscope (Philips CM300FEG/UT) with the instrumental resolution equal to 1.7 Å. The wafer thickness t_s is measured with a probe instrument (Millitron), while the wafer curvature radius is determined before and after film deposition by laser scanning (Flexus). The average residual stress σ_r in the films is determined using Stoney equation (Brenner, A. and Senderoff, 1949):

$$\sigma_r = \left(\frac{e}{1-\nu}\right)_s \frac{t_s^2}{6t_f}\left(\frac{1}{r}-\frac{1}{r_o}\right), \tag{4-1}$$

where $\left(\frac{E}{1-\nu}\right)_s$ is the biaxial modulus of the Si(100) substrate (assumed equal to 180.5 GPa (Brantley, 1973)), and r_o and r are the wafer curvature radii before and after film deposition, respectively. The Ar^+ impinging flux J_{Ar^+} is given by Eq. (3-1). Table 4-1 gives the thickness and residual stress in each film in terms of the corresponding deposition conditions.

4.3 Experimental Results

The compressive residual stress in rf sputtered *a*-C films strongly depends on the deposition conditions. It will be shown that the Ar^+ bombardment on the growing film surface not only controls the evolution of the surface topography (Chapter 3) but also the magnitude of the residual stress. The Ar^+ bombardment effect depends on the Ar^+ kinetic energy E_{Ar^+}, impinging Ar^+ flux J_{Ar^+} and bombardment (deposition) time t.

Figure 4-1 shows the effect of the Ar^+ impinging flux J_{Ar^+} on the residual stress in the *a*-C films of group I. Both Ar^+ kinetic energy E_{Ar^+} and duration time t are fixed at

210 eV (V_S = -200 V) and 3 minutes, respectively, in this group of film depositions. It can be seen that the enhancement of the Ar^+ bombardment effect due to the increase of the Ar^+ impinging flux J_{Ar^+} results in the linear increase of the compressive residual stress from 2.36 to 5.89 GPa.

Figure 4-2 shows the dependence of the residual stress on the Ar^+ kinetic energy E_{Ar^+} of *a*-C films (group II and III). The Ar^+ impinging flux J_{Ar^+} during film growth in group II and III are fixed at $\sim 8.2\times10^{19}$ and $\sim 4.5\times10^{19}$ ions/m^2·s, respectively (Table 4-1). In both groups, the bombardment time t during film growth is equal to 3 minutes. In the absence of Ar^+ bombarding during film growth, the residual stress (~ 0.8 GPa) is independent of the forward rf power. However, the dependence of the evolution of the residual stress on the Ar^+ kinetic energy E_{Ar^+} and impinging flux J_{Ar^+} is complex. The compressive residual stress in the *a*-C films deposited under P_f = 750 W (group II) increases first from 0.75 to 6.77 GPa with the increase of the Ar^+ kinetic energy E_{Ar^+} from 10 to 160 eV, and then decreases slightly to 5.89 GPa for E_{Ar^+} > 160 eV, reaching a steady-state of ~ 6 GPa. Although the compressive residual stress in the *a*-C films deposited under P_f = 200 W (group III) also increases initially from 0.83 to 4.83 GPa with the increase of Ar^+ kinetic energy E_{Ar^+} from 10 to 60 eV, it decreases continuously for E_{Ar^+} > 60 eV, indicating the occurrence of stress relaxation. The possible stress relaxation mechanisms are thermal spike processes (Davis, 1993) and interfacial tension effect. These mechanisms will be discussed in detail later.

Figure 4-3 shows the effect of the bombarding time on the residual stress in the *a*-C films synthesized under P_f = 750 W (group IV) and P_f = 200 W (group V). The Ar^+

kinetic energy E_{Ar^+} is fixed at 210 eV (V_S = -200 V) during the film deposition, while the Ar^+ impinging flux J_{Ar^+} during the growth of *a*-C films in group IV and V is fixed at $\sim 8.2\times10^{19}$ and $\sim 4.8\times10^{19}$ ions/m^2·s (Table 4-1). The compressive residual stress in the *a*-C films of group IV increases initially from 5.89 to 11.44 GPa with the increase of the Ar^+ bombardment time, and later decreases slightly to a steady-state value of ~ 9.6 GPa. However, the compressive residual stress in the *a*-C films of group V increases monotonically from 2.36 GPa to a steady-state of ~ 4 GPa.

4.4 Kinetic Energy of Sputtered Carbon Atoms

From the experimental results mentioned above, it is found that Ar^+ bombardment has a significant effect on the compressive residual stress in rf sputtered *a*-C films. Carbon atoms ejected from the graphite target also gain kinetic energy from the Ar^+ sputtering process. The kinetic energy effect of carbon atoms condensing at the film surface on the residual stress requires further examination. The kinetic energy of the carbon atoms condensing at the film surface is a function of the kinetic energy of the carbon atoms ejected from the target and the chamber pressure.

Thompson (1968) proposed a model to describe the energy distribution of sputtered atoms from the target, which yields the following relationship:

$$\frac{dN_E}{N} = \frac{1-\left(\dfrac{(M_1+M_2)^2(E_B+E)}{4M_1M_2E_{ion}}\right)^{1/2}}{E^2(1+\dfrac{E_B}{E})^3}, \qquad (4\text{-}2)$$

where N is the total number of atoms ejected from the target, dN_E is the number of atoms ejected from the target with kinetic energy in the range of E and $E+dE$, M_1 and

M_2 are the masses of the target atoms and incident ions, respectively, E_{ion} is the kinetic energy of incident ions, and E_B is the target surface binding energy. For graphite, E_B = 3.5 eV (Lifshitz, et al, 1990). The kinetic energy E_{Ar^+} of incident Ar+ can be obtained from the target self-bias voltage. For rf sputtered *a*-C films synthesized under conditions of 750 W forward rf power and zero substrate bias, the kinetic energy E_{Ar^+} of Ar^+ impinging on the target surface is ~1755 eV (Table 4-1). The kinetic energy distributions of carbon atoms ejected from the target surface is calculated from Eq. (4-2) and shown in Figure 4-4. The average kinetic energy of carbon atoms calculated from this energy distribution is 24.4 eV.

The kinetic energy of carbon atoms ejected from the graphite target by Ar^+ bombardment decreases progressively during travel across the target-substrate space due to scattering mainly by the Ar gas. As shown below, the energy ratio *r* of a sputtered atom before and after one scattering event is given by (Westwood, 1978)

$$r = \frac{< E_0 >}{< E_1 >} = e^{\omega}, \tag{4-3}$$

where $< E_0 >$ and $< E_1 >$ are the kinetic energies of a sputtered atom before and after scattering, respectively, and parameter ω is given by (Westwood, 1978)

$$\omega = \frac{(\alpha - 1)^2}{2\alpha} \ln(\frac{\alpha + 1}{\alpha - 1}) - 1, \tag{4-4}$$

where α is the mass ratio of the sputtering gas atom to the sputtered atom. For a sputtered carbon atom scattered by Ar gas, ω = -0.494 and r = 0.6099.

The average distance *L* traveled by a sputtered carbon atom after its *nth* scattering event is given by (Westwood, 1978)

$$L = n\lambda\sqrt{2}\cos(\frac{<\theta>}{2}), \tag{4-5}$$

where $<\theta>$ is the spatial average of the scatter angle of carbon atoms due to collisions with Ar atoms, which for carbon-argon system is 78.46°; λ is the mean free path of a sputtered carbon atom traveling through the target-substrate space, given by (Mcdaniel, 1964)

$$\lambda = 2.2 / p \ \text{(cm)}, \tag{4-6}$$

where p is the working pressure in Pa. Therefore, the ratio R_n of the kinetic energy of a carbon atom before and after *n* scatterings is given by

$$R_n = \exp(n\omega) = \exp(-0.205pL). \tag{4-7}$$

In the present sputtering system, the distance L between the target and the substrate is 7 cm, and the working pressure is set at 3 mTorr (0.4 Pa) during film growth. Hence, R_n = 0.56, and the average kinetic energy of carbon atoms condensing at the film surface is approximately equal to 56% of the average kinetic energy of carbon atoms ejected from the target (i.e., 13.7 eV).

The average kinetic energy of sputtered carbon atoms condensing at the film surface is comparable to that of Ar^+ bombarding the film surface (~10 eV) when the substrate is not negatively biased. However, the impinging flux of sputtered carbon atoms is much smaller than that of Ar^+ and the direction of carbon atoms ejected from the target surface is random. Therefore, the residual stress in the film is predominantly affected by the Ar^+ bombardment, while the carbon atom striking effect is secondary.

4.5 Effect of Ar^+ Bombardment

In the absence of substrate biasing, the kinetic energy (~10 eV) of Ar^+ striking the film surface is independent of the rf power and too low to produce a significant bombardment effect. Therefore, the residual stress in the film is independent of the rf power (Figure 4-2). However, the effect of Ar^+ bombardment on the residual stress becomes significant when the substrate is biased negatively during film growth.

As reported previously in this chapter, the experimental results show that the residual stress in sputtered *a*-C films increases with the Ar^+ impinging flux J_{Ar^+} on the film surface, and depends on the Ar^+ kinetic energy E_{Ar^+}. D'Heurle (1970) attributed the origin of a compressive residual stresses in sputtered films to "shot-peening" of energetic particles arriving at the film surface at significant kinetic energy. Since then different models have been proposed for the ion-peening process (Hoffman and Gaertner, 1980; Windischmann, 1987). Windischmann (1987, 1992) used ballistic atomic collisional descriptions to develop a theoretical model that explains the origin of the compressive stresses in sputtered films based on the following assumptions: (i) a volumetric distortion is produced due to the displacement of n atoms per unit volume from their equilibrium positions through a series of primary and recoil collisions, (ii) the volumetric distortion is frozen in place due to insignificant mass transport and defect mobility at low deposition temperatures ($T / T_m < 0.25$, where T is the deposition temperature and T_m is the melting temperature), and (iii) the relative volumetric distortion (strain) is proportional to the fractional number of atoms n / N displaced from their equilibrium positions, where N is the atomic number density of sputtered atoms condensing on the film surface. Therefore, the compressive residual stress in sputtered film is given by

$$\sigma_r = \left(\frac{E}{1-\nu}\right)_f \left(\frac{Kn}{N}\right), \tag{4-8}$$

where $\left(\frac{E}{1-\nu}\right)_f$ is the biaxial modulus of the sputtered film, and K is a proportionality factor. Based on the knock-on linear cascade theory of sputtering (Sigmund, 1981), the number of atoms per unit volume n displaced due to the bombardment effect can be obtained as the product of the forward sputtering yield γ and the ion flux J_{ion} as

$$n = J_{ion}\gamma . \tag{4-9}$$

For the carbon-argon system, n is related to the impinging fluxes of the energetic particles on the *a*-C film and the forward yields and is given by (Mounier and Pauleau, 1996)

$$n = \gamma_{Ar^+} J_{Ar^+} + \gamma_C J_C , \tag{4-10}$$

where γ_{Ar^+} and γ_C are the energetic Ar^+ and carbon atom induced forward sputtering yields on the *a*-C film surface, respectively, and J_C is the carbon atom impinging flux. The forward yield of carbon atoms depends on the incident particle energy E_p, and is given by (Mounier and Pauleau, 1996)

$$\gamma = 4.79\left(\frac{M_C}{M_C + M_P}\right)^{1/2} \frac{(Z_P Z_C)^{1/2}}{\left(Z_P^{2/3} + Z_C^{2/3}\right)^{1/4}} \frac{E_p^{1/2}}{U_o}, \tag{4-11}$$

where M_C and M_p are the atomic masses of carbon and projectile, respectively, Z_C and Z_p are the atomic numbers of carbon and projectile, respectively, and U_0 is the sublimation energy of carbon. Neglecting the effect of the carbon atom striking at the

film surface, the compressive residual stress in the sputtered *a*-C films can be expressed as

$$\sigma_r = 13.36\left(\frac{E}{1-\nu}\right)_f \left(\frac{K}{N}\right)\frac{E_{Ar^+}^{1/2}}{U_o} J_{Ar^+} . \qquad (4\text{-}12)$$

According to Eq. (4-12), the compressive residual stress increases linearly with the Ar^+ impinging flux. The experimental data reported earlier in this chapter are in agreement with Eq. (4-12) (Figure 4-1). However, the compressive residual stress always increases with the Ar^+ kinetic energy E_{Ar^+} according to Eq. (4-12) conversely to the results shown in Figure 4-2. As mentioned previously, the relationship between σ_r and E_{Ar^+} is complex due to stress relaxation during the film growth. The possible mechanisms controlling stress relaxation are thermal spike processes and interfacial tension effect.

The effect of Ar^+ bombardment also depends on the film thickness. The plasma sheath behavior plays an important role in the rf sputtered *a*-C film growth. The plasma sheaths in low-pressure rf discharge can be modeled as pure capacitors C_s when $\omega\tau_i >> 1$, where ω is the frequency of the applied field and τ_i is the ion transit time through the sheath. The sheath behavior can be analyzed using an equivalent electrical circuit of the discharge, and has already been discussed in Chapter 2. The growing *a*-C film and the substrate form a capacitor $C_{f,s}$ because the *a*-C film is a dielectric material. Figure 4-5 shows the equivalent electrical circuit of a single rf power sputtering system. The substrate bias voltage V_S is distributed in the film-substrate capacitor $C_{f,s}$ and the capacitor of the plasma sheath near the substrate C_s. The Ar^+ kinetic energy E_{Ar^+} is determined by the potential V_{sf} between the sheath edge and the growing a-C film

surface. Using the simple electrical analog shown in Figure 4-5, the potential V_{sf} can be expressed by

$$V_{sf} = \frac{C_T}{C_s} V , \tag{4-13}$$

where $C_T = \frac{C_s C_{f,s}}{C_s + C_{f,s}}$, $C_s = \frac{\varepsilon_s \varepsilon_o}{d_s}$, $C_{f,s} = \frac{\varepsilon_f \varepsilon_o}{t_f}$, $V = V_P - V_S$, ε_0 is the electrical permittivity in vacuum, ε_s and ε_f are the dielectric constants of the plasma sheath and the *a*-C film, respectively, and d_s is the thickness of the plasma sheath near the substrate. For rf discharge conditions of 3 mTorr working pressure, 300 K environmental temperature, ~750 W absorbed rf power and 7 cm spacing between the target and substrate, d_s is estimated to be about ~360 μm using Child Law, and ε_s is given by (Lieberman and Lichtenberg, 1994)

$$\varepsilon_s = \frac{e n_0 L}{V} \frac{d_s}{\varepsilon_0}, \tag{4-14}$$

where n_0 is the plasma density, which is a function of the absorbed rf power P_a .

Figure 4-6 shows the variation of the potential V_{sf} with the film thickness for rf discharge conditions of 740 W absorbed rf power and -200 V substrate bias voltage. The kinetic energy E_{Ar^+} decreases continuously with film growth, hence, decreasing the effect of Ar^+ bombardment. The compressive residual stress in the *a*-C films of group IV increases initially with the deposition time from 5.89 to 11.44 GPa, and then decreases slightly when the film thickness above 70 nm, and eventually reaching a steady-state of ~9.6 GPa (Figure 4-3) due to the decrease of E_{Ar^+} from 210 eV to less than 180 eV (Figure 4-6).

4.6 Thermal Spike Effect

As mentioned previously, the prediction based on the Windischmann model that the compressive residual stress always increases with E_{Ar^+} predicted is not supported by the experiments (Figure 4-2). Stress relaxation can occur during film growth. Davis (1993) proposed a model that takes into account the thermal spike effect to explain stress relaxation in a growing film. The carbon atoms displaced due to the knock-on process by both the energetic Ar^+ and the implanted energetic carbon atoms are responsible for the development of the compressive residual stress in the sputtered *a*-C films (Windischmann, 1987, 1992). However, because the implanted carbon atoms are metastable, they can escape to the film surface if they acquire sufficient excitation energy E_0. The kinetic energy of bombarding particles can be transferred to the film atoms by cascade collisions over a very short impact range. The resulting intense local heating (thermal spike effect) provides energy to the metastable atoms in the film to migrate to the surface. The number of atoms n_a acquiring energy greater than the excitation energy E_0 is given by (Seitz and Koehler, 1956)

$$n_a = 0.016\rho(\frac{Q}{E_0})^{5/3}, \tag{4-15}$$

where Q is the energy dissipated in a thermal spike and ρ is a material-dependent of order 1. Assuming that each implanted carbon atom receiving energy greater than E_0 migrates to the film surface, the migration rate of carbon atoms per unit area is given by (Davis, 1993)

$$n_r = 0.016\rho \frac{n}{N} J_{Ar^+} \left(\frac{Q}{E_0} \right)^{5/3}, \tag{2-16}$$

where n is given by Eq. (4-9). The implantation rate of carbon atoms per unit area is given by (Windischmann, 1987, 1992)

$$n_i = 13.36 J_{Ar^+} \frac{E_{Ar^+}^{1/2}}{U_o}. \tag{4-17}$$

When a steady-state is reached between implantation and relaxation processes, the rate difference $n_i - n_r$ is constant, and is given by

$$n_i - n_r = R\frac{n}{N}, \tag{4-18}$$

where R is the constant steady-state rate per unit area at which implanted carbon atoms are incorporated into the film. Combining Eqs. (4-16)-(4-18) gives

$$\frac{n}{N} = \frac{13.36}{U_o} \frac{J_{Ar^+} E_{Ar^+}^{1/2}}{R + 0.016\rho\left(\frac{E_{Ar^+}}{E_o}\right)^{5/3} J_{Ar^+}}. \tag{4-19}$$

Therefore, the compressive stress in sputtered *a*-C films can be obtained by substituting Eq. (4-19) into Eq. (4-8)

$$\sigma_r = K\left(\frac{E}{1-\nu}\right)_f \frac{13.36}{U_o} \frac{J_{Ar^+} E_{Ar^+}^{1/2}}{R + 0.016\rho\left(\frac{E_{Ar^+}}{E_o}\right)^{5/3} J_{Ar^+}}. \tag{4-20}$$

In Eq. (4-20), K, $\left(\frac{E}{1-\nu}\right)_f$, U_0, and ρ are constant, while R, J_{Ar^+}, and E_{Ar^+} depend on the deposition conditions. When $R >> 0.016\rho\left(\frac{E_{Ar^+}}{E_0}\right)^{5/3} J_{Ar^+}$, carbon atom implantation is dominant and, hence, $\sigma_r \propto J_{Ar^+} E_{Ar^+}^{1/2}$. However,

when $R << 0.016\rho\left(\frac{E_{Ar^+}}{E_0}\right)^{5/3} J_{Ar^+}$, carbon atom migration to the film surface is the dominant process and, thus, $\sigma_r \propto E_{Ar^+}^{-7/6}$ (stress relaxation). This explains why the compressive residual stress in the *a*-C films of group III decreases continuously from 4.83 to 2.36 GPa when $E_{Ar^+} > 60$ eV (Figure 4-2).

The compressive residual stress in the *a*-C films of group II is also relaxed due to the thermal spike effect. However, the stress relaxation is weaker than that in the *a*-C films of group III (Figure 4-2). The possible reason for this difference is the film thickness dependence of the thermal spike effect. In low-pressure rf sputtering deposition, Ar^+ bombardment on the growing *a*-C film surface causes cascade collisions between carbon atoms, which diminishes at a characteristic depth Λ below the film surface, defined as the impact depth. Since most of the recoil carbon atoms move only within the impact region, The depth Λ affects the magnitude of the residual stress This phenomenon is shown schematically in Figure 4-7. When the film thickness is less than the impact depth ($t_f < \Lambda$), the recoil carbon atoms can only migrate to the film surface because it is more difficult to penetrate the single crystal Si(100) substrate (Figure 4-7 a). This process results in significant relaxation of the compressive residual stress in the film. This is the case in the present films discussed above. When the film thickness exceeds the impact depth ($t_f > \Lambda$), some of the recoil carbon atoms can migrate into the bulk of the film resulting in film densification and a decrease of thermal spike effect on stress relaxation (Figure 4-7 b) This explains the less pronounced stress relaxation in the *a*-C films of group III (Figure 4-2).

4.7 Interfacial Tension Effect

A thin interfacial layer is formed during the initial stage of *a*-C film growth by rf sputtering. Davis, Knowles and Amaratunga (1995) observed the formation of a 5-nm-thick interfacial layer in *ta*-C films deposited by filtered cathodic arc apparatus using a transmission electron microscope. Logothetidis, Gioti and Patsalas (2001) studied real-time growth of *a*-C films deposited by sputtering using *in-situ* ellipsometer, and observed a two-stage growth process. In the initial stage of film nucleation and coalescence encountered up to a film thickness of ~5 nm, the film growth rate was low, compared to the film growth rate at a later stage. Cross-sectional images of the rf sputtered *a*-C films of this study obtained with a high-resolution transmission electron microscope (Philips CM300FEG/UT) reveal the existence of a ~37-Å-thick interfacial layer between the *a*-C films and the Si(100) substrate (Figure 4-8). It is believed that the interfacial layer enhances the adhesion of the *a*-C film to the Si(100) substrate and relaxes the compressive residual stress (Kelires, Gioti and Logothetidis, 1999). During the initial stage of *a*-C film growth, the bond lengths of carbon atoms must accommodate those of silicon atoms in the outermost layer of the substrate. Thus, due to the lattice mismatch, a tensile residual stress evolves in the interfacial layer. Therefore, the thinner the film, the larger the effect of the tensile stress in the interfacial layer. As the film thickness increases above ~7 - 8 Å, a compressive stress develops progressively in the film because the tensile stress in the interfacial layer is exceeded by the compressive stress in the growing film generated by implanted atoms through the knock-on process (Windischmann 1987, 1992). Therefore, compressive stress relaxation due to the tensile stress in the interfacial layer can only be observed with ultrathin films. The *a*-C films of

group V are less than 20 nm in thickness (Table 4-1). The thickness of the first two samples is 36 Å and 56 Å, respectively. Considering that the thickness of the interfacial layer is ~37 Å in all cases, the compressive residual stress in these two *a*-C films of 2.72 and 2.36 GPa, respectively, represents the compressive stress in the interfacial layer. With the increase of the deposition time, the compressive residual stress attains a steady-state of ~4 GPa (Figure 4-3 and Table 4-1). The relatively low compressive residual stress is attributed to the counter effect of the tensile stress in the interfacial layer. This stress relaxation effect due to the interfacial tensile stress is not observed in the *a*-C films of group IV (Figure 4-3) due to the large thickness of these films (Table 4-1).

4.8 Summary

In this chapter, the development of a compressive residual stress in rf sputtered *a*-C films is examined in light of stress measurement and results from an analysis of the effects of the Ar^+ bombardment, thermal spike process, and tensile stress in the interfacial layer. It is shown that the residual stress is essentially affected by the Ar^+ kinetic energy, impinging flux, and energetic particle bombardment time on the growing film surface. However, in the absence of Ar^+ bombardment (zero substrate bias voltage) the relatively low compressive residual stress (~0.8 GPa) is found to be independent of the Ar^+ impinging flux. It is also shown that carbon atom impingement is secondary compared to that of Ar^+ bombardment. A high compressive residual stress (~10 GPa) is produced with intensive Ar^+ bombardment on the growing *a*-C films. The origins and evolution of the compressive residual stress are explained in terms of Ar^+ bombardment. A film thickness dependence of the Ar^+ bombardment effect is observed for relatively thick *a*-C films (i.e.,

t_f > 70 nm). The compressive residual stress in rf sputtered *a*-C film can be relaxed by either thermal spike processes or the tension stress arising in the ~37-Å-thick interfacial layer bonding the *a*-C film to the Si(100) substrate..

Table 4-1 Thickness and compressive residual stresses

Group	Forward rf power (W)	Absorbed rf power (W)	Substrate bias (V)	Target bias (V)	Ion flux (x 10^{19} ions/m^2-s)	Deposition time (min)	Thickness (nm)	stress (GPa)
I	200	172.5	-200	-499	4.68	3	5.6	-2.36
	300	285	-200	-790	5.48	3	10.9	-3.1
	400	388	-200	-1000	6.17	3	15.6	-4.26
	500	500	-200	-1199	6.83	3	18.9	-4.75
	600	600	-200	-1340	7.45	3	23.1	-4.92
	750	746	-200	-1550	8.16	3	28.7	-5.89
II	750	715	-300	-1345	8.32	3	26.6	-6.22
	750	745.5	-150	-1600	8.15	3	29.6	-6.77
	750	747.5	-100	-1630	8.27	3	30.8	-6.14
	750	746.5	-50	-1685	8.23	3	32.2	-4.53
	750	741.5	0	-1745	8.13	3	34.1	-0.75
III	200	188	-150	-650	4.47	3	7.2	-4.11
	200	196.5	-100	-730	4.5	3	8.5	-4.5
	200	197.5	-50	-795	4.45	3	9.2	-4.83
	200	198	0	-885	4.26	3	9.8	-0.83

Table 4-1 Thickness and compressive residual stresses (Cont'd)

Group	Forward rf power (W)	Absorbed rf power (W)	Substrate bias (V)	Target bias (V)	Ion flux (x 10^{19} ions/m^2-s)	Deposition time (min)	Thickness (nm)	stress (GPa)
IV	750	747	-200	-1540	8.22	5	48.6	-8.66
	750	748	-200	-1540	8.23	7	67.8	-11.4
	750	746	-200	-1550	8.16	9	87	-9.78
	750	745	-200	-1555	8.12	11	106.5	-9.55
V	200	180	-200	-500	4.88	2	3.6	-2.72
	200	172.5	-200	-499	4.68	3	5.6	-2.36
	200	176	-200	-499	4.78	5	8.8	-3.86
	200	180	-200	-500	4.88	7	12.7	-3.64
	200	178	-200	-500	4.83	9	16.1	-4.27
	200	179	-200	-499	4.86	11	19.8	-3.89

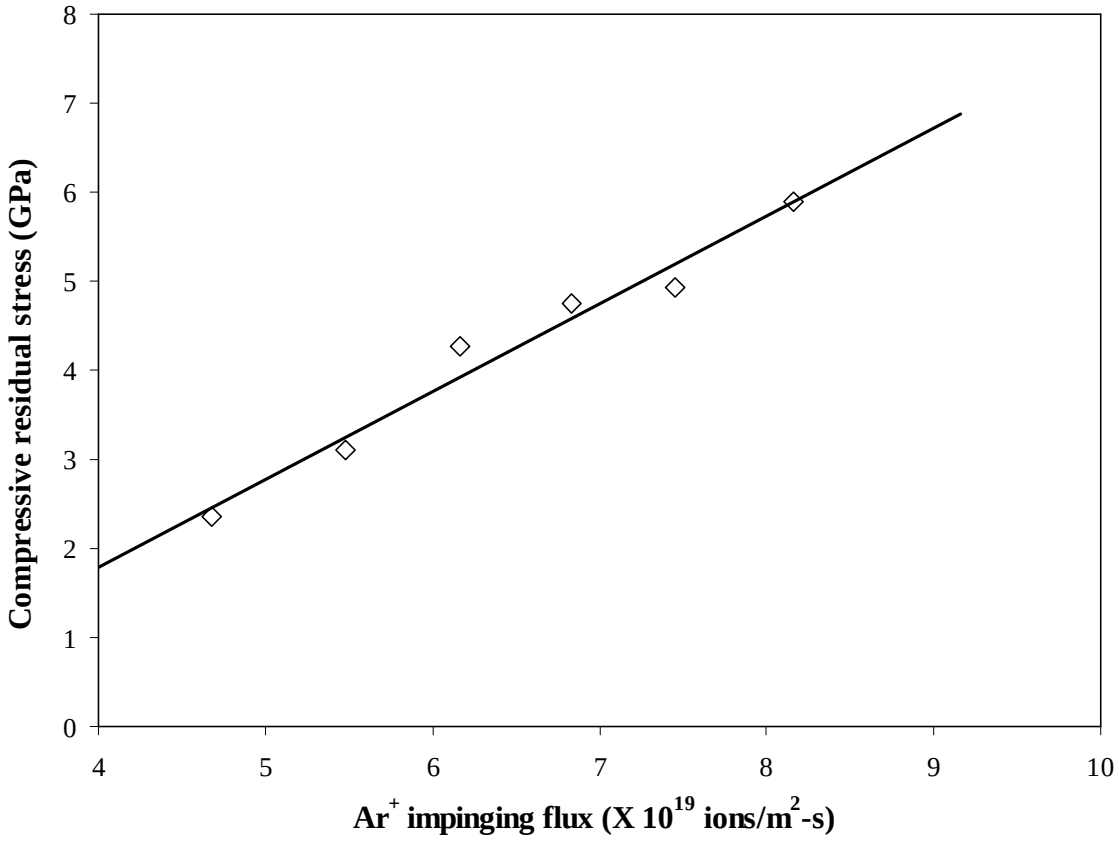

Figure 4-1 Effect of Ar^+ impinging flux J_{Ar^+} on compressive residual stress in sputtered *a*-C films synthesized under conditions of -200 V substrate bias, 3 mTorr working pressure, 20 sccm gas flow rate, and 3 minutes deposition time (Group I).

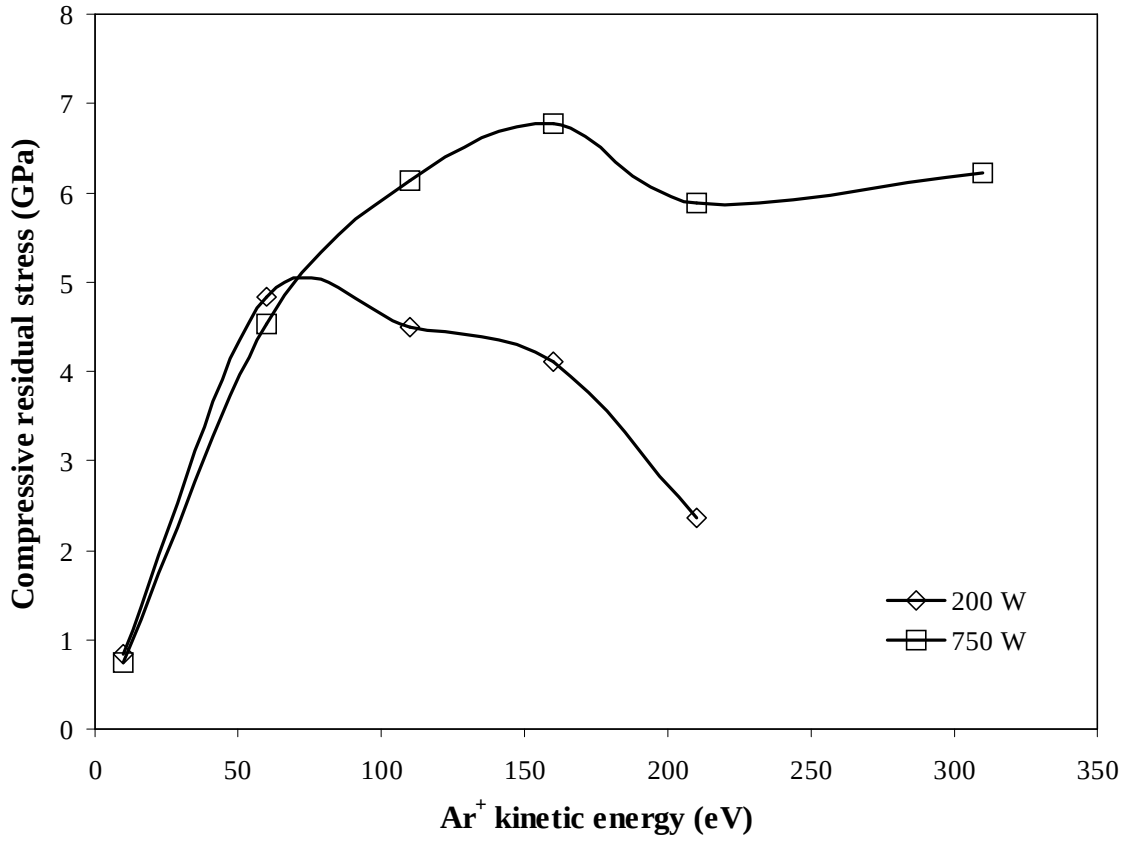

Figure 4-2 Effect of Ar^+ kinetic energy E_{Ar^+} on compressive residual stress in the *a*-C films synthesized under conditions of 750 W (group II) and 200 W (group III) forward rf power, 3 mTorr working pressure, 20 sccm gas flow rate, and 3 minutes deposition time.

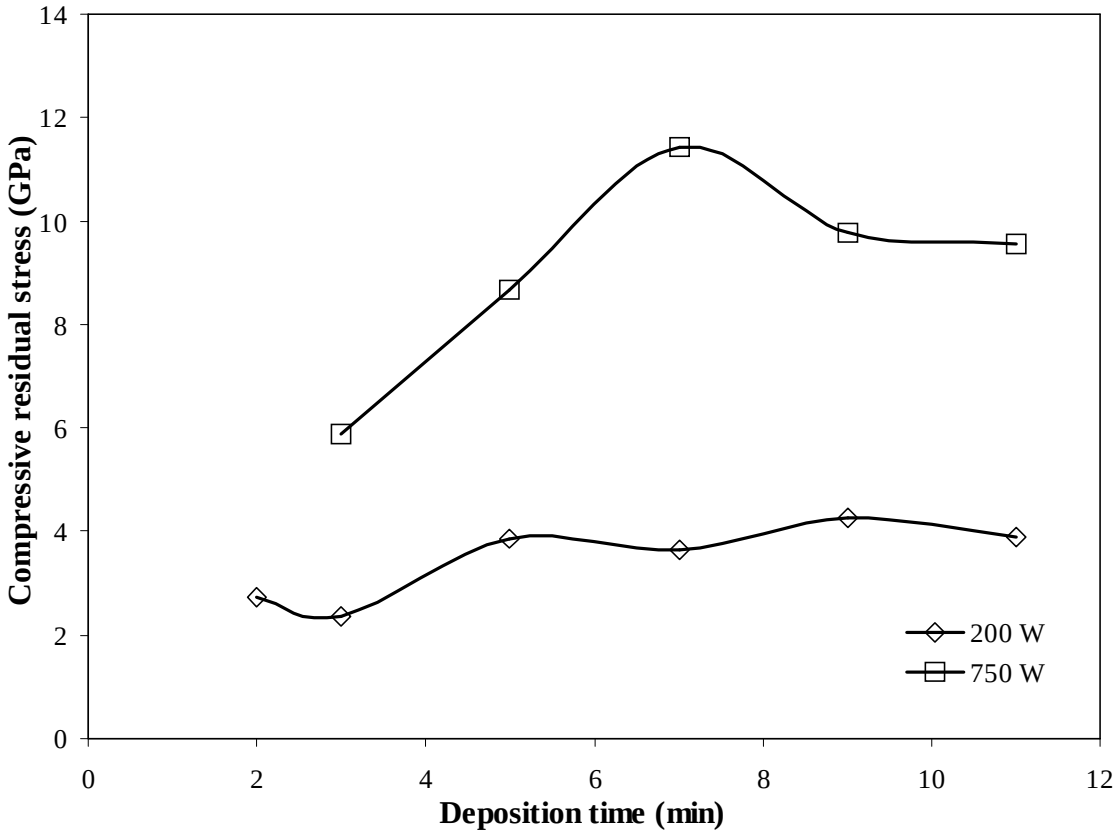

Figure 4-3 Effect of Ar^+ bombardment time t on compressive residual stress in the *a*-C films synthesized under conditions of 750 W (group IV) and 200 W (group V) forward rf power, 3 mTorr working pressure, 20 sccm gas flow rate, and deposition time varied between 2 and 11 minutes.

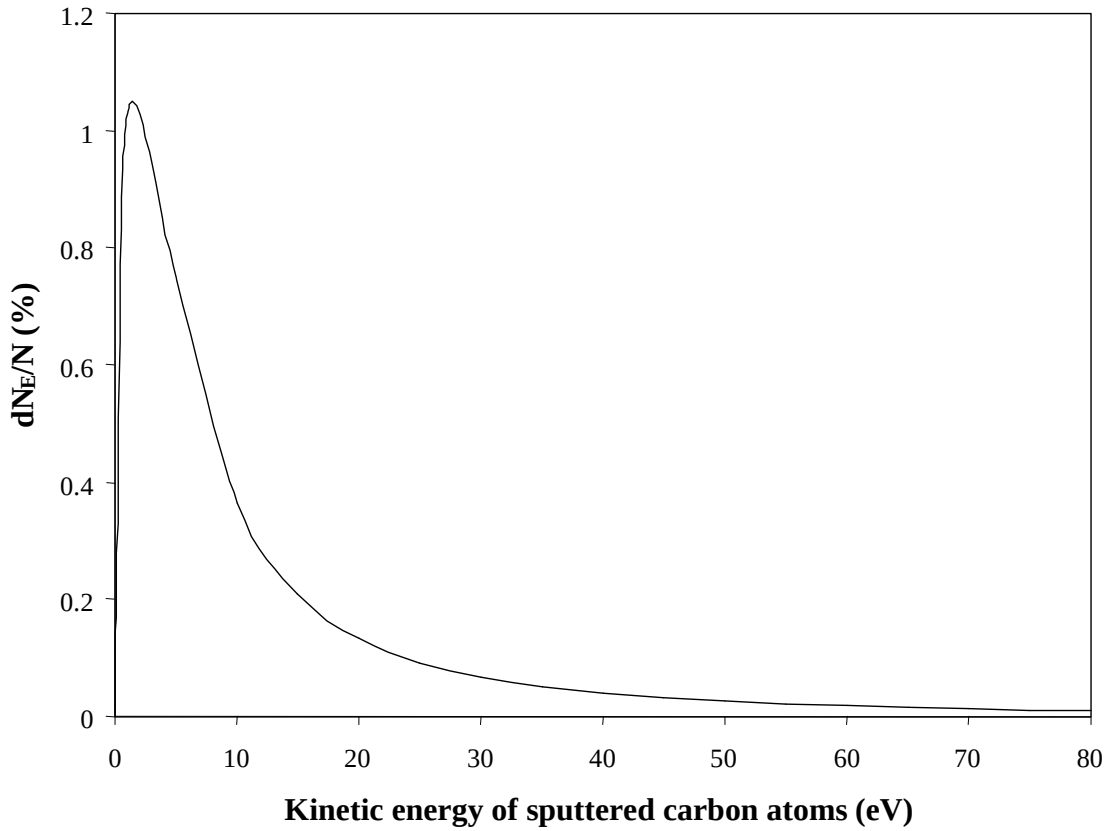

Figure 4-4 Distribution of kinetic energy of carbon atoms sputtered from the graphite target by Ar^+ sputtering of energy $E_{Ar^+} \approx 1755\,\text{eV}$ obtained from Eq. (4-2).

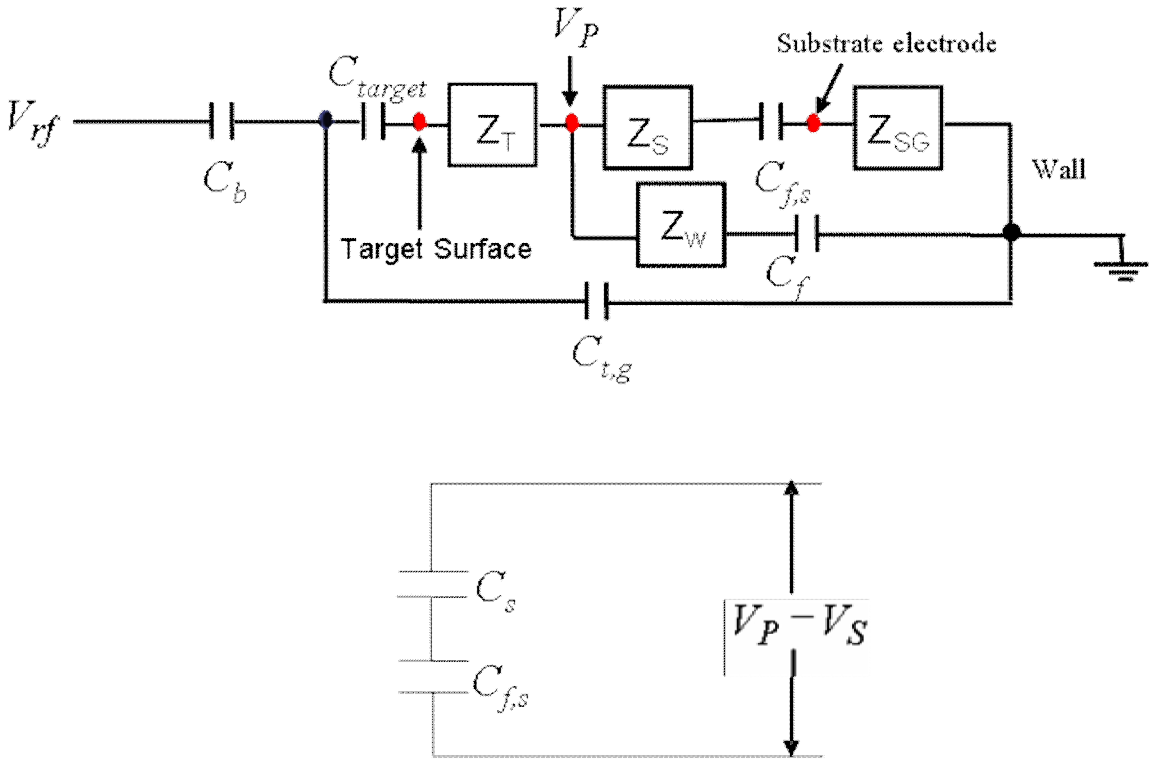

Figure 4-5 Equivalent electrical circuit of a single rf power sputtering system. The impedances of Z_T, Z_S, Z_{SG} and Z_W are defined in Figure 2-3. C_b is the capacitance using to block dc current, C_s is the capacitance of plasma sheath near the substrate, $C_{f,s}$ is the capacitance between *a*-C film and substrate surface, C_{target} is the e capacitance of target, $C_{t,g}$ is the capacitance between target and ground, C_f is the capacitance of thin film on the wall. V_P, V_S and V_{rf} : the potentials of bulk plasma, substrate and rf power supply, respectively.

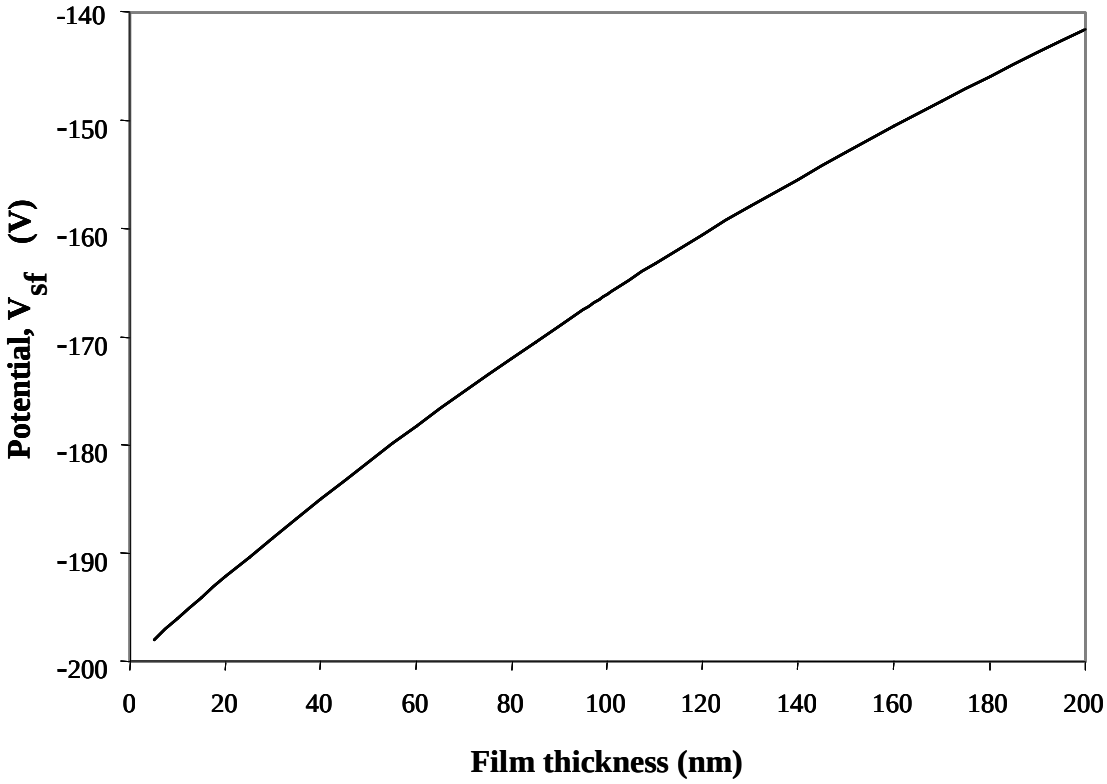

Figure 4-6 The potential V_{sf} between the plasma sheath edge near the substrate and the film surface versus film thickness.

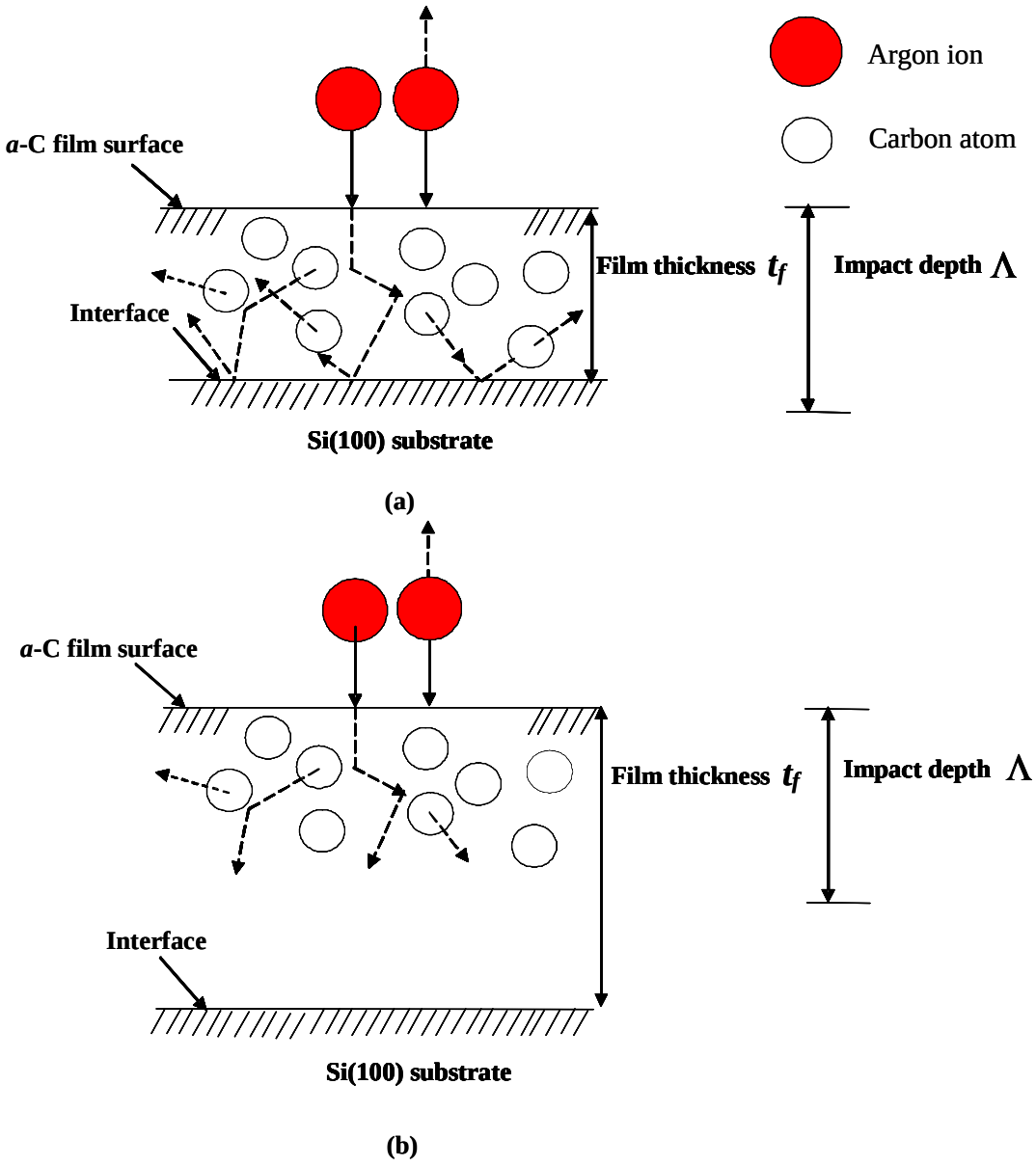

Figure 4-7 Film thickness dependence of the thermal spike effect.

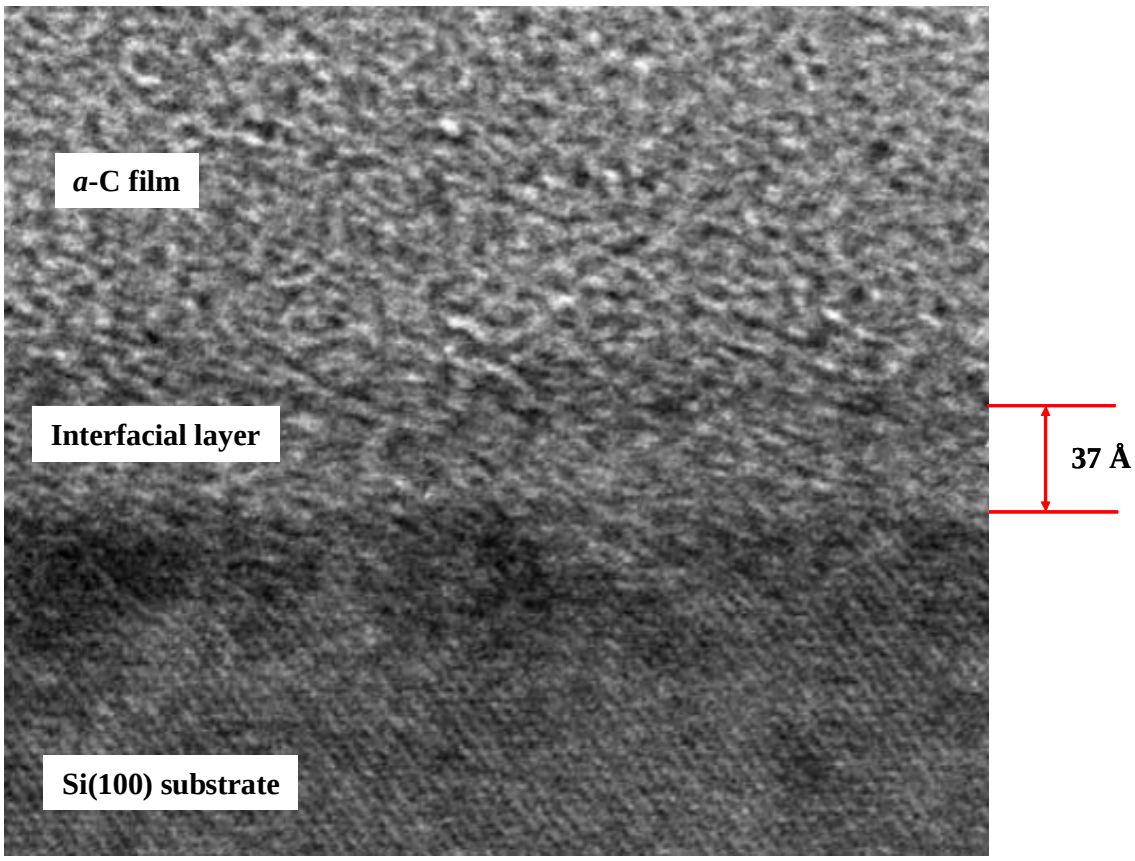

Figure 4-8 Cross-sectional transmission electron microscope image of rf sputtered *a*-C film deposited on Si(100) substrate under conditions of 750 W forward rf power, -200 V substrate bias voltage, 20 sccm gas flow rate, 3 mTorr working pressure, and 3 minutes deposition time.

CHAPTER 5

Transmission Electron Microscopy and Electron Energy Loss Spectroscopy Analysis of Sputtered *a*-C Films

5.1 Introduction

The microstructures of diamondlike carbon (DLC) films greatly affect their mechanical properties. Numerous analytical methods (Lifshitz, 1996, 1999; Robertson, 2002) have been used to characterize the microstructures of DLC films, including Raman spectroscopy, electron energy loss spectroscopy (EELS), transmission electron microscopy (TEM), and X-ray photoelectron spectroscopy (XPS). These microanalysis studies have shown the existence of both trigonal (sp^2) and tetrahedral (sp^3) atomic carbon bonds in DLC films, and that the film properties are functions of the sp^3/sp^2 ratio, which is strongly dependent on deposition method and process conditions.

Transmission electron microscopy is a powerful technique for investigating the microstructures of thin films. Lioutas et al. (1998) used TEM to investigate structures of hydrogen-free *a*-C films deposited by radio-frequency (rf) magnetron sputtering. Large amounts of sp^3 carbon were observed in dark-field cross-sectional transmission electron microscope images obtained with the objective aperture admitting only the 111 diamond reflection. Komninou et al. (2000) examined the microstructures of *a*-C films of thickness equal to 200 Å deposited on Si(001) by rf magnetron sputtering using TEM, X-ray diffraction, and X-ray reflectivity and found that the films contained platelet microcrystallites oriented parallel to the film surface. Davis, Knowles and Amaratunga (1995) studied the cross-sectional structures of tetrahedral carbon (*ta*-C) films

synthesized by filtered cathodic arc deposition using TEM and reported the formation of a ~50 Å thick interfacial layer. Ramírez, Itoh and Sinclair (1999) investigated the crystallization of *a*-C films deposited by dc magnetron sputtering on magnetic media and obtained transmission electron microscope micrographs that showed an increase in the graphite content in the film region adjacent to the magnetic medium for annealing temperature of ~400 ˚C. The microstructure changes suggested that metals in the magnetic layer mediated graphitization, similar to the behavior of other eutectic metal metalloid systems. Analytical electron microscope can be used to obtain EELS spectra. By studying K ionization edge in EELS, the type of carbon bonding can be analyzed quantitatively (Berger, McKenzie and Martin, 1988; Fallon, et al., 1993; Bruley, et al., 1995). The cross-sectional profile of sp^3 content in *ta*-C films synthesized by filtered cathodic arc deposition obtained by EELS revealed a three-layer structure, consisting of a very thin sp^2-rich surface layer, an underlayer with relatively high sp^3 content, and a thin interfacial layer (Davis, Amaratunga and Knowles, 1998).

In this chapter, hydrogen-free ultrathin *a*-C films deposited on Si(100) by rf sputtering and film cross-sectional images obtained by a high-resolution transmission electron microscope are discussed. In addition, EELS results of the microstructures of sputtered *a*-C films near the film surface and in the bulk of film, as well as the interfacial layer between the film and silicon substrate are presented to elucidate structural differences through the film thickness. Plate-like nanocrystallites randomly distributed in the *a*-C films and oriented with their {111} planes parallel to film surface are discovered. Their unexpected formation is discussed in terms of important sputtering phenomena.

5.2 Experimental Procedures

Three series of sputtered *a*-C films are synthesized on Si(100) wafers. Details about the film deposition procedure have been given in section 3.2. A series of films are deposited under conditions of 200-750 W forward rf power, substrate bias voltage equal to –200 V, and deposition time fixed at 3 minutes. In another deposition series, the forward rf power and deposition time are maintained constant at 750 W and 3 minutes, respectively, and the substrate bias voltage is varied between 0 and –300 V. In a third series of depositions, films are synthesized at 750 W forward rf power, –200 V substrate bias voltage, and deposition time in the range of 5-11 minutes. All film depositions are performed under working pressure and Ar gas flow rate equal to 3 mTorr and 20 sccm, respectively. Table 5-1 gives the deposition conditions and thickness of the sputtered *a*-C films.

Film thicknesses are measured directly from the cross-sectional transmission electron microscope images. The film thickness values given in Table 5-1 are obtained as the sum of the thickness of the *a*-C film and interfacial layer. The cross-sectional microstructures of the sputtered *a*-C films are studied by a high-resolution transmission electron microscope (Philips CM300FEG/UT) with the instrumental resolution equal to 1.7 Å. Figure 5-1 shows schematically the main process steps involved in the fabrication of TEM specimens (Williams and Carter, *I: Basics*, 1996). Bright-field cross-sectional transmission electron microscope images are obtained for incident electron beam aligned parallel to the [011] zone axis of the single crystal silicon microstructure. Electron energy loss spectroscopy (EELS) analysis is performed using an analytical electron microscope

(Philips CM200FEG) with focused probe size of 10 Å, equipped with a Gatan imaging filter of energy resolution equal to 0.9 eV.

5.3 Bright-Field TEM Analysis of Sputtered *a*-C Films

The contrast in transmission electron microscope images is due to spatial variations in the phase and the amplitude of the transmission function, resulting from the elastic interaction of incident electrons with the sample. Image contrast is due to changes in both amplitude and phase of the electron wave as it travels through the sample. The image contrast C is defined as (Williams and Carter, *III: Imaging*, 1996)

$$C = \frac{I_1 - I_2}{I_2} = \frac{\Delta I}{I_2}, \tag{5-1}$$

where ΔI is the difference in the electron intensity I between two adjacent areas 1 and 2. Amplitude contrast is due to the electron loss as a result of the obstruction by the objective aperture, while diffraction contrast is a consequence of the electron scattering due to interaction with crystalline regions. Since electron scattering in amorphous materials is observed as incoherent elastic scattering in bright field, diffraction contrast is not obtained and the mass-thickness contrast dominates in bright-field transmission electron microscope imaging.

The phenomenon responsible for the image contrast in TEM due to variations in mass density and sample thickness is depicted schematically in Figure 5-2. When electrons pass through an amorphous material they are scattered off the incident axis by elastic nuclear interactions, a phenomenon known as Rutherford scattering. The strength of Rutherford scattering strongly depends on the atomic number Z, mass density ρ, and

sample thickness t. Thicker samples or higher-Z regions promote electron scattering as opposed to thinner samples and/or lower-mass regions. Therefore, in the case of a thicker sample and/or higher-Z regions in a sample, fewer forward-scattered electrons are obtained on the equivalent area of the image plane, which, therefore, appears darker in the bright-field image. If inelastic scattering is neglected for simplicity, the decrease in the number of electrons passing through the objective aperture and producing the bright-field image is given by (Williams and Carter, *III: Imaging*, 1996)

$$\frac{dn}{n} = -\frac{N_o}{A}\sigma(\beta)d(t\rho), \tag{5-2}$$

where n is the number of electrons at a given location in the sample, dn is the number of electrons scattered through an angle greater than β from the incident electron beam, N_o is the Avogadro number, A is the atomic weight, and $\sigma(\beta)$ is the probability for an electron to be scattered through an angle greater than β, expressed as

$$\sigma(\beta) = 2\pi\int_{\beta}^{\infty}|f(\theta)|^2\theta d\theta, \tag{5-3}$$

where $f(\theta)$ is the atomic scattering factor. Integration of Eq. (5-2) gives

$$N = n_o \exp(-\frac{N_o}{A}\sigma\chi), \tag{5-4}$$

where N is the number of electrons reaching the image plane, n_o is the number of incident electrons, and χ is the mass-thickness of the sample given by $\chi = t\rho$. According to Eq. (5-4), the greater the mass-thickness, the darker the region in the bright-field transmission electron microscope image.

Figure 5-3 shows a cross-sectional image that reveals a two-layer structure consisting of an interfacial layer and the *a*-C film. The very thin surface layer with

relatively high sp^2 content predicted by the subplantation model (Lifshitz, Kasi and Rabalais, 1989; Lifshitz, et al, 1990; Robertson, 1994, 1996; Hofsäss, et al, 1998) is not observed in Figure 5-3. Similar cross-sectional structures are observed with all the other *a*-C films (Table 5-1). These TEM results suggest that the cross-sectional structure of rf sputtered *a*-C films differs from that of *ta*-C films synthesized under much higher energetic ion bombardment, such as ion implantation and filtered cathodic arc depositions.

5.4 EELS Analysis of Sputtered *a*-C Films

The carbon K absorption edge obtained by EELS has been widely used to analyze the content of sp^2 and sp^3 carbon hybridizations in thin films (Berger, McKenzie and Martin, 1988; Yuan, et al., 1992; Fallon, et al., 1993; Bruley, et al., 1995; Davis, Amaratunga and Knowles, 1998). Bruley et al. (1995) used EELS to quantitatively study the microstructure of DLC films and observed that the spectra of sp^3- and sp^2-rich films exhibited similarities with those of diamond and graphite, respectively. The spectrum of graphite within 30 eV from the edge can be separated in two broad peaks corresponding to π^* states between 282 and 288 eV and σ^* states between 290 and 320 eV. However, only σ^* peak between 289 and 320 eV can be found in the diamond spectrum. Microstructures of *a*-C film can be analyzed quantitatively by calculating the relative intensities of π^* and σ^* components and comparing the ratio of these intensities to those of graphite and diamond containing 100% sp^2 and sp^3 carbon bonding, respectively.

Representative EELS results of a sputtered *a*-C film obtained near the film surface, at the center of the film, and from the interfacial layer are presented in Figure 5-4. The

EELS spectra are obtained after smoothly subtracting the background intensities caused by multi-scattering events. The background intensity I can be expressed as (Williams and Carter, *IV: Spectrometry*, 1996)

$$I = \alpha \Delta E^{-\gamma}, \tag{5-5}$$

where α and γ are fitting parameters and ΔE is the electron energy loss. The EELS spectrum obtained from the interfacial layer differs from that of the bulk (center) of the *a*-C film. However, the EELS spectrum obtained near the surface shows small differences compared to that of the center region of the film. The comparison of the EELS spectra obtained from the interfacial layer, near surface region, and at the bulk of this sputtered *a*-C film reveals a two-layer cross-sectional structure, in agreement with the bright-field TEM results presented earlier. The same conclusion is reached after comparing the EELS spectra of another sputtered *a*-C film deposited under much lower forward rf power (i.e., 300 W) and all other deposition conditions identical to those used to synthesize the film shown in Figure 5-3.

5.5 TEM Analysis of the Interfacial Layer

Davis, Knowles and Amaratunga (1995) performed cross-sectional TEM analysis of the microstructures of *ta*-C films synthesized by filtered cathodic arc deposition and observed the presence of a ~50 Å thick interfacial layer. Logothetidis, Gioti and Patsalas (2001) used an *in-situ* ellipsometer to investigate the growth of *a*-C films deposited by rf magnetron sputtering and discovered a two-stage film growth process involving nucleation and coalescence of carbon islands at a relatively low rate up to a film thickness of ~50 Å, followed by a faster growth for thicker films. Figure 5-5 shows a

high-resolution cross-sectional transmission electron microscope image of the sputtered *a*-C film shown in Figure 5-3. A thin layer of ~35 Å in thickness can be seen between the *a*-C film and the Si(100) substrate. The greater darkness of the interfacial layer reveals a mass density higher than that of the *a*-C film, as predicted by Eq. (5-4). This layer, believed to consist of Si, *a*-C, and SiC, plays an important role in the adhesion of the *a*-C film to the Si(100) substrate and the accommodation of the residual stress in the film (Davis, Knowles and Amaratunga, 1995; Kelires, Gioti and Logothetidis, 1999; and section 4.7 in this dissertation).

The fact that the thickness of the interfacial layer is found to be equal to ~35 Å in all the sputtered *a*-C films of this study regardless of the deposition conditions indicates that the film nucleation is mainly controlled by the substrate surface conditions. The relatively thinner interfacial layer obtained in this study than that in previous studies (~50 Å) (Davis, Knowles and Amaratunga, 1995; Logothetidis, Gioti and Patsalas, 2001) is attributed to differences in the Si(100) substrate surface condition, controlled by the cleaning process used in each study. The substrate surface is heterogeneous comprising different surface sites, such as terrace, kink, ledge, vacancy, ledge-adatom, and adatom (Somorjai, 1972). In light of the governing thermodynamic relationships, carbon atom adsorption and bonding with the heterogeneous substrate surface is a spontaneous and highly exothermic process. Heterogeneous film nucleation depends on surface tension at vapor/film, film/substrate, and substrate/vapor interfaces, γ_{vf}, γ_{fs}, and γ_{sv}, respectively, contact angle θ, and change of chemical free energy ΔG_V due to the gas-solid transformation, and can be described by the free-energy change ΔG as (Ohring, 1992)

$$\Delta G = a_3 r^3 \Delta G_V + a_1 r^2 \gamma_{vf} + a_2 r^2 (\gamma_{fs} - \gamma_{sv}), \qquad (5\text{-}6)$$

where $a_1 = 2\pi(1-\cos\theta)$, $a_2 = \pi \sin^2\theta$, $a_3 = \pi(2-3\cos\theta+\cos^3\theta)/3$, r is the average size of nucleating film islands, and ΔG_V is given by

$$\Delta G_V = -\frac{k_B T}{\Omega}\ln(1+s), \tag{5-7}$$

where k_B is the Boltzmann constant, T is the temperature, Ω is the atomic volume, and $s = (p_v - p_s)/p_s$ is the vapor supersaturation, where p_v and p_s denote the pressure in supersaturated vapor and the vapor pressure above the solid, respectively. Before film deposition, the Si(100) substrate surface is sputter-etched for 3 minutes to remove the native oxide layer. This cleaning process is carried out at 250 W forward rf power, 3 mTorr working pressure, and 20 sccm gas flow rate in a pure Ar plasma environment. Hence, by controlling the substrate surface condition before film deposition, the same interfacial layer is produced in all the samples of this study.

5.6 Crystalline Nanostructures in Sputtered *a*-C Films

High-resolution cross-sectional transmission electron microscope images reveal that the sputtered *a*-C films possess mainly amorphous microstructures containing randomly distributed plate-like nanocrystallites of average size equal to ~35 Å oriented parallel to the film surface (Figure 5-6). The calculated fast Fourier transform (FFT) patterns corresponding to nanocrystalline carbon and *a*-C regions are shown in Figure 5-7. The FFT pattern of the *a*-C matrix reveals a diffuse ring pattern, while the nanocrystalline carbon produces a bright set at $\pm g_1$ and the other a dimmer set at $\pm g_2$ in addition to the diffuse ring. The center spot is due to the direct transmission electron beam. These spots

are indexed in Figure 5-7. The distance ratio of $\frac{g_1}{g_2}$ is equal to the inverse d-spacing ratio of the (111) to (200) planes in the fcc lattice, corresponding to the diffraction pattern of fcc crystals in the [011] beam direction (Williams and Carter, *II: Diffraction*, 1996). These findings demonstrate that the nanocrystallites in the *a*-C matrix exhibit a diamond cubic structure and are oriented with their {111} planes parallel to the film surface.

The formation of crystalline nanodomains in the *a*-C films may be attributed to clusters of carbon atoms sputtered off from the target surface due to the intense Ar^+ bombardment and the subsequent epitaxial deposition of the clusters on the growing film surface. For a forward rf power greater than 400 W, the kinetic energy of Ar^+ bombarding on the target surface is greater than 1 keV (Table 5-1). Thus, the intensive bombarding process could sputter off from the target surface not only neutral carbon atoms but also clusters of carbon atoms. Deposition of these clusters on the film surface could then be accompanied by the epitaxial growth of nanocrystallites possessing continuous boundaries. This appears to be the formation mechanism of the plate-like nanocrystallites with {111} planes parallel to the film surface. The crystallite size is limited by both the size of carbon clusters and the deposition environment, which does not seem to favor epitaxial growth.

5.7 Summary

The cross-sectional microstructures of sputtered *a*-C films deposited on Si(100) substrates under various rf sputtering conditions are studied by both high-resolution TEM and AEM. Mass-thickness contrast in bright-field cross-sectional transmission electron

microscope images and qualitative EELS analysis reveal a two-layer structure consisting of a ~35 Å thick interfacial layer and the bulk of the *a*-C film. The thickness of the interfacial layer is found to be independent of the deposition conditions, suggesting that the substrate surface conditions control the nucleation and initial growth of the a-C films. Mass-thickness contrast in bright-field high-resolution transmission electron microscope images shows that the interfacial layer possesses a mass density greater than that of the *a*-C films. The interfacial layer, believed to consist of Si, *a*-C, and SiC, enhances the adhesion of the film to the substrate and relaxes the compressive residual stress in the film. Plate-like nanocrystallites (~35 Å in size) with {111} planes parallel to the film surface and randomly distributed in the sputtered *a*-C film are observed in high-resolution cross-sectional transmission electron microscope images. These nanocrystallites posses diamond cubic structures. The presence of these diamond nanocrystallites is attributed to carbon atom clusters sputtered off from the graphite target as a result of the intensive Ar^+ bombarding effect, followed by epitaxial growth upon cluster deposition on the growing film surface. The diamond nanocrystallite size is constrained by both the size of carbon clusters and the deposition conditions that are not conducive to epitaxial growth.

Table 5-1 Deposition conditions and film thickness of rf sputtered *a*-C films

Series	Forward rf power (W)	Absorbed rf power (W)	Substrate bias (V)	Target bias (V)	Deposition time (min)	Film thickness (nm)
I	200	172	-200	-499	3	5.6
	300	285	-200	-790	3	10.9
	400	388	-200	-1000	3	15.6
	500	500	-200	-1200	3	18.9
	600	600	-200	-1340	3	23.1
	750	739	-200	-1560	3	28.9
II	750	741.5	0	-1745	3	34.1
	750	746.5	-50	-1685	3	32.2
	750	747.5	-100	-1630	3	30.8
	750	744.5	-150	-1600	3	29.6
	750	715	-300	-1345	3	25.4
III	750	749	-200	-1535	5	46
	750	746	-200	-1533	7	67
	750	746	-200	-1550	9	85
	750	747	-200	-1550	11	100

Working pressure = 3 mTorr; Ar gas flow rate = 20 sccm

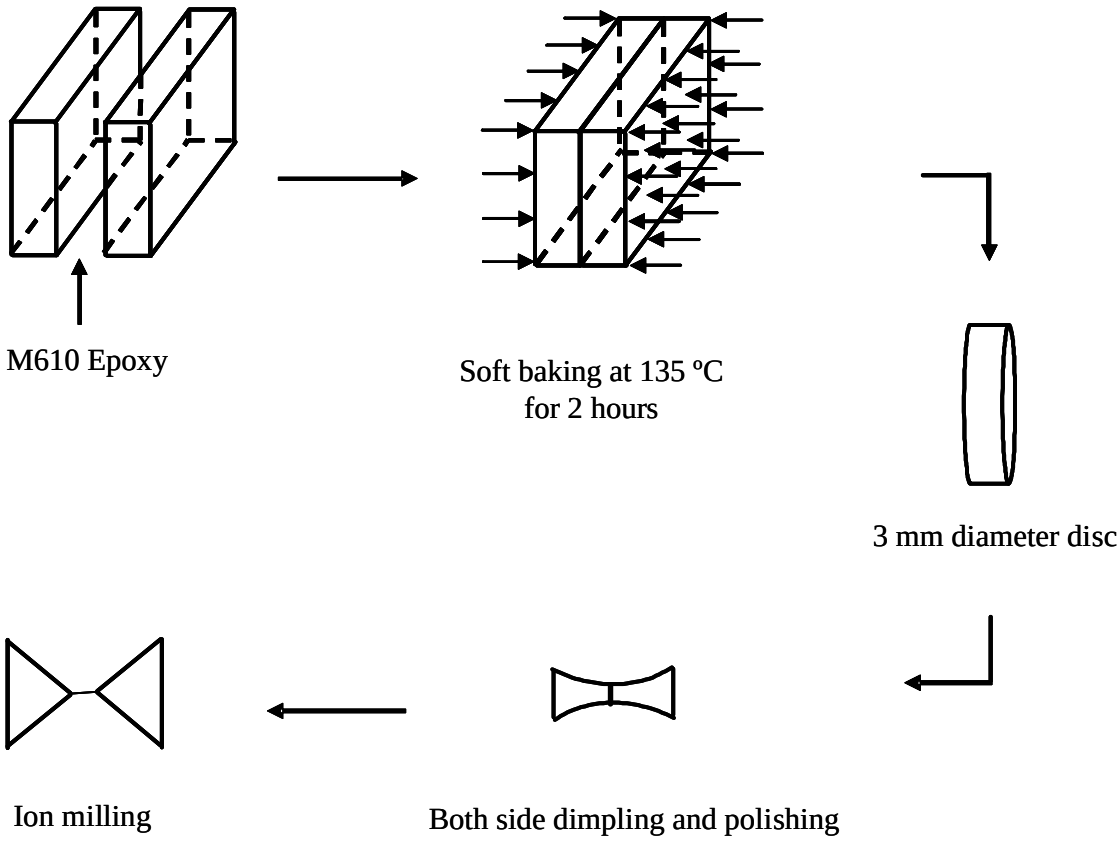

Figure 5-1 Schematic of sample preparation for high-resolution cross-sectional TEM analysis.

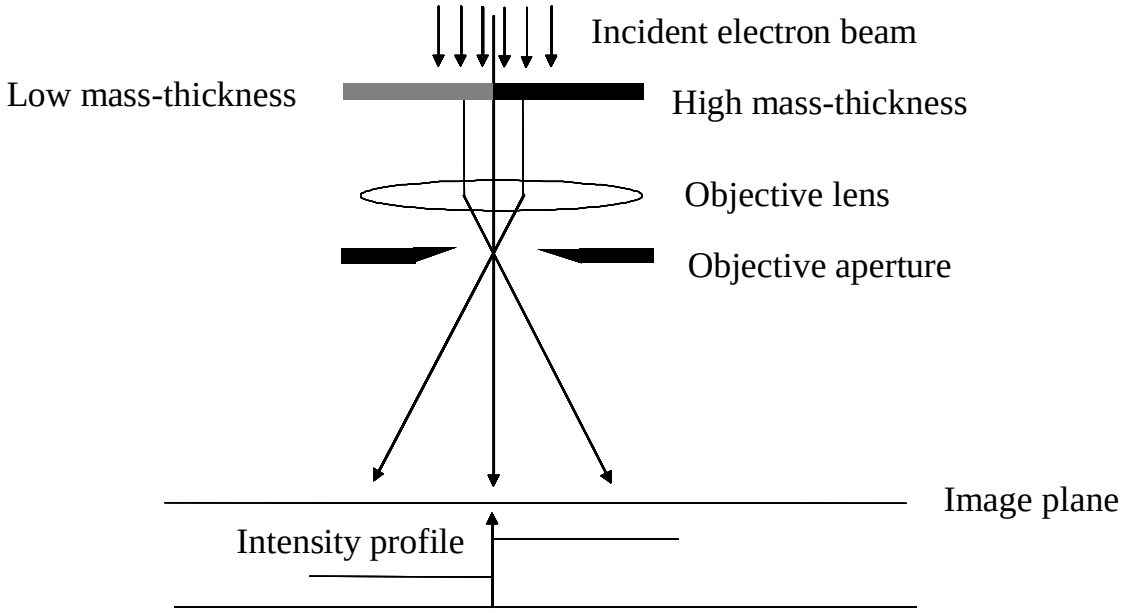

Figure 5-2 Schematic of mass-thickness effect on the contrast observed in bright-field transmission electron microscope imaging. (from Williams and Carter, *III: Imaging*, 1996, p. 353)

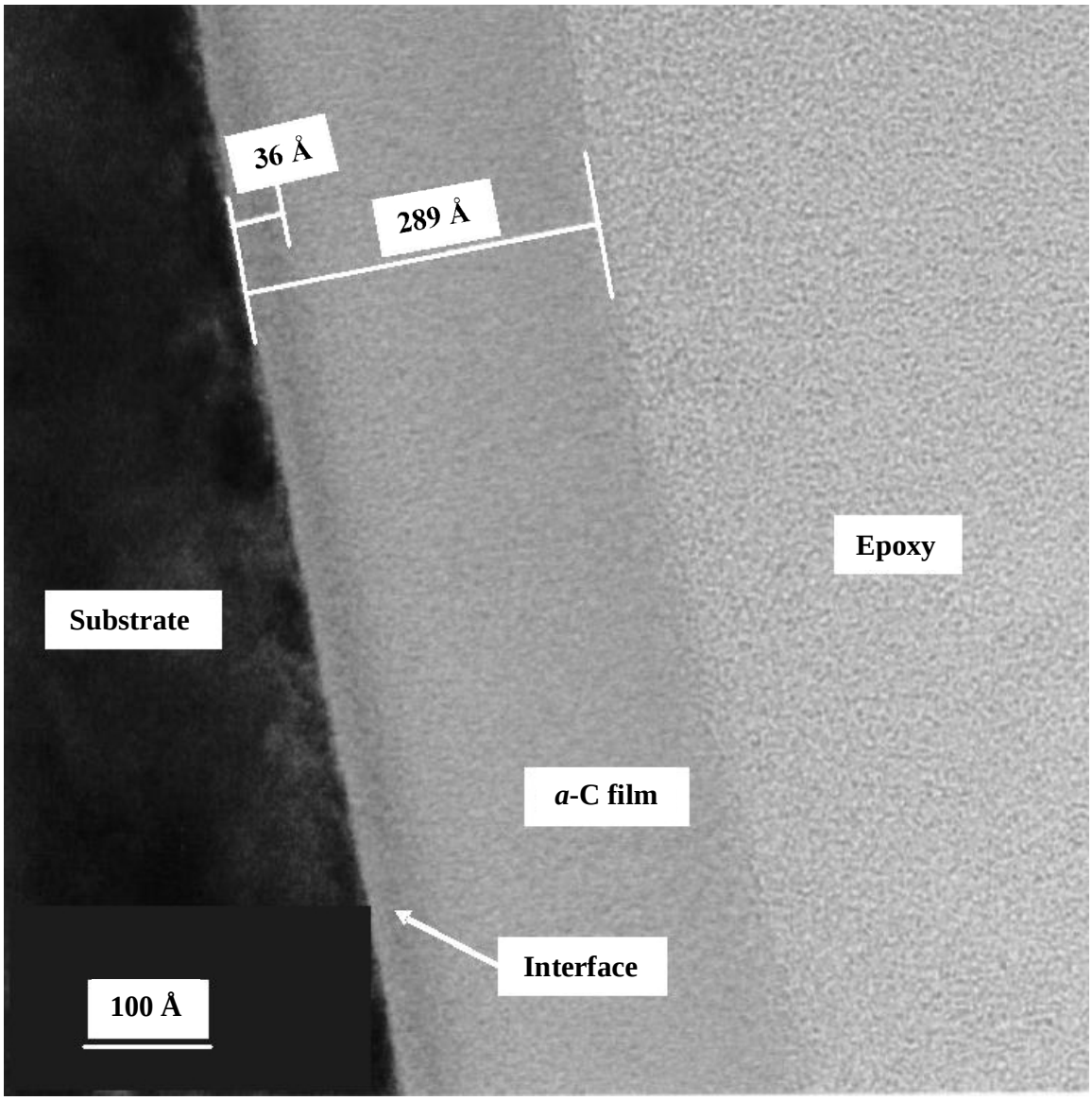

Figure 5-3 Cross-sectional transmission electron microscope image of sputtered *a*-C film deposited under conditions of 750 W forward rf power, -200 V substrate bias voltage, 20 sccm gas flow rate, 3 mTorr working pressure, and 3 minutes deposition time.

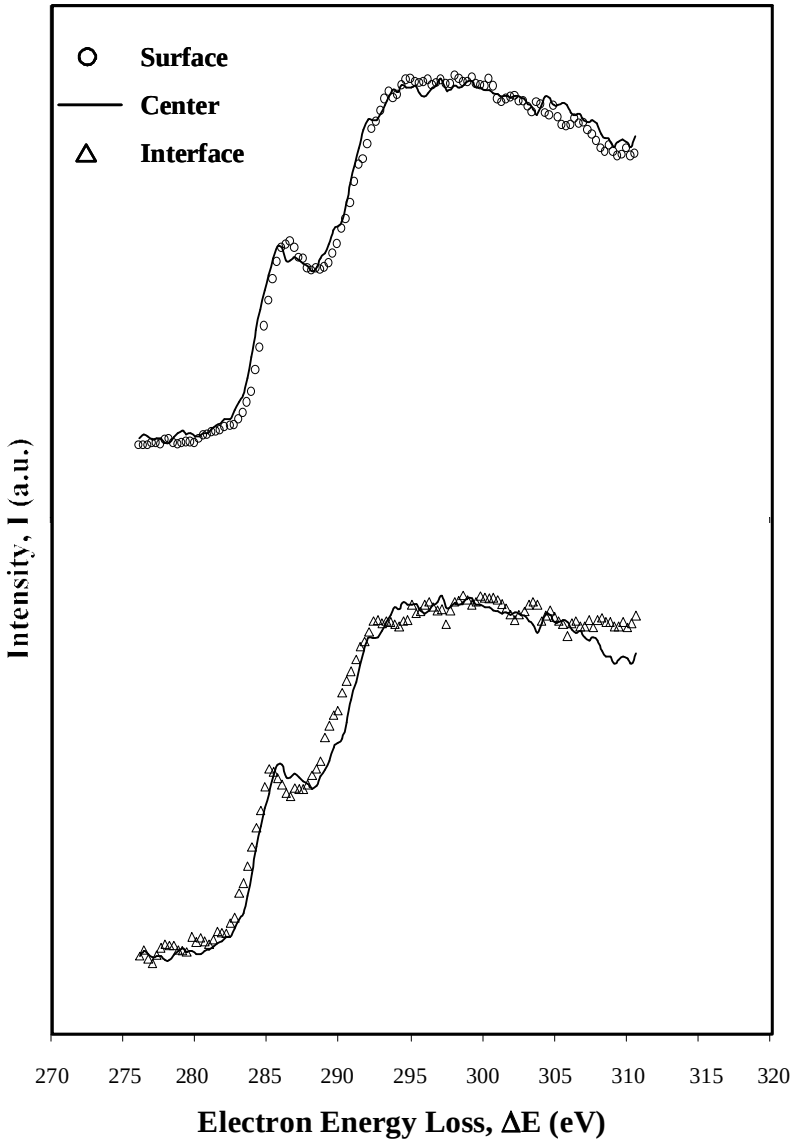

Figure 5-4 EELS spectra from the interfacial layer, the bulk of the film and near the film surface of *a*-C film deposited under conditions of 750 W forward rf power, -200 V substrate bias voltage, 20 sccm gas flow rate, 3 mTorr working pressure, and 3 minutes deposition time. The "center" spectrum is portrayed twice superimposed on the "surface" and "interface" data sets for comparison.

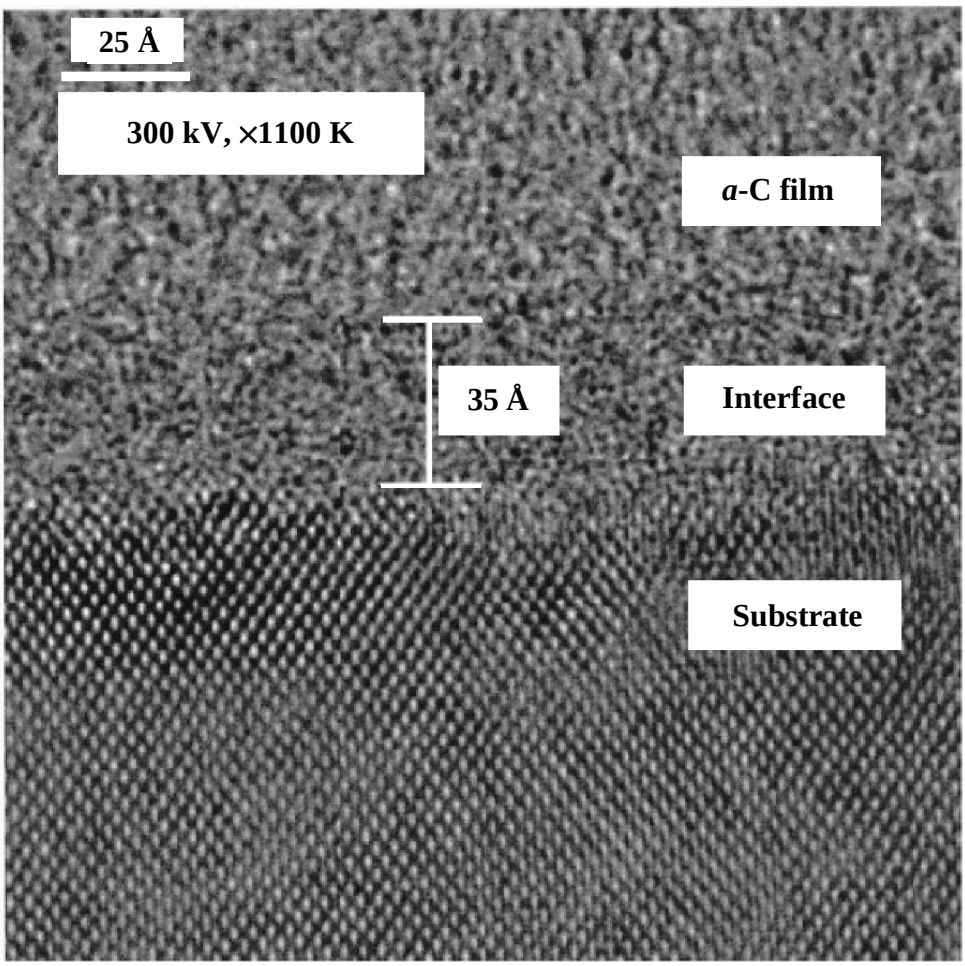

Figure 5-5 High-resolution transmission electron microscope image of the interfacial layer between the Si(100) substrate and an *a*-C film deposited under conditions of 750 W forward rf power, -200 V substrate bias voltage, 20 sccm gas flow rate, 3 mTorr working pressure, and 3 minutes deposition time.

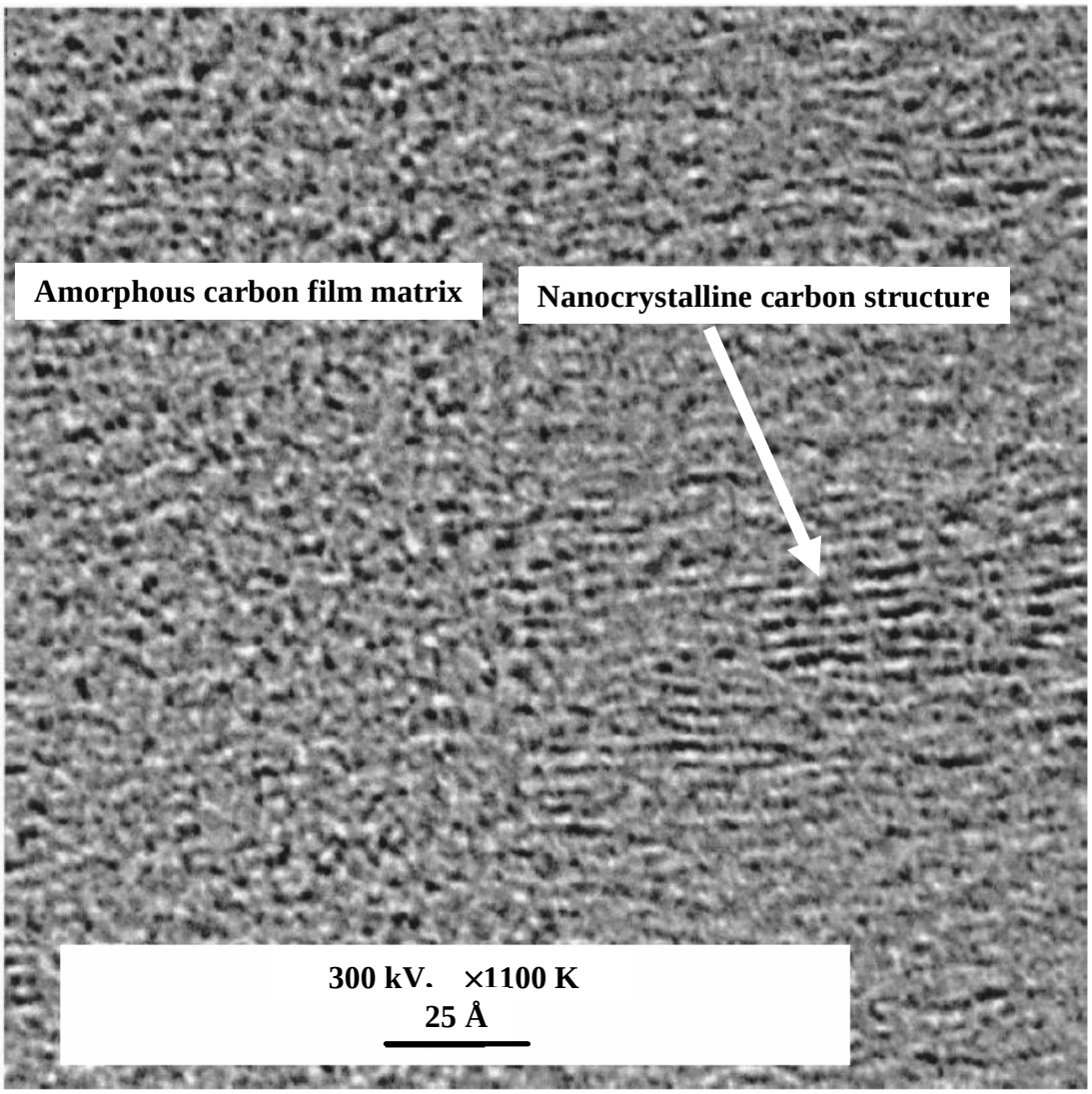

Figure 5-6 High-resolution cross-sectional transmission electron microscope image showing nanocrystallites in a sputtered *a*-C film deposited under conditions of 400 W forward rf power, -200 V substrate bias voltage, 20 sccm gas flow rate, 3 mTorr working pressure, and 3 minutes deposition time.

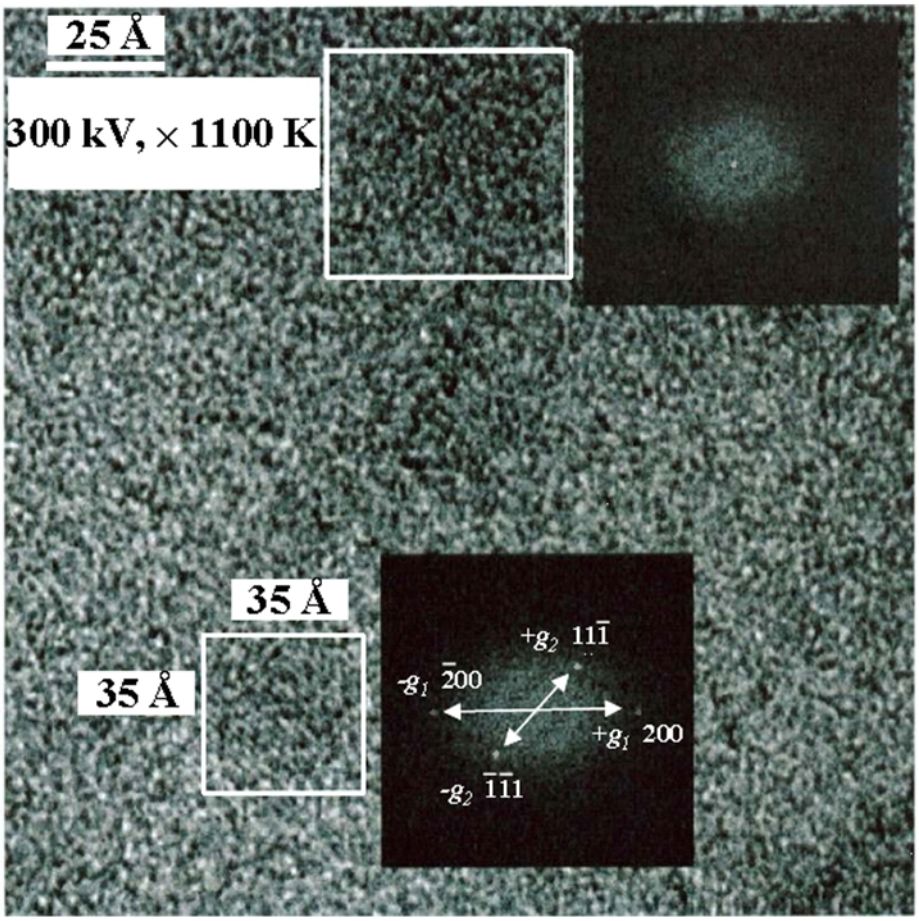

Figure 5-7 Calculated FFT patterns corresponding to nanocrystalline carbon and amorphous carbon regions in the sputtered *a*-C film shown in Figure 5-6. The distance ratio of g_1 / g_2 is equal to ~ 1.155, which corresponds to the diffraction pattern of fcc crystals in the [011] beam direction. This indicates that the nanocrystallites exhibit a diamond cubic structure and are oriented with their {111} planes parallel to the film surface.

CHAPTER 6

X-Ray Photoelectron Spectroscopy Studies of Sputtered *a*-C Films

6.1 Introduction

It is well known that the outermost *s* and *p* orbitals of carbon atoms are hybridized into sp^2 and sp^3 configurations to form π and σ bonds in *a*-C films, with only a small presence of sp^1 configurations (Comelli, et al., 1988; Robertson, 2002). In the sp^2 hybridization, three of a carbon atom's four valance electrons which enter trigonally directed sp^2 orbitals make σ bonds to neighbor atoms in a plane. The fourth lies in a π orbital normal to the σ bonding plane, and forms a weak π bond with a π orbital on one neighbor atom. In the sp^3 configuration, each of a carbon atom's four valence electrons which is assigned to a tetrahedrally directed sp^3 orbital form a strong σ bond with an adjacent atom. In the sp^1 configuration, two of a carbon atom's four valance electrons are assigned to σ orbitals, and each of them forms a σ bond along the $\pm$x directions, the rest enter π orbitals in the y and z directions. It is believed that the electronic properties of *a*-C films, such as their electrical conductivity and optical band gap, are governed by the π bonds because these bonds are weaker than σ bonds, while the mechanical and tribological properties, such as hardness and wear resistance, are determined by the strong σ bonds in the sp^3 carbon configurations (Robertson, 1986, 1992; Tsai and Bogy, 1987; Lu and Komvopoulos, 1999). Hence, systematic investigation of the effect of deposition conditions on the produced microstructures of *a*-C films synthesized by rf sputtering is desirable for understanding the mechanism of film growth and optimizing the film properties.

Several experimental techniques have been used to study the structure and composition of *a*-C films and related materials. X-ray photoelectron spectroscopy (XPS) is a powerful surface chemical composition analysis technique (Chang, 1981; Power and Seah, 1990). Usually, the information provided by XPS is contained in a spectrum that consists of a number of overlapping peaks with different peak shapes and intensities. These overlapping peaks reflect different chemical bond states. There are two main techniques used to resolve the spectrum into these components (Baruya and Maddams, 1978; Carley and Joyner, 1979; Maddams, 1980): deconvolution and curve fitting. The XPS data analysis techniques have been discussed by Proctor and Sherwood (1982) and reviewed by Sherwood (1983). In curve fitting it is assumed that a particular peak profile is uniquely characterized, and cannot be resolved into subcomponents once its full width at half maximum (FWHM) value has been fixed. Fortunately, numerical decomposition of the spectrum provided by XPS using Gaussian and Lorentzian profiles is unique, and curve fitting may be undertaken in most practical situations (Baruya and Maddams, 1978). Different types of carbon bonding can be discerned and studied quantitatively by decomposition of the C 1s XPS spectra using the curve fitting method proposed by Jackson and Nuzzo (1995) and Díaz et al. (1996). The C 1s core level obtained from an *a*-C film can be effectively decomposed into a number of Gaussian or Gaussian-Lorentzian profiles which reflect different types of carbon bonds. The Gaussian profile accounts for the instrumental energy resolution together with the chemical disorder, and the Lorentzian profile for the life time of the photoionization process (Díaz et al., 1996). From the best fit, the component surface concentration can be inferred by calculating the ratio of the area under the particular fitting curve to the total area under the spectrum.

In Chapter 5, TEM and EELS studies of sputtered *a*-C films were presented to illustrate that rf sputtered *a*-C films possess a two-layer structure consisting of a ~35-Å-thick interfacial layer and a continuous *a*-C film. Although XPS as a surface specific analysis technique can only probe the material composition a few nanometers below the surface, it is suitable to analyze the different types of carbon bonding in sputtered *a*-C films exhibiting two-layer structures. Four series of *a*-C films are sputtered under different conditions. The surface chemical compositions of these films are first detected by XPS surveys, and C 1s core level photoelectron spectra are subsequently obtained with XPS narrow scans. The microstructures of the *a*-C films are identified by decomposition of the C 1s XPS spectra using mixed Gaussian-Lorentzian profile curve fitting. The effect of plasma conditions on the microstructures of the *a*-C films is studied in light of XPS spectra and binding energy shift is interpreted in terms of the compressive residual stress in the films.

6.2 Experimental Procedures

Four series of *a*-C films are sputtered on Si(100) substrates. Films belonging in series I and II are synthesized under forward rf power ranging in the range of 300 - 750 W, with fixed substrate bias voltage of 0 or -200 V. In series III and IV, *a*-C films are deposited under substrate bias voltage between -50 and -200 V, and fixed forward rf power of 750 or 300 W. The working pressure, Ar gas flow rate, and deposition time are fixed at 3 mTorr, 20 sccm and 3 minutes, respectively, in all film depositions. Details about the *a*-C film deposition procedures have been given in section 3.2. The film deposition conditions, i.e., absorbed rf power P_a, target bias voltage V_T, and substrate

bias voltage V_S are given in Table 6-1 together with the Ar^+ ion impinging flux J_{Ar^+} and film thickness t_f. The Ar^+ impinging flux J_{Ar^+} is given by Eq. (3-1). In Chapter 3, it was reported that the film thickness depends linearly on the product of sputtering rate $\beta (= \gamma J_{Ar^+})$ and deposition time t. The film thickness given in Table 6-1 is calculated based on the film deposition conditions and the film thickness of a standard sample measured directly from high-resolution cross-sectional transmission electron microscope images. The standard sample is prepared under conditions of forward rf power of 750 W and substrate biased voltage of -200 V. The working pressure, gas flow rate, and deposition time are set at 3 mTorr, 20 sccm and 3 minutes, respectively. The deposition conditions of the standard sample, Ar^+ impinging flux, and film thickness are also given in Table 6-1.

X-ray photoelectron spectroscopy (XPS) spectra of rf sputtered *a*-C films are obtained with a PHI Model 5400 ESCA/XPS system. A 400 W Al$K\alpha$ (Energy: 1486.6 eV, Work function: 4.53 eV) anode x-ray source is used in the XPS studies. The Omni focus II lens is selected, and the aperture size is set at 3.3×1.1 mm. The XPS vacuum chamber pressure is maintained below 5×10^{-9} Torr. The *a*-C films are not sputtered by Ar^+ bombardment for cleaning before XPS measurement. All the *a*-C film surfaces are first surveyed in the binding energy range of 0 - 1300 eV using pass energy of 178.95 eV, channel width of 0.5 eV/step, and acquisition time of 50 ms/step. The final spectra are obtained after 10 sweeps. Next, multiplex narrow scan Si 2p3, Si 2s, Ar 2p1/2, Ar 2p3/2, C 1s, N 1s, and O 1s spectra are acquired using pass energy of 17.9 eV and channel width of 0.05 eV/step for C 1s, and 0.1 eV/step for all the other peaks, and acquisition time of

50 ms/step. The final C 1s core level spectra were obtained after 40 sweeps in the binding energy range of 280 - 295 eV.

6.3 Film Surface Composition Survey

For a homogeneous sample, the photoelectron emission intensity I of a specific element in the XPS survey spectrum is given by (Moulder, et al., 1995)

$$I = nS, \tag{6-1}$$

where n is the atomic number density of the specific element in the sample, and S is the atomic sensitivity factor. The relative concentration of the element x of interest in the sample is expressed as:

$$C_x = \frac{n_x}{\sum n_i} = \frac{I_x / S_x}{\sum I_i / S_i}. \tag{6-2}$$

The values of S are obtained for specific XPS system based on empirical peak area data.

Figure 6-1 shows an XPS survey spectrum of a thin *a*-C film. Five different chemical elements (C, Ar, Si, O, and N) are detected. Figure 6-2 shows an XPS multiplex narrow scan spectrum. After background subtraction using Shirley's method (1972), the C 1s, Ar 2p3/2, Si 2s, O 1s, and N 1s spectra obtained by XPS multiplex narrow scan on a specific *a*-C film surface are used to calculate each element's atomic concentration in this film, as listed in Table 6-2.

Ar atoms are incorporated in the *a*-C films by the implantation process. Hence, the Ar atomic concentration in the film is mainly determined by the Ar^+ ion kinetic energy, and is weakly affected by the Ar^+ ion impinging flux. Figures 6-3 and 6-4 show the effect of deposition conditions on the Ar concentration in the sputtered *a*-C films. It is obvious that the Ar atomic concentration is weakly dependent on the absorbed rf power and

strongly on the substrate bias voltage. O and N atoms are adsorbed at the film surface by both physisorption and chemisorption upon exposure to the ambient conditions and are not incorporated in the film. Both O and N atoms are absent during film growth because the deposition chamber is pumped down to a low base pressure (< $2x10^{-6}$ Torr) before the initiation of the film deposition. The XPS is performed in an ultra-high vacuum chamber (< 5×10^{-9} Torr). Most of the O and N atoms from the ambient adsorbed at the film surface are pumped out of the XPS chamber. The majority of the detected O and N atoms are those adsorbed by chemisorption. These atoms bind on C atoms chemically and affect the C 1s core level spectrum.

Phenomenologically, the adsorption can be described by an adsorption function $n = f(P,T)$, where n is the amount adsorbed, P is the pressure, and T is the temperature. At room temperature and low pressure, the amount adsorbed can be estimated by the Langmuir adsorption isothermal model (Adamson and Gast, 1997):

$$n = \frac{\kappa_2}{\kappa_1} n_m P , \tag{6-3}$$

where κ_1 and κ_2 are proportionality coefficients of evaporation and condensation, respectively, and n_m is the moles per gram adsorbed at the monolayer point given by

$$n_m = \frac{\Sigma}{N_0 \sigma^0} , \tag{6-4}$$

where Σ is the specific surface area of the solid, σ^0 is the area of an adsorbed site, and N_0 is Avogadro number. At a relatively high pressure in the valid pressure range of this model, n approaches the limiting value of n_m. Therefore, the amount absorbed is linearly proportional to the specific surface area, i.e., $n \propto \Sigma$.

Figure 6-5 shows that both O and N atomic concentrations are strongly dependent on the implanted Ar atomic concentration. The higher the Ar atomic concentration in the *a*-C film, the lower the O and N atomic concentrations. As mentioned previously, the Ar atomic concentration is mainly determined by the Ar^+ kinetic energy. Ar^+ bombardment on the growing *a*-C film surface significantly improves the surface roughness with increasing kinetic energy up to ~200 eV (section 3.5). For 750 W forward rf power, the surface rms roughness of sputtered *a*-C film decreases from 1.13 nm to 0.12 nm when the substrate bias voltage changes from 0 to -200 V (Figure 3-7). A higher Ar atomic concentration in sputtered *a*-C films suggests a stronger Ar^+ bombardment effect and a smoother *a*-C film surface. The smoother the film surface, the smaller the specific surface area, resulting in less O and N adsorb at the film surface.

6.4 Decomposition of C 1s Core Level XPS Spectra

As mentioned previously, the C 1s XPS spectra obtained from *a*-C film surfaces can be effectively decomposed into a number of Gaussian or Gaussian-Lorentzian profiles corresponding to different types of carbon bonds, and the decomposition is unique in practical situations. In this work, mixed Gaussian-Lorentzian (GL) profiles are used to fit the C 1s XPS spectra by a standard least squares algorithm after subtracting the background noise according to Shirley's method. The FWHM values of all the peaks are set in the range of 0 - 3 eV during curve fitting.

Díaz et al. (1996) reported that the line positions of the sp^2 and sp^3 hybrids are at 284.3 and 285.2 eV, respectively, in the C 1s spectra of *a*-C films deposited by pulsed laser evaporation of graphite targets, and that the binding energy of sp^3 hybrids is upward

shifted by 0.9 eV from that of sp^2 hybridized carbon. Jackson and Nuzzo (1995) reported that binding energies of 284.84 and 285.80 eV correspond to sp^2 and sp^3 bonded carbons, respectively, in *a*-C films deposited by dc magnetron sputtering and cathodic arc deposition. Taki and Takai (1998) observed sharp peaks at 284.15 and 285.50 eV in the spectra of graphite and diamond, respectively, and assigned these values to the binding energies of sp^2 and sp^3 bonded carbon in *a*-C:H films synthesized by shielded arc ion plating. They also reported that the corresponding FWHM values are 1.0 and 2.20 eV. Mérel et al. (1998) found that the binding energies of sp^2 and sp^3 hybridized carbon atoms in pulsed laser deposited *a*-C films are equal to 284.4 and 285.2 eV, respectively, and the corresponding FWHM values are equal to 1.0 and 1.10 eV. Tay et al. (1999) found that the line positions of sp^2 and sp^3 bindings in *a*-C films deposited by the filtered cathodic vacuum arc deposition are at 284.3 and 285.1 eV, respectively. Lu and Komvopoulos (1999, 2001) reported that the binding energies of sp^2 and sp^3 hybridized carbon atoms in *a*-C films deposited by rf sputtering are in the ranges of 284.24-284.45 and 285.36-285.44 eV, respectively, depending on the deposition conditions.

In view of the above investigations, the search of sp^2 and sp^3 binding peak positions is performed in the ranges of 283.95-284.55 and 284.95-285.70 eV, respectively, while the sp^1 binding peak position is searched in the range of 282-283.5 eV. As discussed previously, the shape of the C 1s core level XPS spectrum can be modified due to chemical adsorption of O and N atoms. Since the N atomic concentration is less than 3 at.% in all the *a*-C films, the effect of the N atoms can be neglected. However, the O atomic concentration is greater than 6 at.% and, therefore, must be considered in the fitting of the C 1s XPS spectra. To account for the presence of O, three additional peaks

are searched in the ranges of 286-287, 287-288.5, and 288.5-290.5 eV, respectively (Lu and Komvopoulos, 2001). Finally, six GL profiles are used to fit the C 1s core level XPS spectra. Figure 6-6 shows a representative C 1s core level XPS spectrum of a sputtered *a*-C film with six mixed GL profile fits.

6.5 Effects of Deposition Conditions on Microstructure of Sputtered *a*-C Films

As mentioned previously, it is desirable to study the effects of deposition conditions on the ratio of $sp^3/(sp^2+sp^3)$ because the mechanical and tribological properties of *a*-C films are controlled by the strong σ bonds in the sp^3 configurations. Figures 6-7 and 6-8 show the effect of deposition conditions on the $sp^3/(sp^2+sp^3)$ ratio of rf sputtered *a*-C films. The $sp^3/(sp^2+sp^3)$ ratio of the *a*-C films in Series I is nearly constant (i.e., ~27%) and independent of the rf power. However, the $sp^3/(sp^2+sp^3)$ ratio of the *a*-C films in Series II increases linearly from 30.41% to 48.62% with the increase of the rf power from 300 W to 750 W (Figure 6-7). The $sp^3/(sp^2+sp^3)$ ratio of the *a*-C films in both Series III and IV increase from 26.8% to 48.62% and 26.68% to 30.41%, respectively, when the substrate bias voltage is changed from 0 to -200 V (Figure 6-8).

The percentage of sp^3 hybridized carbon atoms in rf sputtered *a*-C film is governed by thermodynamic principles and is strongly affected by the Ar^+ bombardment on the growing film surface. Before *a*-C film deposition, a fresh Si(100) substrate surface is produced by Ar^+ sputter etching to remove the native oxide layer. After the formation of an ultrathin interfacial layer on the freshly exposed silicon substrate, the neutral carbon atoms arriving from the pure graphite target bind to each other to spontaneously form a

stable continuous film to minimize the surface free energy, which can be described as a thermodynamic process. The percentage of sp^3 hybridized carbon atoms is affected only by the film surface condition, and the $sp^3/(sp^2+sp^3)$ ratio is independent of the rf power, in the absence of Ar^+ bombardment on the growing film surface, as shown in Figure 6-7.

However, intense Ar^+ bombardment during film growth enhances the formation of sp^3 bindings in *a*-C film. The Ar^+ impinging flux increases from 5.4×10^{15} to 8.2×10^{15} ions/cm^2·s with the increase of the absorbed rf power from 282.5 to 752 W as shown in Table 6-1 (Series II). This enhances the Ar^+ bombardment effect, which is beneficial to the formation of sp^3 bindings in the film. This is shown in Figure 6-7 for the *a*-C films of Series II. Hence, It may be inferred that Ar^+ bombardment produces an enhancement of the sp^3 bonding content in the *a*-C films.

The $sp^3/(sp^2+sp^3)$ ratio of the *a*-C films in both Series III and IV increases with the increase of the Ar^+ kinetic energy from ~10 to ~210 eV (Figure 6-8) for fixed Ar^+ impinging fluxes. The Ar^+ impinging flux (~5.3×10^{15} ions/cm^2·s) for rf power equal to 300 W is less than that for 750 W rf power (~8.3×10^{15} ions/cm^2·s) (i.e., samples A and K in Table 6-1). Therefore, the Ar^+ bombardment effect is weaker during the growth of the *a*-C films of Series IV than that during the growth of the *a*-C films of Series III, and the $sp^3/(sp^2+sp^3)$ ratio of the *a*-C films of Series IV is smaller than that of the *a*-C films of Series III (Figure 6-8). The underlying mechanism of the enhanced sp^3 hybridization in sputtered *a*-C films is discussed in detail in Chapter 7.

6.6 Binding Energy Shift

Figure 6-9 shows the effect of forward rf power on the binding energy of peaks 1 (sp^1), 2 (sp^2), and 3 (sp^3). The binding energy of peak 1 (sp^1) in the *a*-C films of Series I (no Ar^+ bombardment) and Series II (intensive Ar^+ bombardment) increases from 282.59 to 283.27 eV and 282.67 to 282.96 eV, respectively, with the increase of the forward rf power from 300 to 750 W. There are no obvious differences between the binding energies of peak 1 (sp^1) in both series of *a*-C films. However, the binding energy of peak 2 (sp^2) decreases from 284.48 to 284.33 eV and 284.23 to 284.06 eV, respectively, in the *a*-C films of both Series I and II with forward rf power increasing from 300 to 750 W, and the binding energy of peak 3 (sp^3) decreases from 285.62 to 285.44 eV and 285.37 to 284.95 eV, respectively. Figure 6-9 shows that both binding energies of peaks 2 (sp^2) and 3 (sp^3) have shifter to lower energy levels as a consequence of the intense Ar^+ bombardment during film growth.

Figure 6-10 shows the effect of the Ar^+ kinetic energy (substrate bias effect) on the binding energy of peaks 1 (sp^1), 2 (sp^2), and 3 (sp^3). The binding energy of peak 1 (sp^1) in the *a*-C films of Series III (forward rf power equal to 750 W) increases from 283.27 to 283.45 eV as the substrate bias changes from 0 to -50 V, and then decreases to 282.61 eV with substrate biased changing from -50 to -150 V. Finally, the binding energy of peak 1 (sp^1) in the *a*-C films of Series III increases again to 282.96 eV as the substrate bias voltage changes from -150 to -200 V. The binding energy of peak 1 (sp^1) in the *a*-C films of Series IV (forward rf power equal to 300 W) remains nearly constant (~282.6 eV), demonstrating insensitivity to the change of the substrate bias voltage. The binding energy of peak 2 (sp^2) in the *a*-C films of both Series III and IV decreases from 284.33 to

284.06 eV and 284.48 to 284.23 eV, respectively, as the substrate bias voltage changes from 0 to -200 V. The binding energy of peak 3 (sp^3) in the *a*-C films of both Series III and IV decreases from 285.44 to 284.95 eV and 285.62 to 285.37 eV, respectively, with substrate bias changing from 0 to -200 V. Again, the binding energies of both peaks 2 (sp^2) and 3 (sp^3) are shifted to lower energy levels as the effect of the Ar^+ bombardment is enhanced by substrate biasing (Figure 6-10).

The binding energy of the XPS photoelectron peak is conveniently referred to the Fermi level. Figure 6-11 shows an energy level diagram for a non-conducting sample in contact with an electron spectrometer in electrical equilibrium (Evans, 1977). The binding energy (BE^F) can generally be obtained directly from the instrumental kinetic energy (KE^m) scale using the usual relationship (Siegbahn, 1967)

$$h\nu = KE^m + BE^F + \phi_{sp}, \tag{6-5}$$

where $h\nu$ is the X-ray photon energy ϕ_{sp} and is the spectrometer work function. There are several major factors contributing to the shift of the XPS electron binding energies of an atom in a solid, such as the differences in valence electron density, field potential, work function and relaxation (Siegbahn, 1967). Generally, the binding energy shift can be expressed as follows (Kim and Winograd, 1975)

$$\Delta BE^F = \frac{\Delta q}{r} - \Delta V^f - \Delta E_R - \Delta\phi, \tag{6-6}$$

where the $\Delta q / r$ represents the so called "chemical shift" due to differences in valence electron density or in the oxidation state of the common ion, ΔV^f is the difference in field potential energy, ΔE_R represents relaxation effects, which can be neglected, and

$\Delta\phi$ is the work function correction. If the binding energy is obtained from Eq. (6-5), then $\Delta\phi = 0$, and Eq. (6-6) can be simplified as follows

$$\Delta BE^F = \frac{\Delta q}{r} - \Delta V^f . \tag{6-7}$$

Eq. (6-7) is the famous charge potential model for the shift in binding energy introduced by Siegbahn, et al. (1969). For the same kind of chemical bonds between the same atoms, such as sp^3 hybridized bonds between carbon atoms in *a*-C films, Eq. (6-7) can be further simplified as

$$\Delta BE^F = -\Delta V^f . \tag{6-8}$$

For an atom A in a solid, the field potential energy V_A^f is given by a simple point-charge approximation

$$V_A^f = \sum_{B \neq A} \frac{q_B}{4\pi\varepsilon_o r_{AB}}, \tag{6-9}$$

where q_B is the charge on the atom B, r_{AB} is the internuclear distance between the atom A and B, and ε_o is the permittivity of the free space. In the presence of a large compressive stress in a solid, the internuclear distance between atoms in the solid is reduced. According to Eq. (6-9), the field potential in the solid will increase, and the difference in the potential energy between the stressed solid and stress-free solid, ΔV^f, will be positive. Hence, the binding energy position of the XPS photoelectron peak in a stressed solid will shift to a lower energy level from the binding energy position of the XPS photoelectron peak in the stress-free solid according to Eq. (6-8).

As discussed in Chapter 4, a relatively high in-plane, equibiaxial, compressive residual stress arises in rf sputtered *a*-C films synthesized under intense Ar^+

bombardment. The magnitude of the residual stress depends on the Ar^+ kinetic energy and the impinging flux. Thus, the stronger the Ar^+ bombardment, the higher the compressive residual stress. While there is no Ar^+ bombardment during the growth of the *a*-C films in Series I, intense Ar^+ bombardment is applied during the growth of the *a*-C films in Series II. Therefore, the residual stress in the films of Series II is higher than that in Series I. This produces a shift in the carbon binding energy positions of both peaks 2 (sp^2) and 3 (sp^3) in the XPS spectra of the films in Series II to lower energy compared to the films in Series I (Figure 6-9). The Ar^+ impinging flux (~8.3×10^{15} ions/cm^2·s) during deposition of the *a*-C films in Series III (forward rf power equal to 750 W) is larger than that (~5.3×10^{15} ions/cm^2·s) during deposition of the *a*-C films in Series IV (forward rf power equal to 300 W) (Table 6-1). Hence, the Ar^+ bombardment effect during the growth of the *a*-C films in Series III is more pronounced than that during the growth of the *a*-C films in Series IV. This explains the higher compressive residual stress in the *a*-C films of Series III and the shift of the carbon binding energy positions of both peaks 2 (sp^2) and 3 (sp^3) to lower energy levels compared to the films of Series IV (Figure 6-10).

6.7 Summary

X-ray photoelectron spectroscopy **(**XPS) is used to study the structure of rf sputtered *a*-C films synthesized under different conditions. Five different chemical elements, i.e., C, Ar, Si, O, and N, are detected on the *a*-C film surfaces by XPS surveys. Ar atoms are incorporated into the films by the implantation process, and the Ar atomic concentration in the films is mainly determined by the Ar^+ kinetic energy and secondarily by the Ar^+ impinging flux. O and N atoms are adsorbed at the *a*-C film surfaces by

physisorption and chemisorption, and their atomic concentrations are significantly affected by the surface roughness. The microstructures of the sputtered *a*-C films are studied by the decomposition of corresponding C 1s XPS spectra using mixed Gaussian-Lorentzian profile curve fitting technique. The percentage of sp^3 hybridized C atoms in rf sputtered *a*-C films is described by thermodynamics and is shown to be significantly affected by the Ar^+ bombardment during film growth. Ar^+ bombardment enhances the formation of sp^3 hybridization and causes a shift in binding energy positions for both sp^2 and sp^3 hybridized C atoms, which is related to the relatively high compressive residual stress in the films.

Table 6-1 Deposition conditions, Ar^+ impinging flux and film thickness

Series	Sample	Absorbed rf Power (W)	Target bias (V)	Substrate bias (V)	Ar^+ flux ($\times 10^{15}$ ions/cm^2·s)	Thickness (nm)
I	A	298.5	-1095	0	5.15	14.6
	B	401.0	-1290	0	5.89	19.1
	C	496.5	-1400	0	6.73	23.2
	D	595.0	-1550	0	7.29	27.1
	E	746.5	-1750	0	8.12	32.8
II	F	282.5	-780	-200	5.44	10.3
	G	393.5	-995	-200	6.23	15.3
	H	495.5	-1195	-200	6.74	19.6
	I	597.0	-1340	-200	7.37	23.5
	J	752.0	-1550	-200	8.18	29.2
III	K	749.5	-1667	-50	8.31	32.5
	L	751.5	-1630	-100	8.27	31.9
	M	754.0	-1600	-150	8.20	30.9
IV	N	298.5	-100	-50	5.37	14
	O	299.0	-965	-100	5.30	13.4
	P	293.0	-880	-150	5.37	12.2
Standard sample		739.0	-1560	-200	7.99	28.7*

*: The film thickness of the standard sample is measured directly from a high-resolution cross-sectional transmission electron microscope image.

Table 6-2 Elemental concentrations in *a*-C film surfaces

Series	Sample	Elemental concentration (at.%)				
		C	Ar	Si	O	N
I	A	77.8	0.5	4.8	14.3	2.8
	B	82.6	0.4	1.7	13.6	1.8
	C	83.4	0.1	1.0	14.3	1.1
	D	83.9	0.1	0.3	14.0	1.7
	E	85.5	0.0	1.2	11.9	1.1
II	F	85.6	1.9	3.4	8.1	0.9
	G	90.5	2.0	0.2	6.6	0.6
	H	90.4	1.6	0.4	7.2	0.4
	I	91.9	1.6	0.1	6.0	0.4
	J	89.8	1.4	0.7	7.7	0.3
III	K	82.6	2.0	1.5	12.8	1.1
	L	91.9	1.6	0.2	6.0	0.4
	M	91.8	1.4	0.0	6.3	0.6
IV	N	87.2	2.2	1.4	8.3	0.8
	O	85.4	1.7	2.7	9.8	0.3
	P	88.4	2.0	1.8	7.5	0.3

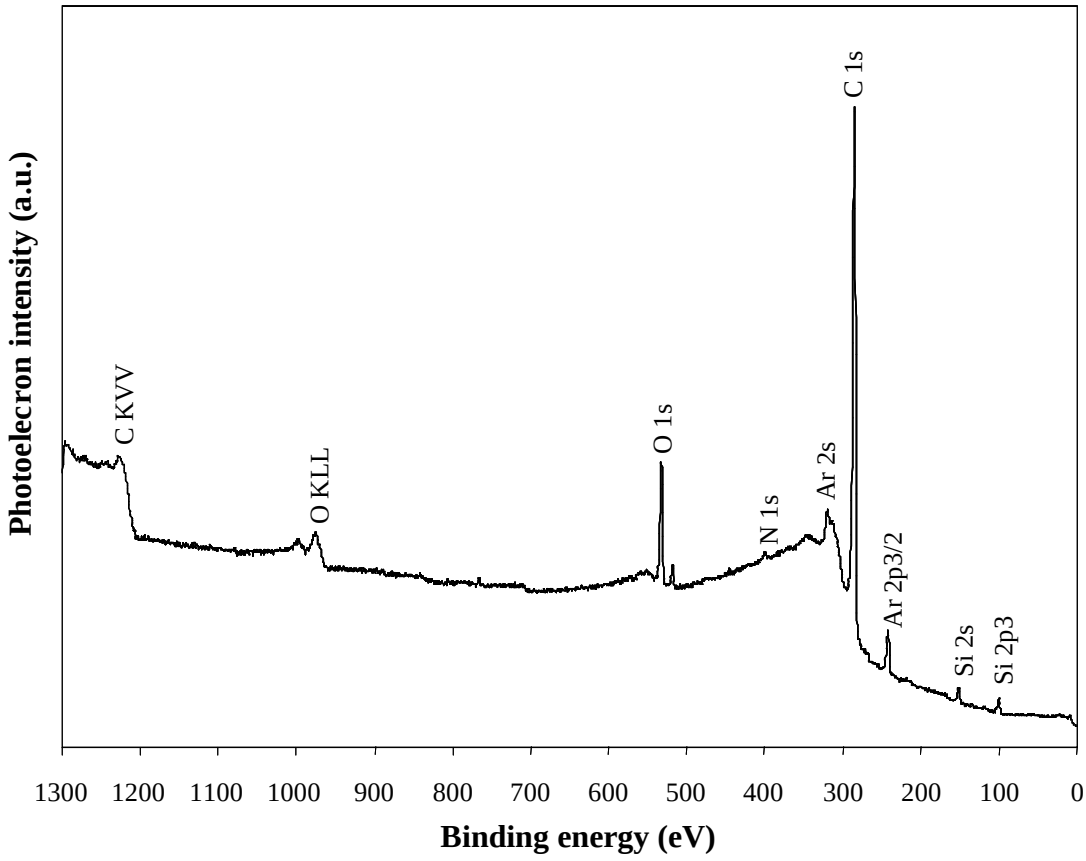

Figure 6-1 XPS survey spectrum of rf sputtered *a*-C film synthesized under conditions of 300 W forward rf power, -200 V substrate bias voltage, 20 sccm gas flow rate, and 3 minutes deposition time.

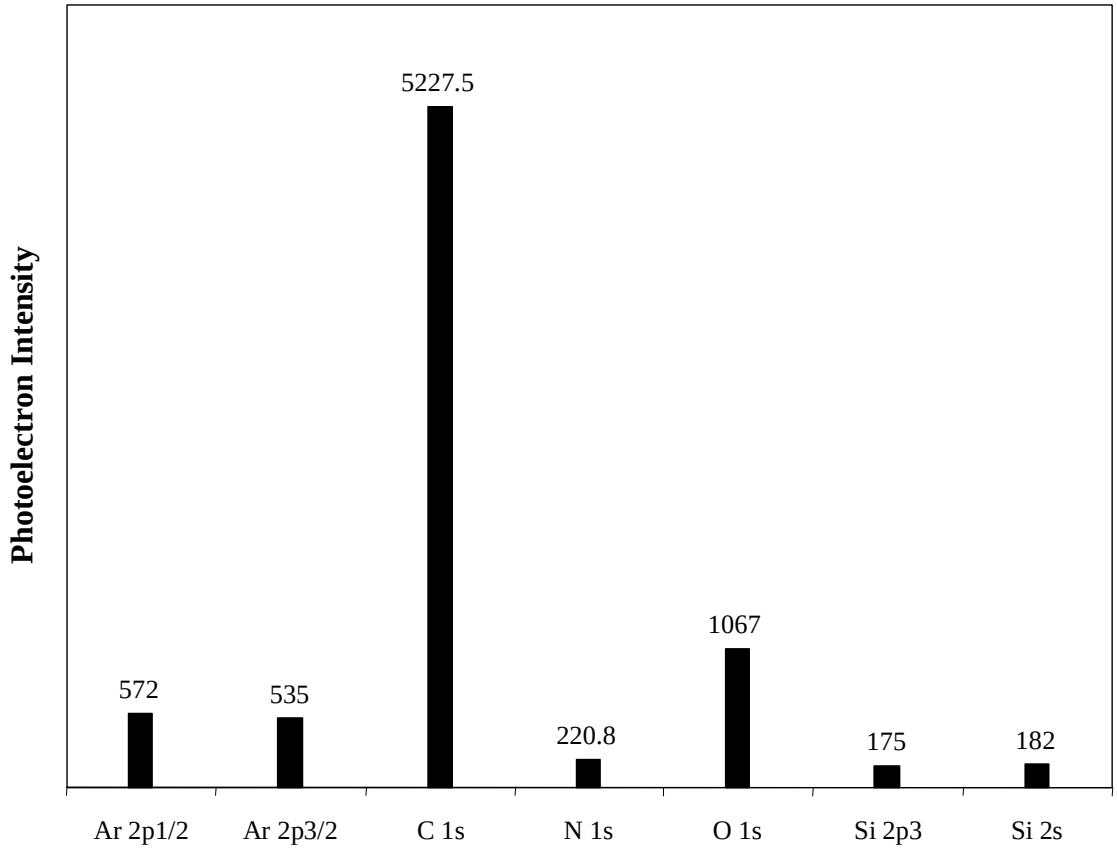

Figure 6-2 XPS multiplex narrow scan spectrum of *a*-C film surveyed by XPS in Figure 6-1.

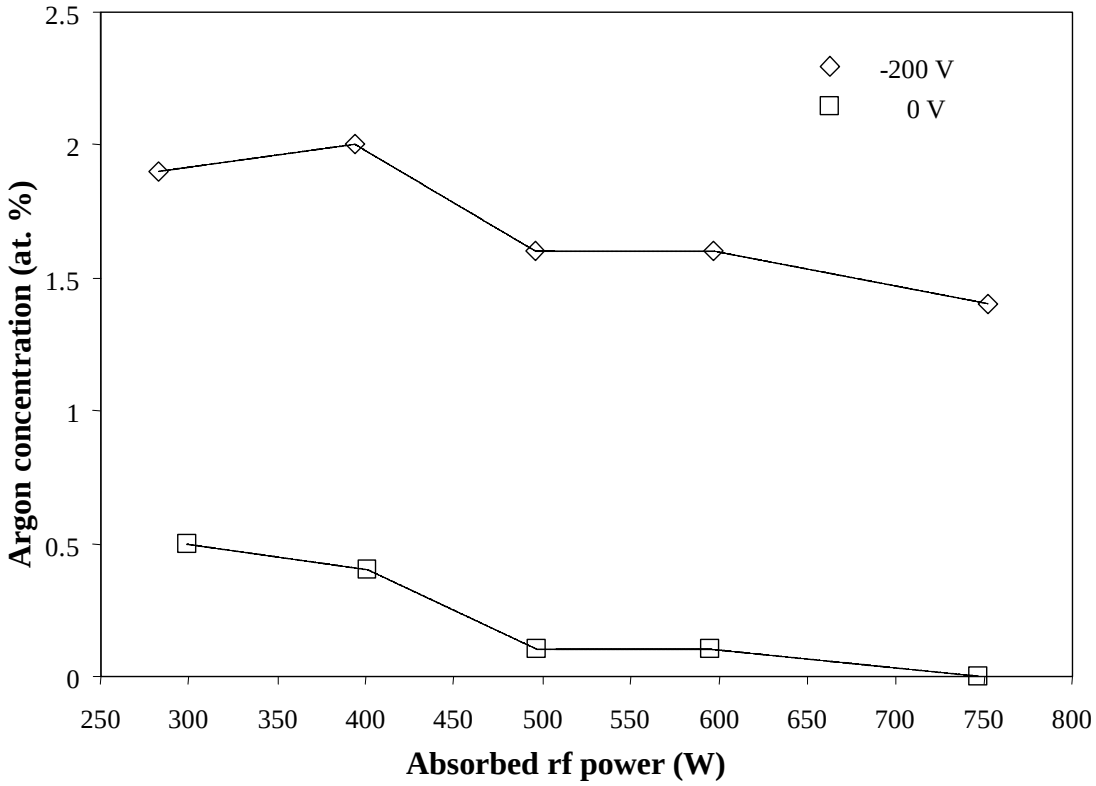

Figure 6-3 Effect of absorbed rf power on Ar atomic concentration in sputtered *a*-C films for 0 and -200 V substrate bias.

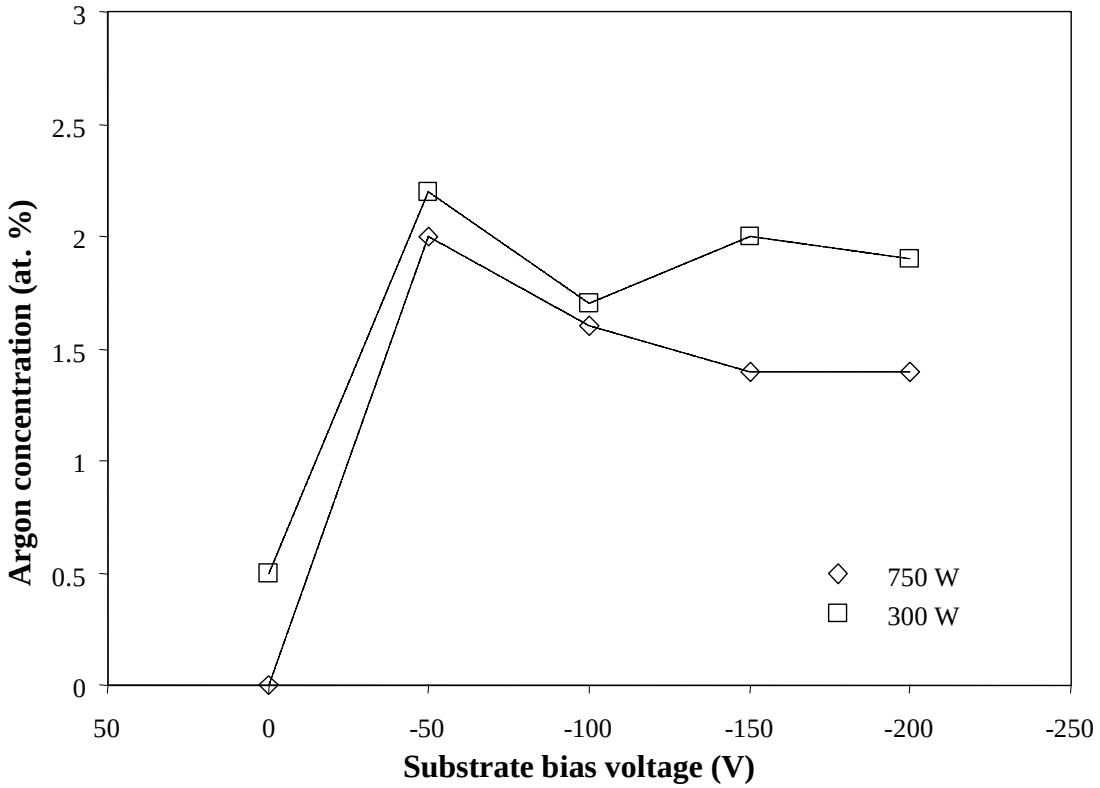

Figure 6-4 Effect of substrate bias on Ar atomic concentration in sputtered *a*-C films for forward rf power of 300 and 750 W.

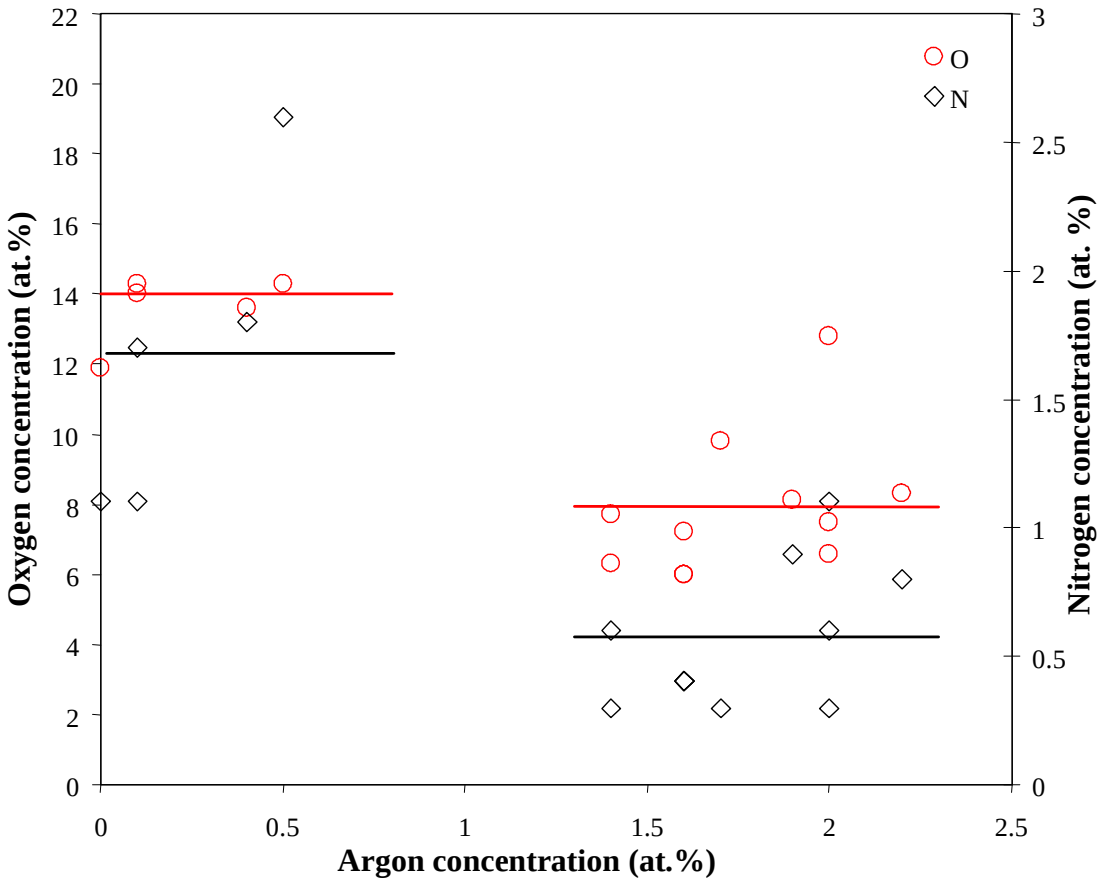

Figure 6-5 Implanted Ar atom dependence of both the O and N atomic concentrations in sputtered *a*-C films. Open symbols show actual data points; lines show trends.

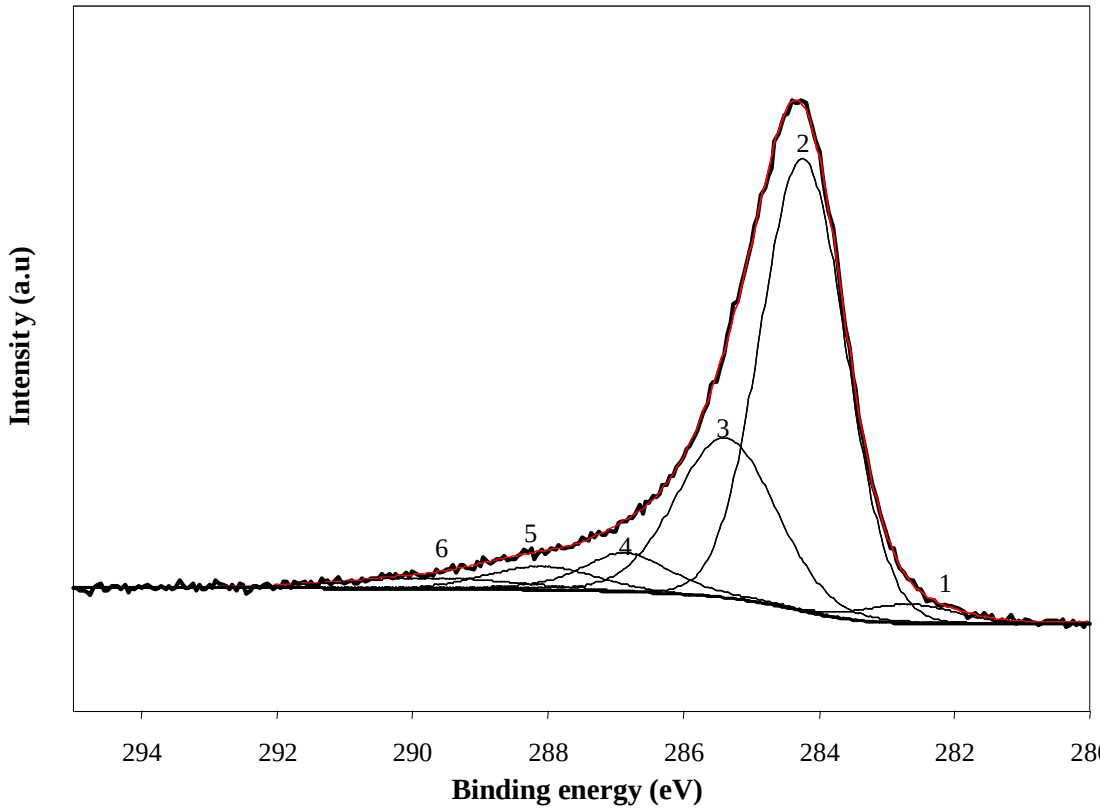

Figure 6-6 Typical C 1s core level XPS spectrum of sputtered *a*-C film deposited under conditions of forward rf power of 300 W, substrate bias voltage of -200 V, 20 sccm gas flow rate, and 3 minutes deposition time with six Gaussian–Lorentzian profile fits.

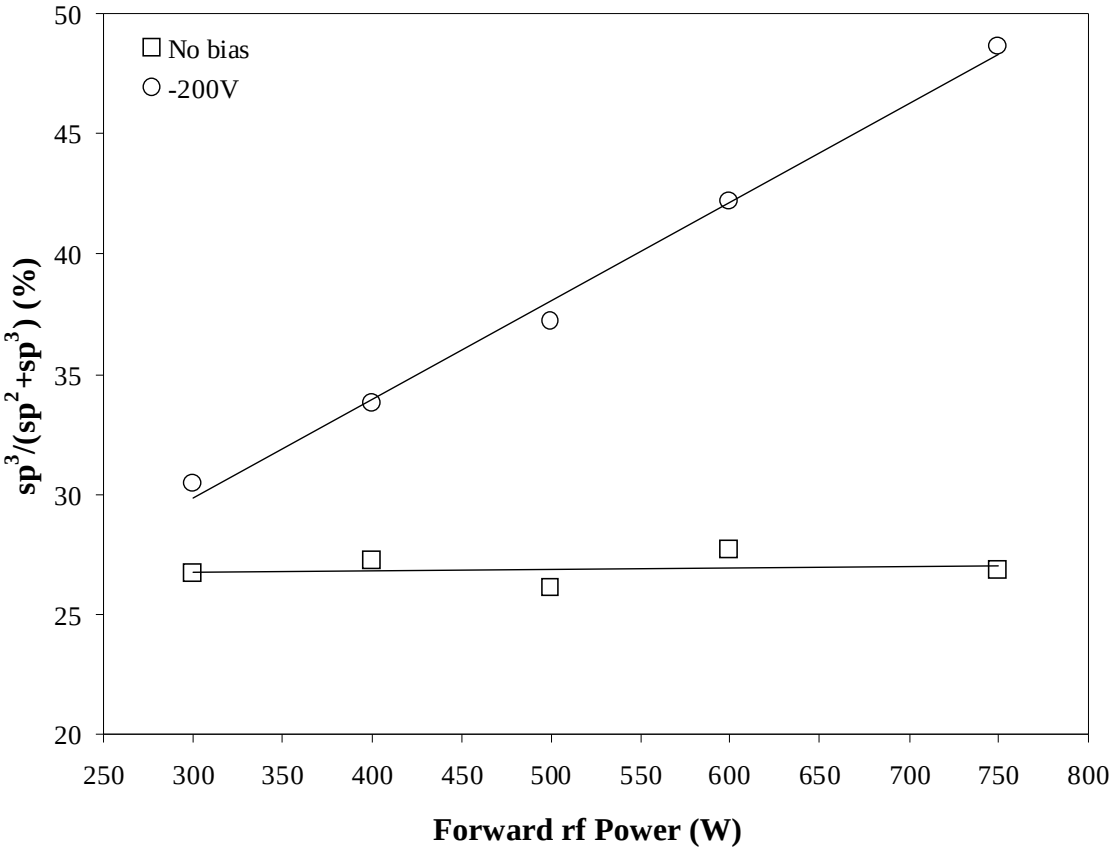

Figure 6-7 Effect of rf power on sp^3 content in sputtered *a*-C films for 0 and -200 V substrate bias.

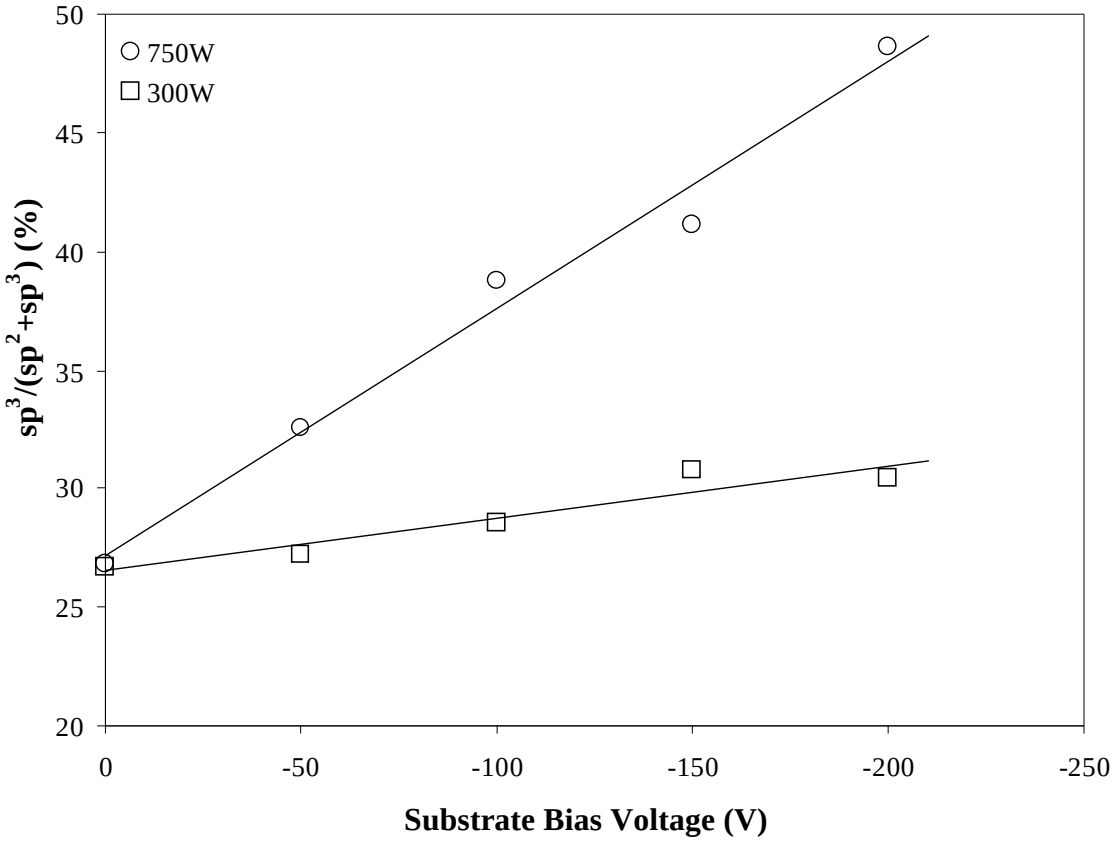

Figure 6-8 Effect of substrate bias on sp^3 content in sputtered *a*-C films for 300 and 750 W rf power.

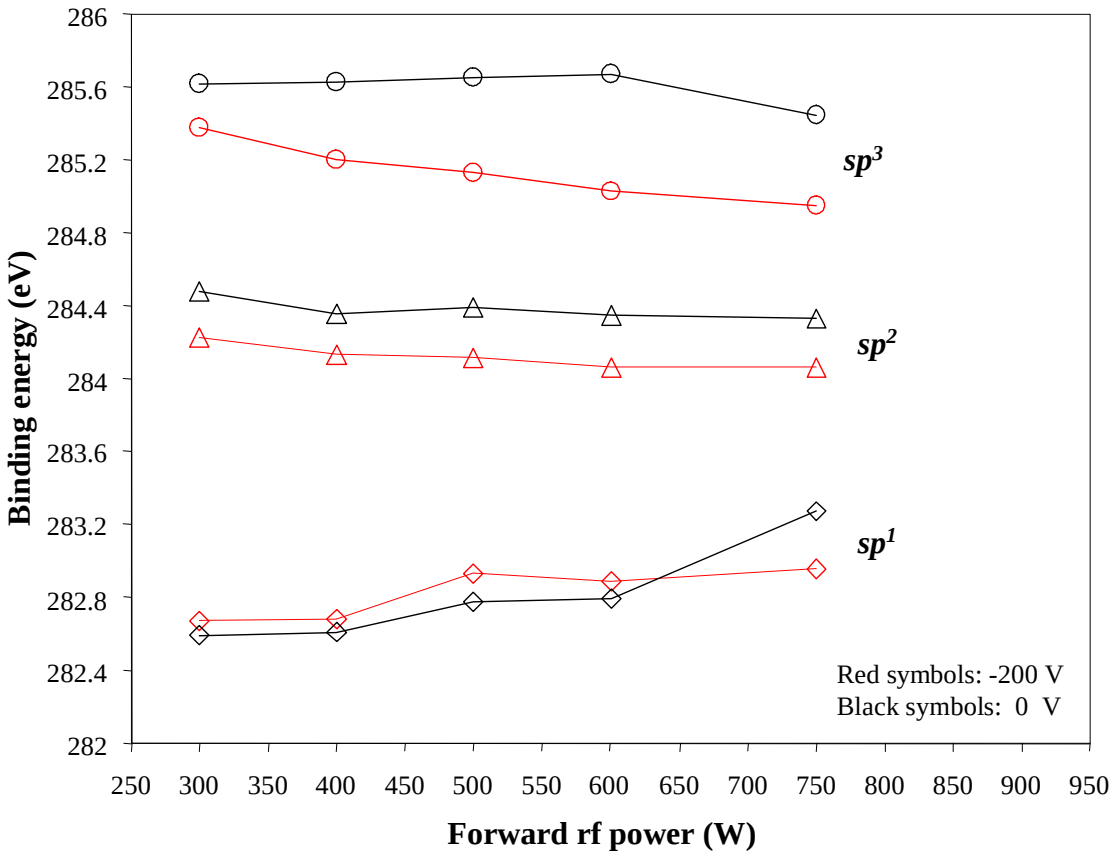

Figure 6-9 Effect of forward rf power on binding energy of sp^1, sp^2, and sp^3 for 0 and -200 V substrate bias.

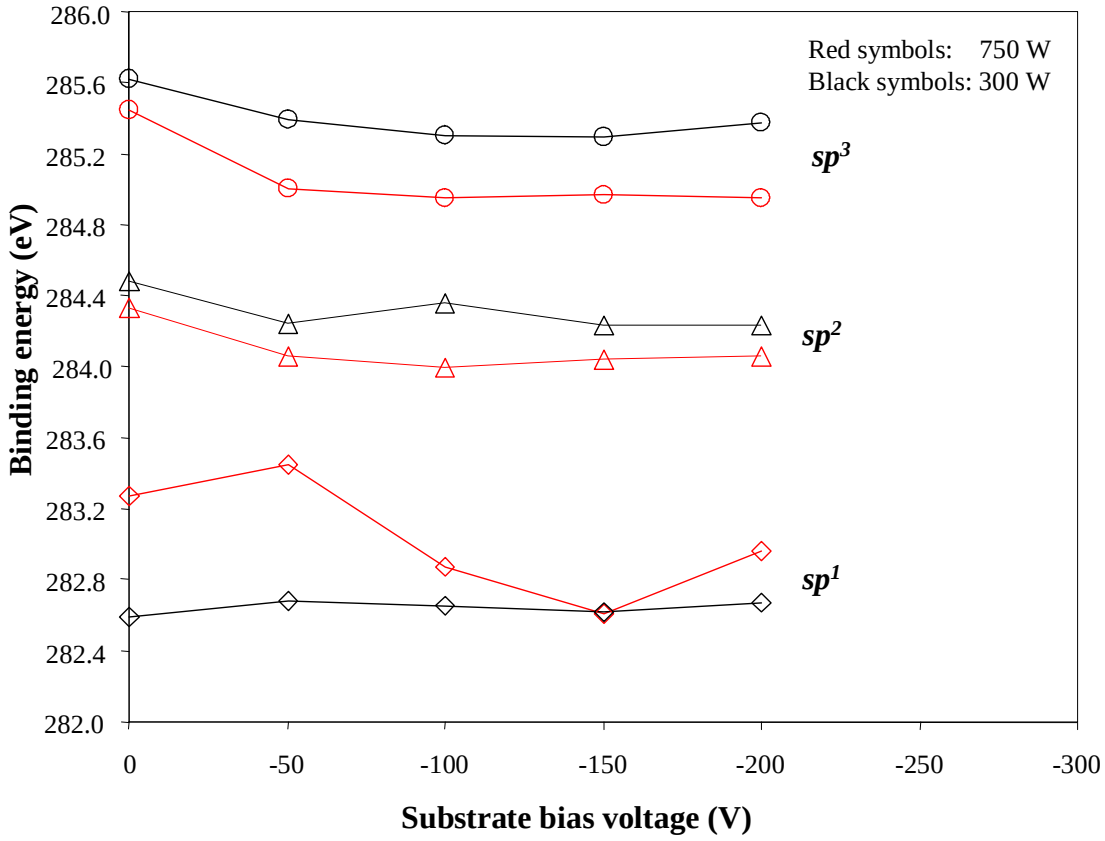

Figure 6-10 Effect of substrate bias on binding energy of sp^1, sp^2, and sp^3 for 300 and 750 W forward rf power.

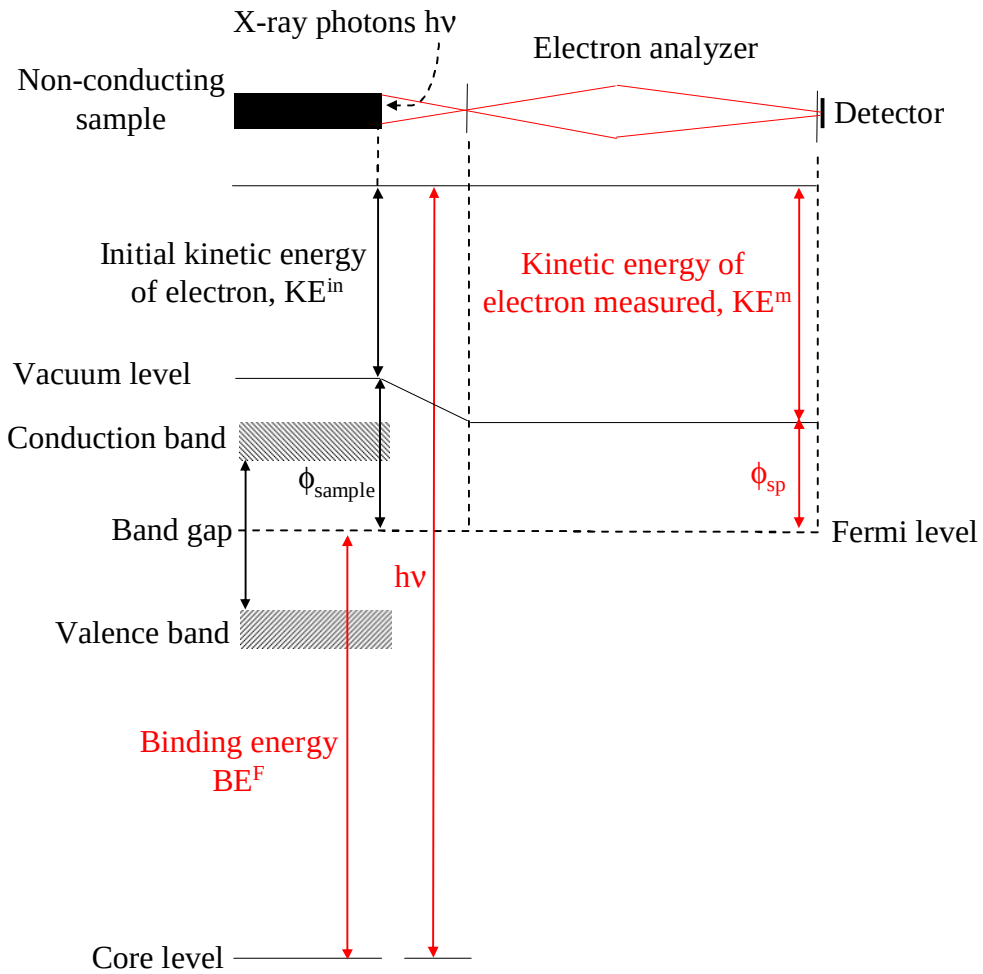

Figure 6-11 Schematic of the energy level for a non-conducting sample in electrical equilibrium with the spectrometer (Evans, 1977).

CHAPTER 7

Energetic Particle Collision Analysis of the Enhancement of Tetrahedral Carbon Hybridization in Sputtered *a*-C Films

An important characteristic of *a*-C films is the sp^3 carbon content, which depends strongly on the deposition technique and associated conditions. A common feature in tetrahedral amorphous carbon (*ta*-C) films produced from energetic carbon ions is the relatively high compressive residual stress. The formation of *ta*-C films has been examined in the context of a compressive stress model based on the pressure-temperature phase diagram of carbon (McKenzie, Muller and Pailthorp, 1991). It has been suggested that transformation from sp^2 to sp^3 occurs when the film stress exceeds a threshold value (~13 GPa) (Schwan, et al., 1997), while a stress up to 12 GPa does not necessarily result in such transformation (Lacerda, et al., 2001). However, a critical review of published experimental data has shown that the compressive residual stress cannot be directly related to the sp^3 content of *ta*-C films (Ferrari, et al., 2002). The sp^3 hybridization in *ta*-C films due to the bombardment of energetic carbon ions is a physical process that can be explained by the subplantation model (Lifshitz, Kasi and Rabalais, 1989; Lifshitz, et al., 1990; Robertson, 1994, 1996; Hofsäss, et al, 1998). The promotion of sp^3 bonding over the more stable sp^2 bonding in *ta*-C films can be interpreted in terms of a model based on the mechanisms of shallow ion implantation and relaxation. According to this model, the film cross-section shows a three-layer structure consisting of an interfacial layer, the bulk of the *ta*-C film, and a surface layer rich in sp^2 hybridization of average thickness equal to 4 and 13 Å for carbon ion energy equal to 35 and 320 eV, respectively (Davis, Amaratunga and Knowles, 1998). However, *ta*-C films synthesized by filtered cathodic

vacuum arc (FCVA) deposition and dc magnetron sputtered *a*-C films exhibited single- and three-layer structures, respectively (Ferrari, et al., 2000), which is contradictory to the theoretical prediction of the subplantation model. Therefore, it was concluded that structure layering is not an intrinsic property of *ta*-C films but a result of fluctuating deposition conditions (Ferrari, et al., 2000).

In Chapter 6, it was reported that *a*-C films with moderately high sp^3contents can also be produced by low-pressure radio-frequency (rf) sputtering without magnetron. *a*-C films with sp^3 contents as high as ~50 at.% can be deposited by applying an optimum negative bias voltage to the substrate during sputtering. Because the film precursors in rf sputtering are low-energy (~24 eV) neutral carbon atoms (section 4.4), film densification results from Ar^+ bombarding the growing film surface. The concentration of implanted Ar^+ atoms in rf sputtered *a*-C films is typically less than 3 at.% (Lu and Komvopoulos, 2000; Table 6-2), suggesting that film implantation of the heavy Ar^+ is limited. This implies that interactions between Ar^+ and carbon atoms occur mainly on the film surface, with most Ar^+ being backscattered from the surface. As a consequence, the film cross-section exhibits a two-layer structure composed of an interfacial layer and a continuous *a*-C film (sections 5.3 and 5.4). To provide additional experimental evidence for the two-layer film structure in low-pressure nonmagnetron rf sputtering with maximum Ar^+ bombardment energy of 210 eV, a high-resolution cross-sectional transmission electron microscope image of an *a*-C film deposited at 300 W forward rf power and –200 V substrate bias voltage is shown in Figure 7-1. According to the subplantation model, an approximately 10-Å-thick layer rich in sp^2 carbon should be present in the cross-sectional structure. However, only a two-layer film structure consisting of a ~32-Å-thick interfacial

layer and a ~77-Å-thick continuous *a*-C layer with 30.4 at.% sp^3 (Figure 6-7) can be seen in Figure 7-1. A similar result is found for an *a*-C film deposited at much higher forward rf power (750 W) and all other deposition conditions identical to those of the film shown in Figure 7-1. Figure 7-2 shows EELS spectra obtained from the interface, bulk (center) of the film, and near the surface of the film shown in Figure 7-1. The EELS spectrum of the interfacial layer differs from that of the bulk of the film. However, the EELS spectrum obtained near the film surface is nearly the same as that of the bulk of the film. The same conclusion is reached by comparing the EELS spectra of an *a*-C film deposited at 750 W forward rf power and –200 V substrate bias voltage. Thus, the EELS analysis also confirms the existence of a two-layer *a*-C film structure. In light of the TEM and EELS results, the statistical nature of sputtering process, and the heavy Ar^+, it may be inferred that the mechanisms of sp^3 carbon hybridization in rf sputtered *a*-C films differ significantly from those of the carbon films synthesized from highly energetic carbon ions, such as *ta*-C films produced by FCVA deposition, where the deposition conditions promote the formation of a three-layer film structure, as predicted by the subplantation model.

The development of a compressive residual stress in rf sputtered *a*-C films has been discussed in Chapter 4. Depending on the deposition conditions in the rf plasma discharge, the compressive residual stress in the *a*-C films of this study is found to be in the range of 2-11 GPa. For this stress level, stress-induced sp^2 to sp^3 transformation cannot occur according to the compressive stress model (Schwan, et al., 1997; Lacerda, et al., 2001). Therefore, the two-layer film structure and the sp^3 content in the rf sputtered *a*-C films cannot be explained based on the subplantation and compressive stress models. In

this chapter, an energetic particle collision analysis of sp^3 hybridization in rf sputtered *a*-C films id developed for conditions not conducive to high-energy particle bombardment during film growth, which result in the formation of a two-layer film structure. The underlying theory is based on collisions between Ar^+ and carbon atoms on the film surface that enhance the formation of sp^3 carbon bonding. The associated cascade collision process is a manifestation of the following sequential events:

Event A: An Ar^+ of average kinetic energy E_{Ar^+} collides with a carbon atom (C1) on the growing *a*-C film surface. In view of the low Ar concentration (< 3 at.%) (Lu and Komvopoulos, 2000, and Table 6-2 in this dissertation), the probability of this event is $P(A) \approx 1$. The kinetic energy E_{C1} gained by carbon atom C1 due to the elastic collision with the Ar^+ is proportional to E_{Ar^+}.

Event B: The carbon atom (C1) with gained kinetic energy E_{C1} due to *Event* A collides with another carbon atom (C2) at the film surface, and this collision enhances the formation of sp^3 bonding. The probability of this event $P(B|A)$ is proportional to the nuclear stopping cross-section S_n, which, in general, can be expressed as (Nastasi, Mayer and Hirvonen, 1996)

$$S_n(E_1) = \frac{C_m E_1^{1-2m}}{1-m}\left[\frac{4M_1M_2}{(M_1+M_2)^2}\right]^{1-m}, \qquad (7\text{-}1)$$

where M_1 and M_2 are the masses of the incident energetic particle and target atom, respectively, E_1 is the kinetic energy of the incident particle, and C_m is a constant that depends on the value of m. Using the Thomas-Fermi screen function, the values of m in different regions of reduced energy ε are (Winterbon, K. B., Sigmund, P. and Sanders

Winterbon, Sigmund and Sanders, 1970): $m = 1/3$ for $\varepsilon \le 0.2$, $m = 1/2$ for $0.08 \le \varepsilon \le 2$, and $m = 1$ (Rutherford scattering) for $\varepsilon \ge 10$, where ε is defined as

$$\varepsilon = \frac{M_2}{M_1 + M_2} \frac{a_{TF}}{Z_1 Z_2 e^2} E_1, \tag{7-2}$$

where Z_1 and Z_2 are the atomic numbers of the incident and target atoms, respectively, e^2 = 1.44 eV·nm, and a_{TF} is the Thomas-Fermi screening length, defined as

$$a_{TF} = \frac{0.885 a_0}{\left(Z_1^{1/2} + Z_2^{1/2}\right)^{2/3}}, \tag{7-3}$$

where a_o (= 0.05292 nm) is the Bohr radius. For a two-carbon atom collision of kinetic energy $E_{C1} < 1$ keV commencing on a sputtered *a*-C film surface, Eq. (7-2) yields $\varepsilon <$ 0.2; hence, m = 1/3. Therefore, $S_n \propto E_{C1}^{1/3}$, and because $P(B|A) \propto S_n$ and $E_{C1} \propto E_{Ar^+}$, it follows that

$$P(B|A) = kE_{Ar^+}^{1/3}, \tag{7-4}$$

where k is a proportionality factor.

Since the formation of sp^3 carbon bonding depends on the joint event $A \cap B$, the sp^3 percentage is proportional to the probability of event $A \cap B$ and the total number of collisions between Ar^+ and carbon atoms on the a-C film surface *N*. Hence,

$$\frac{sp^3}{sp^2 + sp^3} \propto NP(A \cap B), \tag{7-5}$$

where $P(A \cap B)$ can be written as

$$P(A \cap B) = P(A)P(B|A) \approx P(B|A) = kE_{Ar^+}^{1/3}. \tag{7-6}$$

The total number of collisions between Ar^+ and carbon atoms at the film surface is proportional to the sum of the fluxes of the impinging particles,

$$N \propto J_C + J_{Ar^+}, \tag{7-7}$$

where J_C and J_{Ar^+} are the fluxes of impinging neutral carbon atoms and energetic Ar^+, respectively. In view of the interdependence of these particle fluxes,

$$J_C \propto \gamma J_{Ar^+}, \tag{7-8}$$

where γ is the carbon atom sputtering yield due to Ar^+ bombarding on the pure graphite target surface. Using Eqs. (7-5) - (7-8), the sp^3 fraction is expressed as

$$\frac{sp^3}{sp^2 + sp^3} = \beta J_{Ar^+} E_{Ar^+}^{1/3}, \tag{7-9}$$

where β is a proportionality factor.

To examine the accuracy of the analytical model, thin *a*-C films are deposited on Si(100) substrates under conditions of forward rf power in the range of 298–755 W, substrate bias voltage between –50 and –200 V, working pressure of 3 mTorr, Ar gas flow rate of 20 sccm, and deposition time fixed at 3 minutes. The sp^3 content of the *a*-C films reported in section 6.5 are used to check the validity of Eq. (7-9). Figure 7-3 shows the percentage of sp^3 carbon hybridizations in the *a*-C films deposited under different conditions versus $J_{Ar^+} E_{Ar^+}^{1/3}$. The experimental data are in good agreement (correlation factor = 0.913) with the analytical results obtained from Eq. (7-9). The favorable comparison between analytical results and TEM, EELS, and XPS findings confirms that the enhancement of the sp^3 carbon hybridization in rf sputtered *a*-C films is mainly due to the energetic Ar^+ bombardment effect and confirms the validity of the analytical model derived herein.

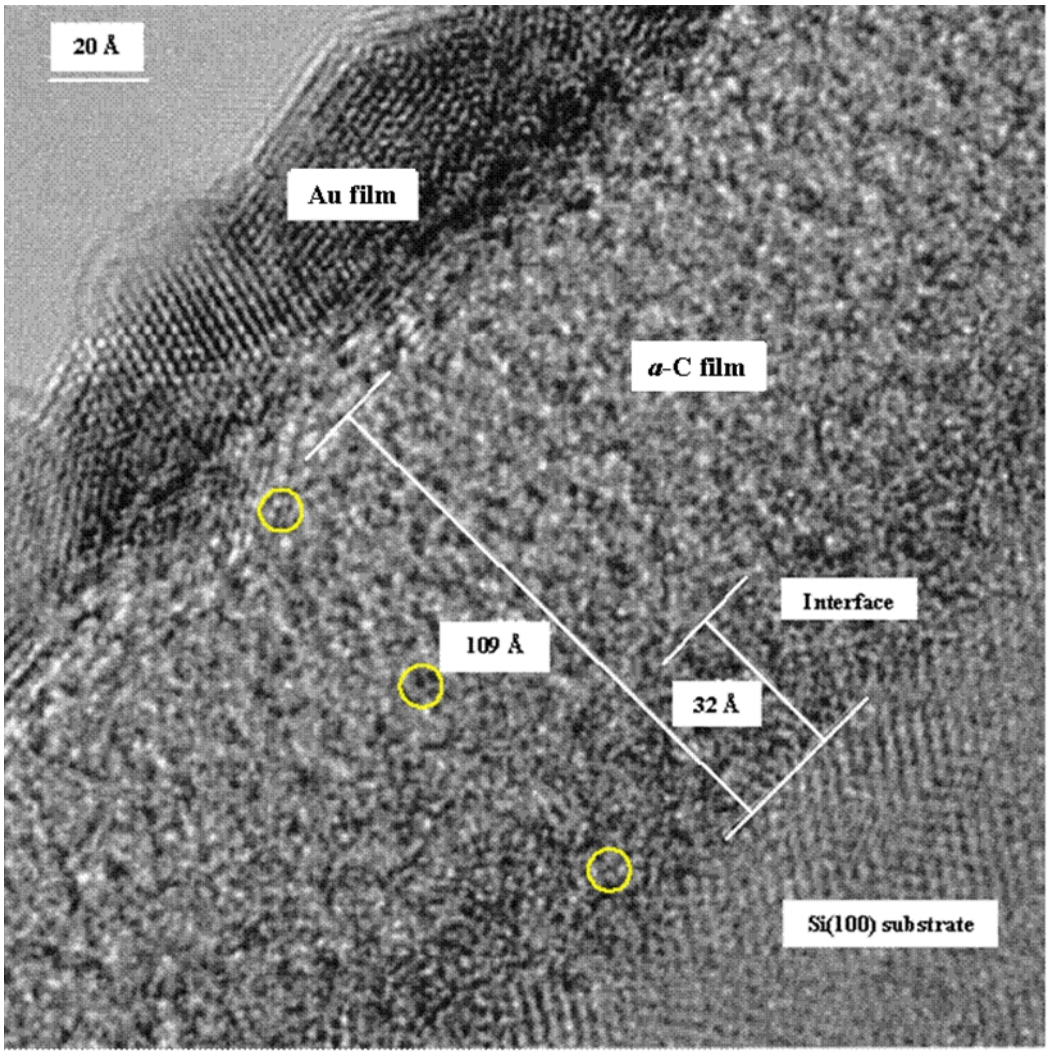

Figure 7-1 High-resolution cross-sectional transmission electron microscope image of a sputtered *a*-C film with 30.4 at.% sp^3 content deposited by rf sputtering under conditions of 300 W forward rf power, –200 V substrate bias voltage, 3 mTorr working pressure, and 20 sccm Ar gas flow rate. Open circles show the positions where the EELS spectra shown in Figure 7-2 are obtained.

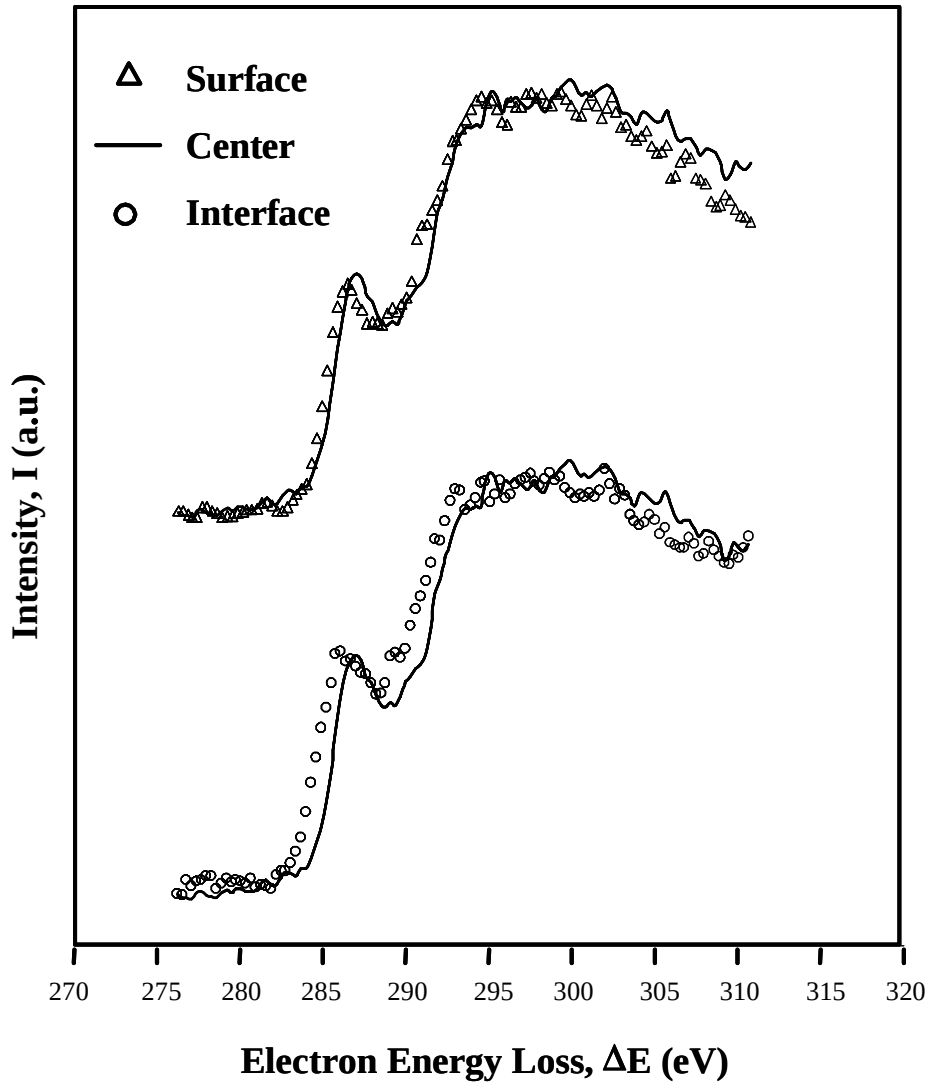

Figure 7-2 EELS spectra of the sputtered *a*-C film with 30.4 at.% sp^3 content shown in Figure 7-1. The "center" spectrum is portrayed twice superimposed on the "surface" and "interface" data sets for comparison.

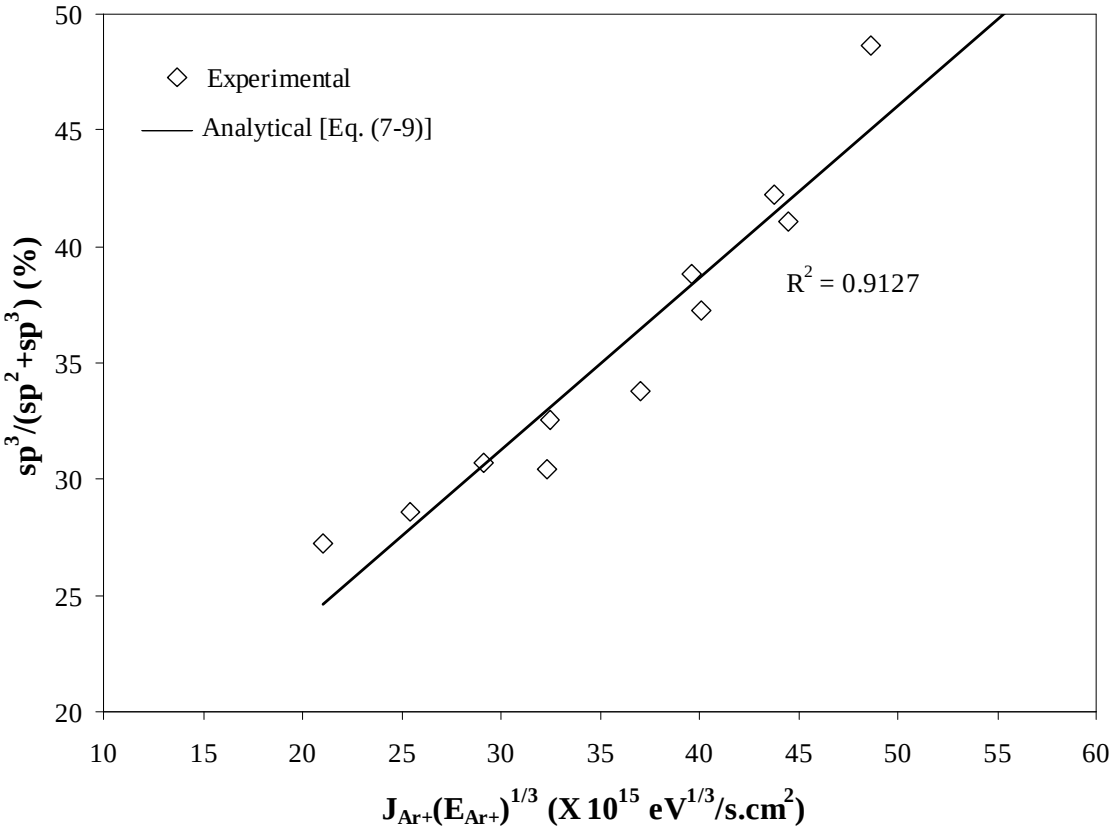

Figure 7-3 Comparison of analytical and experimental results demonstrating the dependence of the sp^3 carbon content in rf sputtered *a*-C films on the Ar^+ impinging flux J_{Ar^+} and kinetic energy E_{Ar^+}.

CHAPTER 8

Thickness Effect on Phase Transformation in Sputtered Shape Memory TiNi Films

8.1 Introduction

In previous chapters, we have discussed the deposition and characterization of sputtered *a*-C films. In this chapter, we will discuss a new topic: phase transformation in sputtered TiNi shape memory alloy thin films and the effect of constrains imposed by the film surface and layer interface.

Since the discovery of the shape memory effect (SME) in binary titanium-nickel (TiNi) alloys (Buehler, Gilfrich and Wiley, 1963), significant research effort has been devoted to the study of shape memory alloy (SMA) materials. For example, sputtered TiNi films are increasingly used in microdevices, such as microvalves, microactuators, and microgrippers, fabricated by surface micromachining. Several applications of sputtered TiNi films can be found in Proceedings of the Shape Memory and Superelasticity Technology (SMST) from 1994 through 2003. The SME in TiNi alloys is a consequence of a diffusionless transformation occurring upon cooling from the parent cubic (B2) austenite phase to the twinned monoclinic (B19′) martensite phase through the formation of an intermediate rhombohedral (R) phase and vice versa upon heating. These transformations are solely displacive because atoms are cooperatively rearranged or shifted to another crystal structure by a shear-like self-accommodation mechanism (Wang, Buehler and Pickart, 1965; Wang, 1972; Wang, Pickart and Alperin, 1972; Kudoh, et al, 1985; Miyazaki, Otsuka and Wayman, 1989). Because atom migration does not occur, this phase transformation commences at the speed of sound (Wayman and

Duerig, 1990). The R-phase (R) occurs during cooling of austenitic TiNi alloys before the start of martensite phase transformation (Dautovich and Purdy, 1965). Hence, TiNi alloys generally undergo a two-stage transformation during cooling, B2 $\rightarrow$ R $\rightarrow$ B19′ (Cai, Murakami and Otsuka, 1999). The R-phase transformation is very important because the SME is associated with this transformation (Miyazaki and Otsuka, 1984, 1986; Miyazaki, Kimura and Otsuka, 1988; Stachowiak and McCormick, 1988). Previous studies dealing with R-phase transformation have been performed on bulk TiNi alloys or sputtered TiNi films of several micrometers in thickness (Lehnert, Crevoiserat and Gotthardt, 2002). The R-phase transformation occurs in parent crystals that are not subjected to spatial constraints, such as those imposed by the film surface and/or interface with the substrate. However, R-phase transformation may be severely constrained when the film thickness is reduced to a few nanometers. Unfortunately, basic understanding of constrained R-phase transformation in ultrathin TiNi films has not yet been obtained. In this chapter, this important phenomenon is elucidated by performing experiments on sputtered nanometer-thick TiNi films and analyzing the results in terms of shear-like self-accommodation microstructure changes.

8.2 Experimental Procedures

Amorphous TiNi films are deposited on Si(100) substrates by radio-frequency (rf) sputtering without magnetron. All the films are sputtered under forward rf power of 250 W, Ar gas flow rate of 20 sccm, working pressure of 3 mTorr, and zero substrate bias voltage. The deposition time is varied in the range of 5–30 minutes to produce films of thickness between 45 and 365 nm. After deposition, the amorphous TiNi films are

crystallized by heating at ~500 °C for a few minutes and then cooled down to room temperature in a vacuum of 10^{-6} Torr. The native silicon oxide layer (~ 2–3 nm thick) on the substrate surfaces prevents interdiffusion of Si and TiNi during crystallization and insulates the TiNi films from the silicon substrate. The sputtered TiNi film thickness is obtained from the cross-sectional image of the film taken with a scanning electron microscope (LEO 1550). A four-probe experimental set-up is used to measure the film electrical resistivity ρ as a function of temperature and film thickness (Wang, et al, 1968), which represents the phase transformation in the crystallized TiNi films. Nitrogen gas through a liquid nitrogen contain is used to cool down the film temperature first. The cooling rate is controlled by adjusting the gas flow rate. After cooling, the film is heated by electricity. The heating rate is controlled by electrical power. The film temperature is monitored by a thermal couple.

8.3 R-phase Transformation in Shape Memory TiNi Alloy

As mentioned above, the R-phase (R) occurs during cooling of austenitic TiNi alloys before the commencement of martensite phase transformation (Dautovich and Purdy, 1965). TiNi alloy transforms from austenite to R-phase at a temperature R_S during cooling, in which the cubic B2 austenite phase is distorted to produce a rhombohedral R-phase, as depicted in Figure 8-1. The unit cell of the R-phase is created from the B2 cell by elongation along one of <111> directions. The lattice distortion is described by the Bain strain matrix $\mathbf{B_d}$, giving the maximum lengthening and shortening of the lattice vectors due to the R-phase transformation, in the principle axes system of

$a'[100]_d$ //$[110]_{B2}$, $b'[010]_d$ //$[\bar{1}1\bar{2}]_{B2}$, and $c'[001]_d$ //$[\bar{1}11]_{B2}$ (Miyazaki, Kimura and Otsuka, 1988)

$$\mathbf{B_d} = \begin{bmatrix} \sqrt{2\sin(\alpha/2)} & 0 & 0 \\ 0 & \sqrt{2\sin(\alpha/2)} & 0 \\ 0 & 0 & \sqrt{3-4\sin^2(\alpha/2)} \end{bmatrix}, \tag{8-1}$$

where α is the rhombohedral angle in the R-phase. Vector **X** in the parent phase changes to vector **X′** after R-phase transformation according to relationship,

$$\mathbf{X'} = \mathbf{\Phi}\,\mathbf{B_d}\,\mathbf{\Phi^t}\,\mathbf{X} \tag{8-2}$$

where

$$\mathbf{\Phi} = \begin{bmatrix} 1/\sqrt{2} & -1/\sqrt{6} & -1/\sqrt{3} \\ 1/\sqrt{2} & 1/\sqrt{6} & 1/\sqrt{3} \\ 0 & -2/\sqrt{6} & 1/\sqrt{3} \end{bmatrix}$$

and $\mathbf{\Phi^t}$ is the transpose of $\mathbf{\Phi}$. Hence, the resulting lattice strain ε (tensile or compressive) is given by

$$\varepsilon = (|\mathbf{X'}| - |\mathbf{X}|) / |\mathbf{X}|. \tag{8-3}$$

When the temperature is decreased below R_s, the rhombohedral angle α decreases. A relatively large rhombohedral distortion of approximately $\alpha = 89.5°$ was found by *in-situ* neutron diffraction studies, and the distortion increases up to $\alpha = 89°$ (Lukáš, et al, 2002). This indicts that a maximum strain of about ~1% can be obtained from the R-phase transformation. The decrease of the strain by twinning is important in the R-phase transformation because it proceeds by nucleation and growth in the parent phase crystal in a heterogeneous manner (Fukuda, et al, 1992). Therefore, the R-phase transformation

is a self-accommodating process that occurs gradually in the parent phase with the decrease of the temperature.

8.4 Unconstrained Phase Transformation in Thick TiNi Films

Figure 8-2 shows a cross-sectional image of a sputtered TiNi film obtained with a scanning electron microscope (SEM) (LEO 1550). The film thicknesses are measured directly from their cross-sectional SEM images. Figure 8-3 shows a linear dependence of film thickness on deposition time.

Figure 8-4 shows the electrical resistivity ρ versus temperature response of a 361-nm-thick austenite TiNi film subjected to a thermal cycle. The electrical resistivity decreases linearly with temperature during cooling from 150 °C due to the decrease of the intensity of electron-phonon interactions. At temperature R_s , transformation from austenite to R-phase commences in which the cubic B2 austenite phase is distorted to produce a rhombohedral R-phase, resulting a relatively large strain. As mentioned above, the decrease of the strain by twinning is important. The density of the twinned structures in the parent phase increases with the decrease of the temperature, causing an increase in the electrical resistivity (Figure 8-4). The R-phase transformation is completed when the temperature is decreased to R_f . Thus, additional twinning does not occur below R_f . Further cooling promotes transformation of the R-phase to the monoclinic B19′ martensite phase (Figure 8-5), which exhibits less lattice distortion. Therefore, the electrical resistivity decreases significantly at temperatures below R_f , which is also the martensite transformation start temperature M_s . Since the martensite phase

transformation finishes at temperature M_f, cooling below M_f does not involve additional phase transformation in the TiNi film and the electrical resistivity decreases again linearly with the temperature due to the decrease of the intensity of electron-phonon interactions (Figure 8-4).

When the TiNi film is reheated to a temperature above T_1, the monoclinic angle β in the B19′ martensite phase (Figure 8-5) changes gradually, causing a decrease in the lattice distortion. As a consequence, electron scattering due to lattice distortion decreases and the electrical resistivity increases gradually with temperature, deviating from the previous linear response. This process ends at temperature T_2. The lattice change caused by heating from T_1 to T_2 differs from that obtained by cooling from M_s to M_f, even though $T_2 \approx M_s$. This is attributed to the accumulation of less distortion in the temperature range of T_1 to T_2 than in the range of M_s to M_f. Consequently, lower electrical resistivity is obtained during heating from T_1 to T_2 than cooling from M_s to M_f. This behavior produces a temperature hysteresis in the electrical resistivity response during a thermal cycle (Figure 8-4). Increasing the temperature above T_2 does not produce additional lattice changes and, hence, the electrical resistivity increases linearly with the temperature. When the temperature is increased to A_s, detwinning commences in the TiNi film, resulting in transformation to the cubic B2 austenite parent phase, and a rapid decrease in the electrical resistivity. The austenite phase transformation finishes at temperature A_f, which is equal to R_s. At this stage, the film microstructure completely reverses to that consisting of single cubic B2 austenite phase.

Hence, transformation during heating does not involve the formation of the R-phase, i.e., $B19' \rightarrow B2$.

8.5 Constrained Phase Transformation in Thin TiNi Films

The phenomenon described above is a complete athermal phase transformation in which the transformation is not constrained by the surface and/or interface of the film because of the relatively large film thickness (361 nm). However, when the film thickness is less than a critical value, the R-phase transformation could be severely constrained by the film surface and interface with the substrate, which may affect lattice distortion and twinning significantly. The resistance force resulting from such constraint increases with the decrease of the rhombohedral angle α (i.e., increase of lattice strain) and the increase of the twinned structure density in the film. As a consequence, if the driving force for phase transformation is less than this resistance force, the transformation process ceases before the entire austenite parent phase transforms to the R-phase.

A characteristic example of the aforementioned phenomenon is shown in Figure 8-6(a) for a 192-nm-thick TiNi film. During cooling, self-accommodating R-phase transformation starts at temperature R_s. The austenite parent phase transforms to the twinned R-phase as the temperature decreases below R_s. However, R-phase transformation ceases prematurely at temperature T_3 due to the constraints introduced by the film surface and interface; thus, the electrical resistivity reaches a plateau in the temperature range from T_3 to T_4. The force responsible for the phase transformation increases with the decrease of the temperature and, eventually, overcomes the resistance force at temperature T_4, thereby enabling the phase transformation process to resume.

This is reflected by an increase in the electrical resistivity when the temperature decreases from T_4 to R_f, the temperature at which R-phase transformation finishes. Cooling below R_f ($=M_s$) leads to the transformation of the R-phase microstructure to the monoclinic B19′ martensite phase microstructure. Since this is accompanied by a decrease in the lattice distortion, the electrical resistivity decreases significantly. However, because this process is also constrained by the film surface and interface, the martensite transformation is not completed even after cooling the TiNi film down to -150 °C. Clearly, a much lower temperature is needed for full martensite transformation to occur in this film.

When the thermal cycle is reversed, angle β in the monoclinic B19′ martensite phase changes gradually resulting in a decrease in the lattice distortion. As a consequence, the effect of electron scattering due to the lattice distortion decreases and the electrical resistivity increases gradually with the temperature. This process ends and detwinning commences at temperature T_5. Thereafter, the electrical resistivity decreases with the increase of the temperature from T_5 to T_6. Detwinning during heating from T_5 to T_6 is the reverse process of the twinning encountered during cooling from T_4 to R_f. Heating above T_6 does not affect the lattice distortion and the electrical resistivity increases linearly with the temperature. When the temperature is increased to A_s, detwinning commences again accompanied by a reverse transformation to the austenite parent phase, resulting in a rapid decrease in the electrical resistivity. The TiNi microstructure completely reverses to the single austenite phase when the film is heated to temperature A_f, which is equal to R_s.

If the TiNi film is cooled down to a temperature T^* above R_f and then reheated to temperature A_f, only R-phase transformation occurs in the film. Since both lattice distortion and twinning are reversible processes in R-phase transformation, the electrical resistivity response does not exhibit a temperature hysteresis, as shown in Figure 8-6(b). However, if the film is cooled down to a temperature slightly below R_f and then reheated to A_f, a small temperature hysteresis is observed in the electrical resistivity response due to the commencement of martensite phase transformation since $R_f \approx M_S$.

Figure 8-7 shows the electrical resistivity of sputtered TiNi films of thickness equal to 147 and 47 nm subjected to the same thermal cycles as the thicker films (Figure 8-4 and Figure 8-6). A comparison of Figure 8-6(a) and Figure 8-7(a) reveals that the R-phase transformation in the 147-nm-thick TiNi film is profoundly restricted. Since the twinning process in this film is much more difficult to occur than in the 192-nm-thick film, the electrical resistivity behavior shown in Figure 8-7(a) is less influenced by the twinning process than that shown in Figure 8-6(a). For a film thickness less than 50 nm, the R-phase transformation is fully constrained by the film surface and substrate interface. Figure 8-7(b) shows that the heating path of the electrical resistivity response of the 47-nm-thick TiNi film is very similar to that shown in Figure 8-6(b) obtained during cooling, i.e., the electrical resistivity behavior does not exhibit a temperature hysteresis. As discussed previously, both lattice distortion and twinning are reversible processes in R-phase transformation. Hence, the electrical resistivity does not exhibit a temperature hysteresis when only R-phase transformation occurs in the film. The electrical resistivity response shown in Figure 8-7(b) reveals the sole occurrence of R-phase transformation in

this ultrathin film, evidently due to the high resistance force generated by the film surface and interface that prevents full R-phase transformation. As mentioned previous, the SME is associated with R-phase transformation (Miyazaki and Otsuka, 1984, 1986; Miyazaki, Kimura and Otsuka, 1988; Stachowiak and McCormick, 1988). Therefore, the SME is also restricted in this ultrathin film.

8.6 Summary

Phase transformation phenomena in sputtered shape-memory TiNi films are investigated in light of electrical resistivity measurements obtained during *in-situ* cooling and heating. It is shown that the anomalous behavior of the electrical resistivity of sputtered shape-memory TiNi films is a manifestation of lattice distortion and twinning, which are dominant mechanisms in the self-accommodating R-phase transformation and the reverse R-phase transformation. For a film thickness less than 300 nm, the film surface and interface limit the lattice distortion and twinning process, and phase transformation from austenite to martensite is inhibited in the sputtered TiNi film. This effect becomes even more pronounced as the film thickness decreases further. For sputtered TiNi films of thickness less than 50 nm, the R-phase transformation is severely constrained and, as a result, the electrical resistivity of the film does not exhibit any temperature hysteresis. The thickness effect on phase transformation may affect the materials' shape memory behavior, and play an important role on the applications of TiNi shape memory alloy thin films.

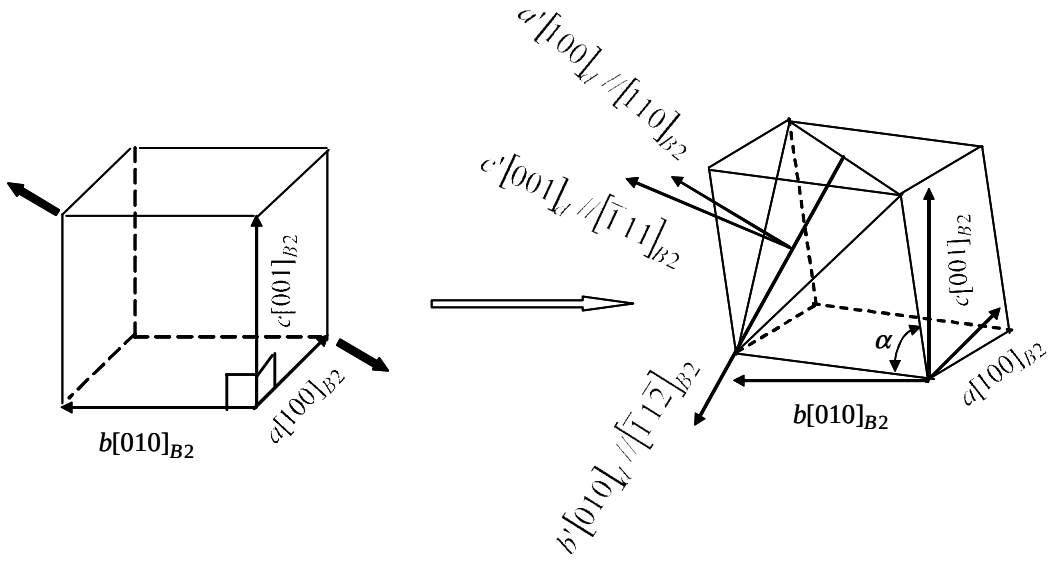

Cubic (B2) austenite phase

Rhombohedral (R) phase

Figure 8-1 Cubic (B2) austenite to rhombohedral (R) phase transformation.

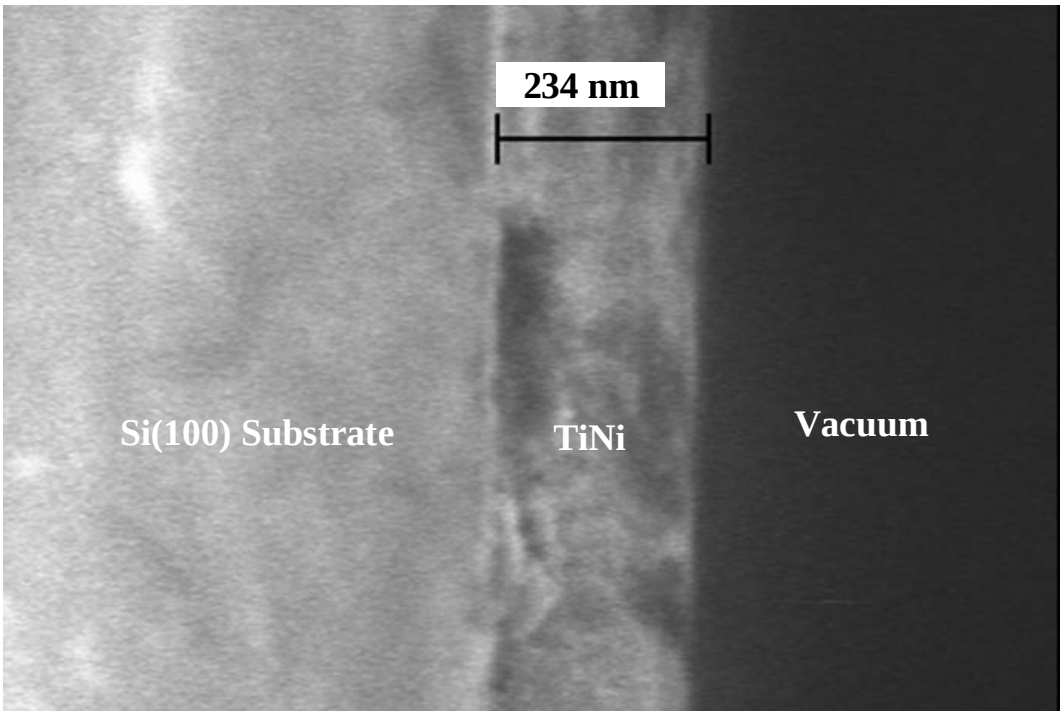

Figure 8-2 Cross-sectional scanning electron microscope image of a 234-nm-thick sputtered TiNi film synthesized under conditions of 250 W forward rf power, zero substrate bias, 20 sccm gas flow rate, 3 mTorr working pressure, and 20 minutes deposition time.

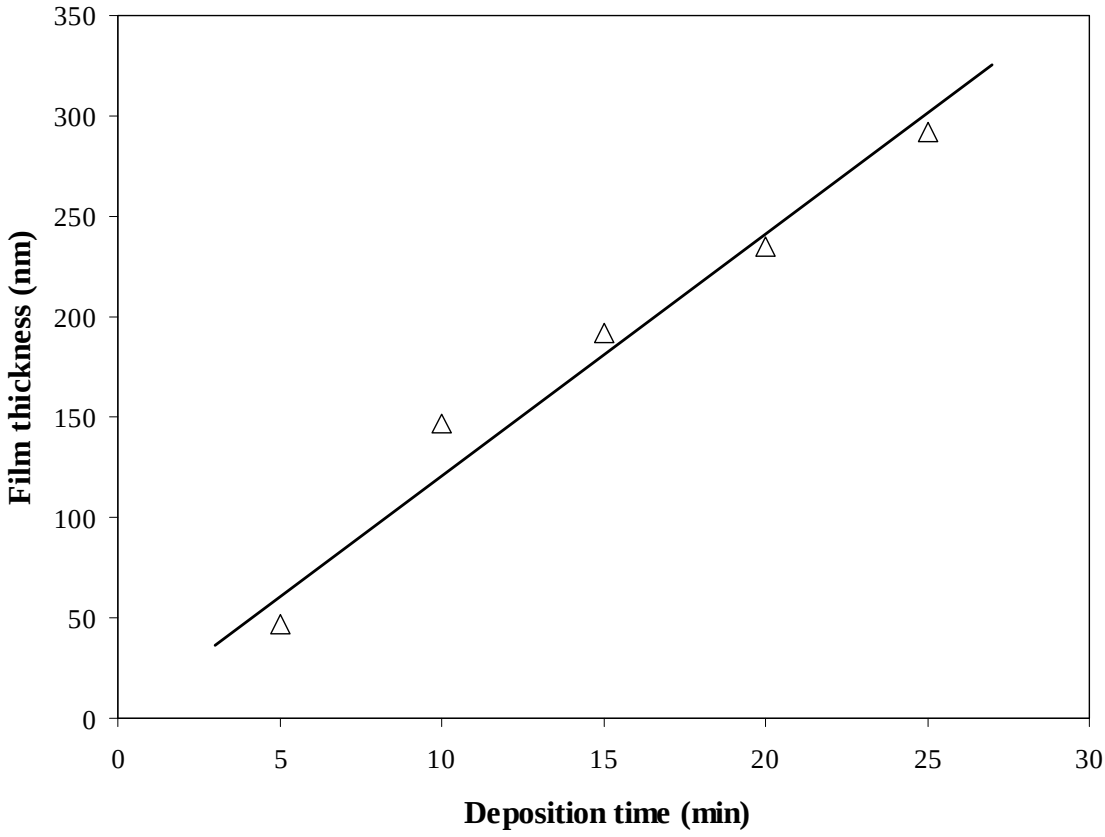

Figure 8-3 Thickness of sputtered TiNi film versus deposition time.

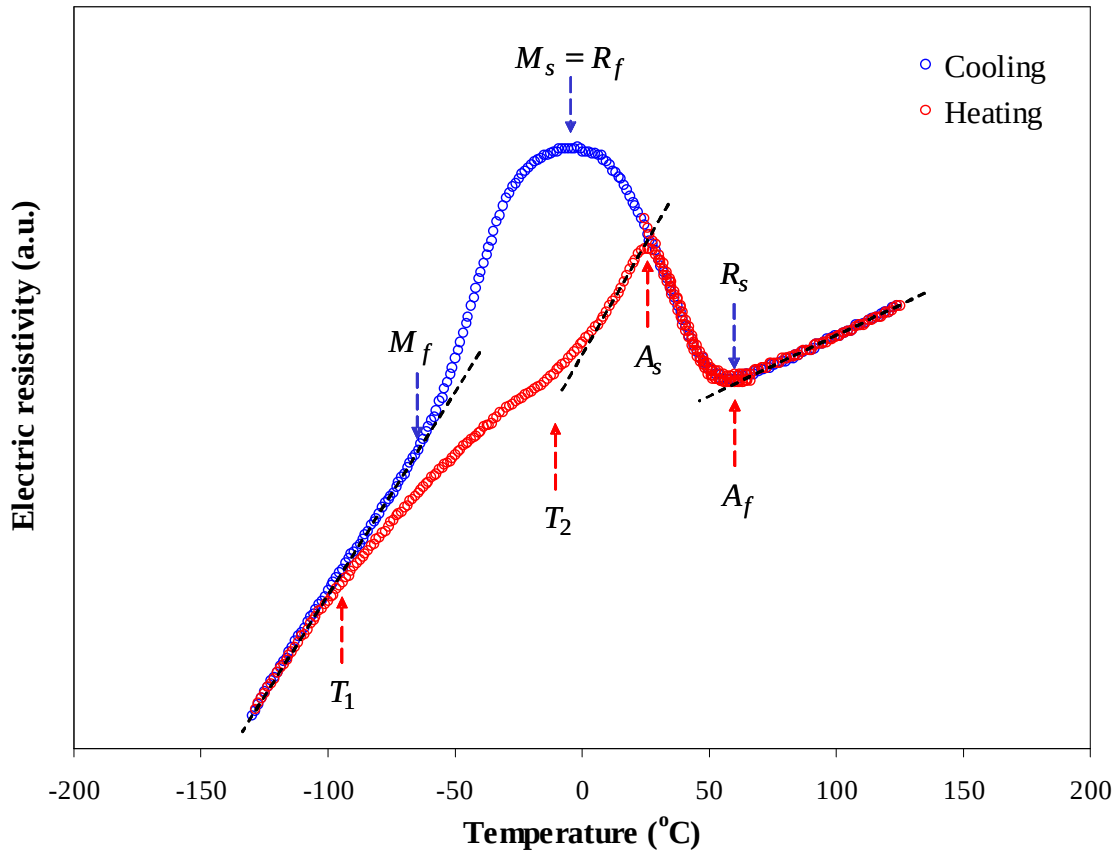

Figure 8-4 Electrical resistivity versus temperature for a 361-nm-thick sputtered TiNi film. A full phase transformation cycle occurs during this thermal cycle.

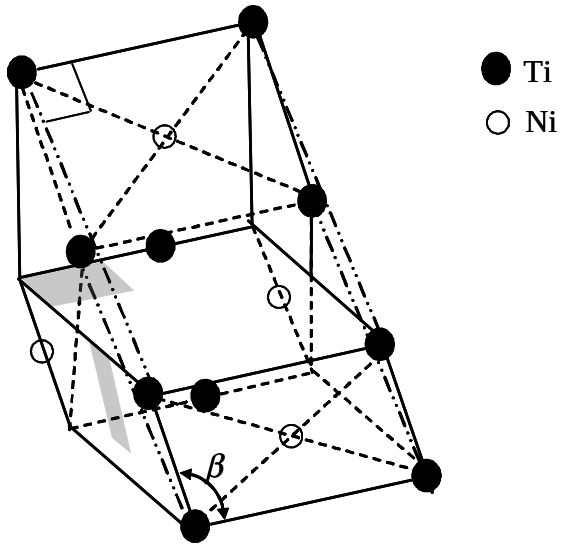

Figure 8-5 Monoclinic B19′ martensite phase.

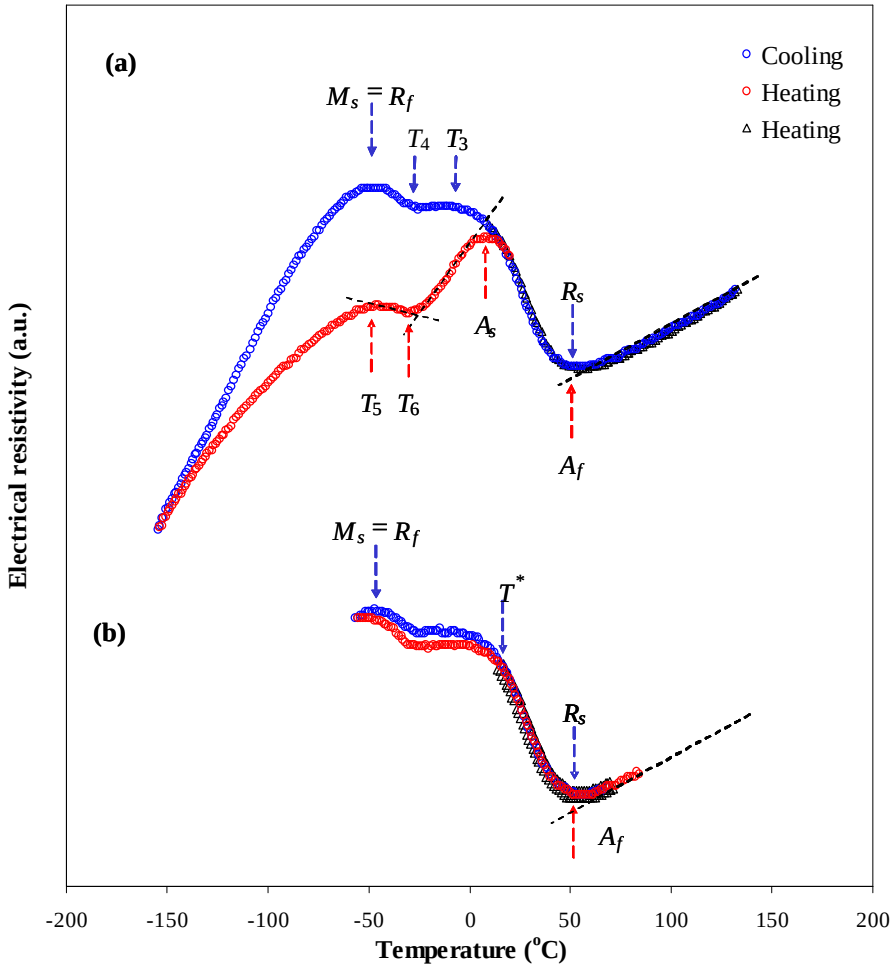

Figure 8-6 (a) Electrical resistivity versus temperature for a 192-nm-thick sputtered TiNi film showing that R-phase transformation is constrained by the film during cooling from T_3 to T_4.

(b) The electrical resistivity does not exhibit a temperature hysteresis in the temperature range of R_S to T^*. However, electrical resistivity exhibits a small temperature hysteresis in the temperature range of R_S to slightly below M_S.

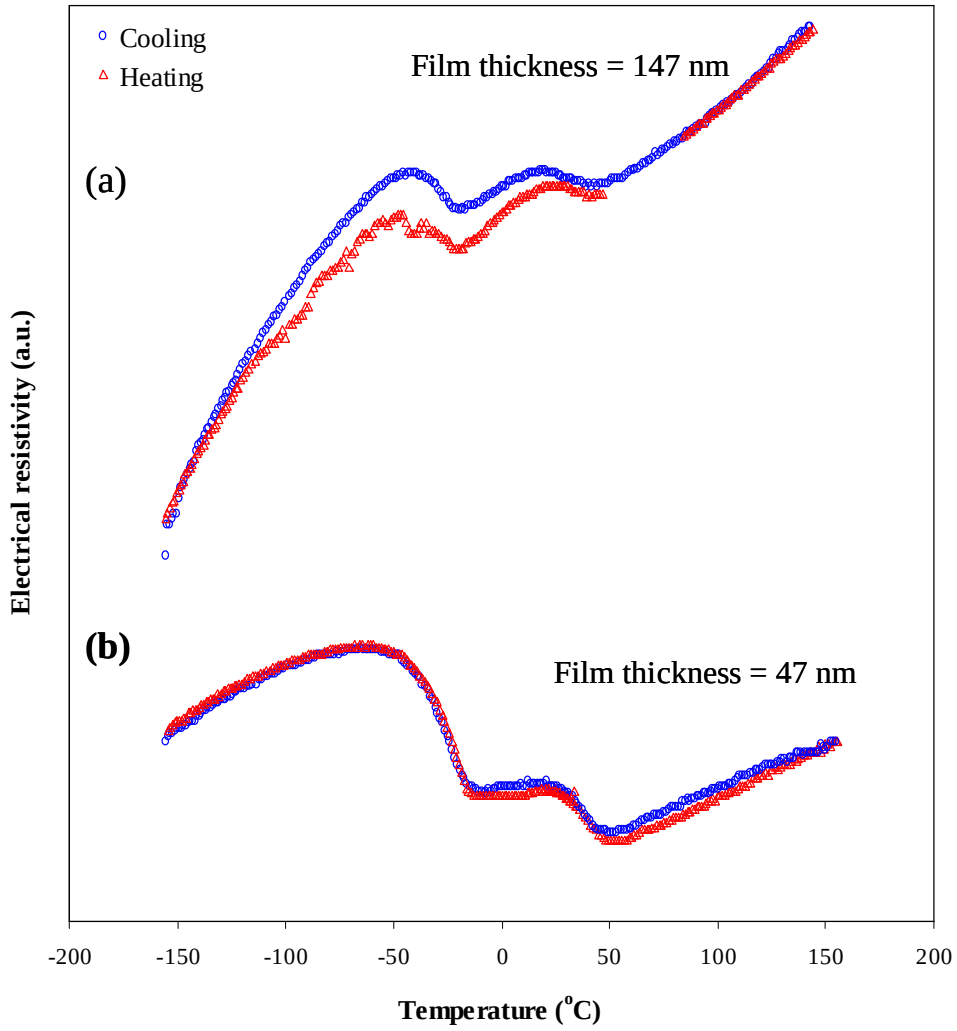

Figure 8-7 Electrical resistivity versus temperature for sputtered TiNi films of thickness (a) 147 nm and (b) 47 nm showing the constraint of R-phase transformation due to the effect of the film thickness.

CHAPTER 9

Conclusions

In this dissertation, sputtered amorphous carbon (*a*-C) and TiNi shape memory alloy thin films were synthesized using low-pressure Ar radio-frequency (rf) discharge. Plasma parameters of the film growth environment were investigated in Chapter 2. The observed effects of process conditions, such as absorbed rf power, substrate bias voltage, working pressure, and gas flow rate on the target self-bias voltage and ion current density in low-pressure rf discharge were interpreted in terms of energy balance and sheath capacitance considerations. It was shown that the Ar gas flow rate only determines the adjustable range of the working pressure and has a marginal effect on the discharge. However, the absorbed rf power, substrate bias voltage, and working pressure exhibit strong effects on the target self-bias voltage and ion current density in the discharge. The effect of low-pressure rf discharge on the growth of sputtered *a*-C film was discussed in Chapter 3. It was demonstrated that the film thickness varies linearly with the product of the sputtering rate and deposition time. There are two mechanisms contributing to film surface roughness: film growth rate and Ar^+ bombardment. In the absence of Ar^+ bombardment, the film surface roughness correlates significantly with the film growth rate. It was found that rapid film growth produces rough *a*-C film surfaces. However, Ar^+ bombardment on the growing film surface controls the surface roughness evolution. Energetic particles bombarding the growing film surface enhances the random movement of carbon atoms at the surface, hence, significantly improving the film surface roughness when the kinetic energy is ~ 200 eV.

Evaluation and relaxation of the compressive residual stresses in low-pressure rf sputtered *a*-C films were investigated by experiments presented in Chapter 4, and explained in terms of the effects of Ar^+ bombardment effect, thermal spike, and interfacial tension. It was observed that the stress level is essentially dependent on the Ar^+ kinetic energy, impinging Ar^+ flux, and duration time of the energetic particle bombardment on the growing film surface, although the stress level (~ 0.8 GPa) is independent of the Ar^+ impinging flux in the absence of Ar^+ bombardment. A compressive residual stress as high as -10 GPa may occur in the *a*-C films due to intensive Ar^+ bombardment during film growth. The origin and development of the compressive residual stress were related to Ar^+ bombardment kinetic energy and impinging flux. A film thickness dependence of the bombardment effect was found for thick films. The compressive residual stress in rf sputtered *a*-C films can relax due to thermal spike processes or the interfacial tension effects.

The examination of the cross-sectional microstructures of sputtered *a*-C films deposited on Si(100) using a high-resolution transmission electron microscope and analytical electron microscope was discussed in Chapter 5. Mass-thickness contrast in cross-sectional bright-field transmission electron microscope images and qualitative EELS analysis revealed a two-layer structure consisting of a ~35 Å thick interfacial layer and the *a*-C film. The thickness of the interfacial layer was found to be independent of the deposition conditions, confirming that the substrate surface condition controls the nucleation and initial growth of the a-C films. Mass-thickness contrast in bright-field high-resolution transmission electron microscope images showed that the density of the interface layer is greater than that of the *a*-C films. Plate-like nanocrystallites (~35 Å in

size) with {111} planes parallel to the film surface and randomly distributed in the sputtered *a*-C film were observed in high-resolution cross-sectional transmission electron microscope images. These nanocrystallites possess a diamond cubic structure. The presence of these nanocrystallites was attributed to carbon atom clusters sputtered off from the graphite target as a result of intensive Ar^+ bombarding effect, followed by epitaxial growth upon cluster deposition on the growing film surface. It was inferred that the nanocrystallite size is constrained by both the size of the carbon clusters and the deposition conditions, which are not conducive to epitaxial growth.

X-ray photoelectron spectroscopy **(**XPS) was used to systematically study the microstructures of the rf sputtered *a*-C films synthesized under different conditions in Chapter 6. Five different chemical elements, i.e., C, Ar, Si, O, and N, were detected on the *a*-C film surfaces by XPS surveys. The detected Ar atoms are incorporated into the films by the implantation process. The atomic concentration in the films was mainly determined by the Ar^+ kinetic energy, and weakly affected by the Ar^+ impinging flux. The O and N atoms were adsorbed on the *a*-C film surfaces by physisorption and chemisorption, and their atomic concentrations were significantly affected by the surface roughness. Microstructures of sputtered *a*-C films were inferred by decomposition of the corresponding C 1s core level XPS spectra using Gaussian-Lorentzian curve fits. Shifting of the binding energy positions of both sp^2 and sp^3 hybridized C atoms was observed, and related to the high compressive residual stress in the films. The percentage of sp^3 hybridized C atoms in the rf sputtered *a*-C films was described based on thermodynamic principles. The sp^3 content was significantly affected by the Ar^+ bombardment during the film growth. A simple model for energetic particle collision was present in Chapter 7 to

explain the effect of Ar^+ bombardment. The model predicts that the enhancement of sp^3 carbon hybridization in rf sputtered *a*-C films due to the Ar^+ bombardment is linearly proportional to the product of Ar^+ flux and cubic root of Ar^+ kinetic energy.

Constrained phase transformation in sputtered shape-memory TiNi alloy thin films was presented in Chapter 8. It was found that the anomalous behavior of the electrical resistivity of sputtered shape-memory TiNi alloy films during a cooling and heating is due to the effects of lattice distortion and the twinning process, which are dominant mechanisms in the self-accommodating R-phase transformation and the reverse R-phase transformation. For a film thickness less than 300 nm, the film surface and interface inhibit lattice distortion and twinning, and R-phase transformation in the sputtered TiNi alloy film is restricted. This effect becomes even more pronounced as the film thickness decreases below 300 nm. For sputtered TiNi alloy films of thickness less than 50 nm, the R-phase transformation is severely constrained and, as a result, the electrical resistivity of the films does not exhibit a temperature hysteresis. The thickness effect on phase transformation may affect the materials' shape memory behavior, and play an important role on the applications of TiNi shape memory alloy thin films.

REFERENCES

Adamson, A. W. and Gast, A. P., Ch. XVII in *Physical Chemistry oft Surfaces*, 6th ed., (John Wiley & Sons, Inc., New York, 1997).

Aisenberg, S. and Chabot, R., Ion-beam deposition of thin films of diamondlike carbon, *J. Appl. Phys.* ***42***, 2953 (1971).

Baruya, A. and Maddams, W. F., Examination of uniqueness of Gaussian and Lorentzian profiles, *Appl. Spec.* ***32***, 563 (1978).

Berger, S. D., McKenzie, D. R. and Martin, P. J., EELS analysis of vacuum arc-deposited diamond-like films, *Philos. Mag. Lett.* ***57***, 285 (1988).

Brantley, W. A., Calculated elastic constants for stress problems associated with semiconductor devices, *J. Appl. Phys.* ***44***, 534 (1973).

Brenner, A. and Senderoff, S., Calculation of stress in electrodeposits from the curvature of a plated strip, *J. Res. Natl. Bur.* ***42***, 105 (1949).

Briggs, D. and Seah, M. P.(Editors), *Practical Surface Analysis by Auger and X-ray Photoelectron Spectroscopy* (John Wiley & Sons, Inc., New York, NY, 1983).

Bruley, J., Williams, D. B., Cuomo, J. J. and Pappas, D. P., Quantitative near-edge structure analysis of diamond-like carbon in the electron microscope using a two-window method, *J. Microscopy* ***180*** *(Pt. 1)*, 22 (1995).

Buehler, W. J., Gilfrich, J. V., and Wiley, R. C., Effect of low temperature phase changes on mechanical properties of alloys near composition TiNi, *J. Appl. Phys.* ***34***, 1475 (1963).

Cai, W., Murakami, Y. and Otsuka, K., Study of R-phase transformation in a Ti-50.7at%Ni alloy by *in-situ* transmission electron microscopy observations, *Mater. Sci. Eng. A* ***273-275***, 186 (1999).

Carley, A. F. and Joyner, R. W., The application of deconvolution methods in electron spectroscopy-a review, *J. Electron Spec. Rel. Phenomena* ***16***, 1 (1979).

Chang, C. C., X-ray photoelectron and Auger analysis of thin films, *J. Vac. Sci. Technol.* ***18***, 276 (1981).

Coburn, J. W. and Kay, E., Positive-ion bombardment of substrate in rf diode glow discharge sputtering, *J. Appl. Phys.* ***43***, 4965 (1972).

Comelli, G., Stöhr, J., Robinson, C. J. and Jark, W., Structural studies of argon-sputtered amorphous carbon films by means of extended x-ray-absorption fine structure, *Phys. Rev. B* ***38***, 7511 (1988).

Dautovich, D. P. and Purdy, G. R., Phase transformations in TiNi, *Can. Metall.* ***Q4***, 129 (1965).

Davis, C. A., A simple model for the formation of compressive stress in thin films by ion bombardment, *Thin Solid Films* ***226***, 30 (1993).

Davis, C. A., Knowles, K. M. and Amaratunga, G. A. J., Cross-sectional structure of tetrahedral amorphous carbon thin films, *Surf. Coatings Technol.* ***76-77***, 316 (1995).

Davis, C. A., Amaratunga, G. A. J. and Knowles, K. M., Growth mechanism and cross-sectional structure of tetrahedral amorphous carbon thin films, *Phys. Rev. Lett.* ***80***, 3280 (1998).

D'Heurle, F. M., Aluminum films deposited by rf sputtering, *Metall. Trans.* ***1***, 725 (1970).

Díaz, J., Paolicelli, G., Ferrer, S. and Comin, F., Separation of the sp^3 and sp^2 components in the C1*s* photoemission spectra of amorphous carbon films, *Phys. Rev. B* ***54***, 8064 (1996).

Durand, H. -A, Sekine, K., Etoh, K., Ito, K and Kataoka, I., Dynamic behavior of carbon ultrathin film formation, *J. Appl. Phys.* ***84***, 2591 (1998).

Evans, S., Ch. 3 in *Handbook of X-ray and Ultraviolet Photoelectron Spectroscopy*, edited by Briggs (Heyden & Son Ltd., 1977).

Fallon, P. J., Veerasamy, V. S., Davis, C. A., Robertson, J., Amaratunga, G. A. J., Milne, W. I. and Koskinen, J., Properties of filtered-ion-beam-deposited diamondlike carbon as a function of ion energy, *Phys. Rev. B* ***48***, 4777 (1993).

Ferrari, A. C., Libassi, A., Tanner, B. K., Stolojan, V., Yuan, J., Brown, L. M., Rodil, S. E., Kleinsorge, B. and Robertson, J., Density, sp^3 fraction, and cross-sectional structure of amorphous carbon films determined by x-ray reflectivity and electron energy-loss spectroscopy, *Phys. Rev. B* ***62***, 11089 (2000).

Ferrari, A. C., Rodil, S. E., Robertson, J. and Milne, W. I., Is stress necessary to stabilise sp^3 bonding in diamond-like carbon? *Diamond Rel. Mater.* ***11***, 994 (2002).

Field, J. E., *Properties of Diamond* (Academic Press, London, UK, 1993).

Fukuda, T., Saburi, T., Doi, K. and Nenno, S., Nucleation and self-accommodation of the R-phase in Ti-Ni alloys, *Mater. Trans. JIM* ***33***, 271 (1992).

Godyak, V. A., Piejak, R. B. and Alexandrovich, B. M., Ion flux and ion power losses at the electrode sheaths in a symmetrical rf discharge, *J. Appl. Phys.* ***69***, 3455 (1991).

Hills, D. A. and Ashelby, D. W., The influence of residual stresses on contact-load-bearing capacity, *Wear* ***75***, 221 (1982).

Hoffman, D. W. and Gaertner, M. R., Modification of evaporated chromium by concurrent ion bombardment, *J. Vac. Sci. Thechnol.* ***17***, 425 (1980).

Hofsäss, H., Feldermann, H., Merk, R., Sebastian, M. and Ronning, C., Cylindrical spike model for the formation of diamondlike thin films by ion deposition, *Appl. Phys. A* ***66***, 153 (1998).

Iijima, S. H., Helical microtubules of graphitic carbon, *Nature* ***354***, 56 (1991).

Ishikawa, J., Takeiri, Y., Ogawa, K. and Takagi, T., Transparent carbon film prepared by mass-separated negative-carbon-ion-beam deposition, *J. Appl. Phys.* ***61***, 2509 (1987).

Jackson, S. T. and Nuzzo, R. G., Determining hybridization differences for amorphous carbon from the XPS C 1s envelope, *Appl. Surf. Sci.* ***90***, 195 (1995).

Jungnickel, G., Kuhn, M., Deutschmann, S., Richter, F., Stephan, U., Blaudeck, P. and Frauenheim, T., Structure and chemical bonding in high density amorphous carbon, *Diamond Rel. Mater.* ***3***, 1056 (1994).

Kelires, P. C., Gioti, M. and Logothetidis, S., Interfacial stability and atomistic processes in the *a*-C/Si(100) heterostructure system , *Phys. Rev. B 59*, 5074 (1999).

Keller, J. H. and Pennebake, W. B., Electrical properties of RF sputtering systems, *IBM J. Res. Develop.* ***23***, 3 (1979).

Kelly, B. T., *Physics of Graphite* (Applied Science Publishers, London, UK, 1981).

Kim, K. S. and Winograd, N., Charge transfer shake-up satellites in X-ray photoelectron spectra of cations and anions of $SrTiO_3$, TiO_2 and Sc_2O_3, *Chem. Phys. Lett.* ***30***, 91 (1975).

Koening, H. R. and Maissel, L. I., Application of r.f. discharges to sputtering, *IBM J. Res. Develop.* ***14***, 168 (1970).

Köhler, K, Coburn, J. W., Horne, D. E., Kay, E. and Keller, J. H., Plasma potentials of 13.56-MHz argon glow discharges in a planar system, *J. Appl. Phys.* ***57***, 59 (1985).

Köhler, K., Horne, D. E. and Coburn, J, W., Frequency dependence of ion bombardment of grounded surfaces in rf argon glow discharges in a planar system, *J. Appl. Phys.* ***58***, 3350 (1985).

Komninou, P., Nouet, G., Patsalas, P., Kehagias, T., Gioti, G., Logothetidis, S. and Karakostas, T., Crystalline structures of carbon complexes in amorphous carbon films, *Diamond Rel. Mater.* ***9***, 703 (2000).

Kovarik, P., Bourdon, E. B. D. and Prince, R. H., Electron-energy-loss characterization of laser deposited *a*-C, *a*-C:H, and diamond films, *Phys. Rev. B* ***48***, 12123 (1993).

Kudoh, Y., Tokonami, M., Miyazaki, S. and Otsuka, K., Crystal structure of the martensite in Ti-49.2 at.% Ni alloy analyzed by the single crystal X-ray diffraction method, *Acta Metall. Mater.* ***33***, 2049 (1985).

Lacerda, R. G., Hammer, P., Lepienski, C. M., Alvarez, F. and Marques, F. C., Hard graphitic-like amorphous carbon films with high stress and local microscopic density, *J. Vac. Sci. Technol. A* ***19,*** 971(2001).

Lehnert, T., Crevoiserat, S. and Gotthardt, R., Transformation properties and microstructure of sputter-deposited Ni-Ti shape memory alloy thin films, *J. Mater. Sci.* ***37***, 1523 (2002).

Lieberman, M. A., Analytical solution for capacitive RF sheath, *IEEE Trans. Plasma Sci.* ***16***, 638 (1988).

Lieberman, M. A. and Lichtenberg, A. J., *Principles of Plasma Discharges and Materials Processing* (John Wiley & Sons, Inc., New York, 1994).

Lifshitz, Y., Kasi, S. R. and Rabalais, J. W., Subplantation model for film growth from hyperthermal species: Application to diamond, *Phys. Rev. Lett.* ***62***, 1290 (1989).

Lifshitz, Y., Kasi, S. R., Rabalais, J. W. and Eckstein, W., Subplantation model for film growth from hyperthermal species, *Phys. Rev. B* ***41***, 10468 (1990).

Lifshitz, Y., Hydrogen-free amorphous carbon films: correlation between growth conditions and properties, *Diamond Rel. Mater.* ***5***, 388 (1996).

Lifshitz, Y., Lempert, G. and Grossman, E., Substantiation of subplantation model for diamondlike film growth by atomic force microscopy, *Phys. Rev. Lett.* ***72***, 2753 (1997).

Lifshitz, Y., in *The Physics of Diamond*, edited by Paoletti and Tucciarone (IOS, Amsterdam, Netherlands, 1997), pp. 209-235.

Lifshitz, Y., Diamond-like carbon—present status, *Diamond Rel. Mater.* ***8***, 1659 (1999).

Lioutas, CB., Vouroutzis, N., Logothetidis, S. and Lefakis, H., Transmission electron microscopy investigation of the structural characteristics of amorphous tetrahedral carbon films, *Thin Solid Films* ***319***, 144 (1998).

Logothetidis, S. and Stergioudis, G., Studies of density and surface roughness of ultrathin amorphous carbon films with regards to thickness with x-ray reflectometry and spectroscopic ellipsometry, Appl. Phys. Lett. **71**, 2463 (1997).

Logothetidis, S., Gioti, M. and Patsalas, P., Real-time monitoring, growth kinetics and properties of carbon based materials deposited by sputtering, *Diamond Rel. Mater.* ***10***, 117 (2001).

Lu, W. and Komvopoulos, K., Microstructure and nanomechanical properties of nitrogenated amorphous carbon thin films synthesized by reactive radio frequency sputtering, *J. Appl. Phys.* ***85***, 2642 (1999).

Lu, W. and Komvopoulos, K., Dependence of growth and nanomechanical properties of ultrathin amorphous carbon films on radio frequency sputtering conditions, *J. Appl. Phys.* ***86***, 2268 (1999).

Lu, W. and Komvopoulos, K., Implanted argon atoms as sensing probes of residual stress in ultrathin films, *Appl. Phys. Lett.* ***76***, 3206 (2000).

Lu, W. and Komvopoulos, K., Stability of ultrathin amorphous carbon films deposited on smooth silicon substrates by radio frequency sputtering, *J. Appl. Phys.* ***89***, 2422 (2001).

Lu, W. and Komvopoulos, K., Nanotribological and nanomechanical properties of ultrathin amorphous carbon films synthesized by radio frequency sputtering, *ASME J. Tribol.* ***123***, 641 (2001).

Lukáš, P., Šittner, P., Lugovoy, D., Neov, D. and Ceretti, M., In situ neutron diffraction studies of the R-phase transformation in the TiNi shape memory alloy, *Appl. Phys. A* ***74****[Suppl.]*, S1121 (2002).

Ma, X.-G., Komvopoulos, K, Wan, D., Bogy, D. B. and Kim, Y.-S., Effects of film thickness and contact load on nanotribological properties of sputtered amorphous carbon thin films, *Wear* ***254***, 1010 (2003).

Machlin, E. S., *Materials Science in Microelectronics, The Relationships between Thin Film Processing and Structure* (Giro Press, Croton-on-Hudson, New York, 1995).

Maddams, W. F., The scope and limitations of curve fitting, *Appl. Spec.* ***34***, 245 (1980).

Manenschijn, A., Janssen, G. C. A. M., van der Drift, E. and Radelaar, S., Measurement of ion impact energy and ion flux at the rf electrode of a parallel plate reactive ion etcher, *J. Appl. Phys.* ***69***, 1253 (1991).

Matsunami, N, Yamamura, Y., Itikawa, Y., Itoh, N., Kazumata, Y., Miyagawa, S., Morita, K., Shimizu, R. and Tawara, H., Energy dependence of the ion-induced sputtering yields of monatomic solids, *Atomic Data and Nuclear Data Tables* ***31*** (no. 1), 1 (1984).

Mcdaniel, E. W., *Collision Phenomena in Ionized Gases* (John Wiley & Sons, Inc., New York, 1964).

McKenzie, D. R., Muller, D. and Pailthorpe, B. A., Compressive-stress-induced formation of thin film tetrahedral amorphous carbon, *Phys. Rev. Lett.* ***67***, 773 (1991).

McKenzie, D. R., Tetrahedral bonding in amorphous carbon, *Rep. Prog. Phys.* ***59***, 1611 (1996).

Mérel, P., Tabbal, M., Chaker, M., Moisa, S. and Margot, J., Direct evaluation of the sp^3 content in diamond-like-carbon films by XPS, *Appl. Surf. Sci.* ***136***, 105 (1998).

Metze, A., Ernie, D. W. and Oskam, H. J., Application of the physics of plasma sheaths to the modeling of rf plasma reactors, *J. Appl. Phys.* ***60***, 3081 (1986).

Miller, P. A. and Riley, M. E., Dynamics of collisionless rf plasma sheaths, *J. Appl. Phys.* ***82***, 3689 (1997).

Miyazaki, S. and Otsuka, K., Mechanical behaviour associated with the premartensitic rhombohedral-phase transition in a $Ti_{50}Ni_{47}Fe_3$ alloy, *Phil. Mag. A* ***50***, 393 (1984).

Miyazaki, S. and Otsuka, K., Deformation and transition behavior associated with the R-phase in Ti-Ni alloys, *Metall. Trans. A* ***17***, 53 (1986).

Miyazaki, S., Kimura, S. and Otsuka, K., Shape-memory effect and pseudoelasticity associated with the R-phase transition in Ti-50.5 at.%Ni single crystals, *Phil. Mag. A* ***57***, 467 (1988).

Miyazaki, S., Otsuka, K. and Wayman, C. M., The shape memory mechanism associated with the martensitic transformation in Ti-Ni alloys. I. Self-accommodation, *Acta Metall. Mater.* ***37***, 1873 (1989).

Miyazaki, S., Otsuka, K. and Wayman, C. M., The shape memory mechanism associated with the martensitic transformation in Ti-Ni alloys. II. Variant coalescence and shape recovery, *Acta Metall. Mater.* ***37***, 1885 (1989).

Moulder, J. M., Stickle, W. F., Sobol, P. E. and Bomben, K. D., Introduction in *Handbook of X-ray Photoelectron Spectroscopy* (Physical Electronics, Inc., Minnesota, 1995).

Mounier, E., Juliet, P., Quesnel, E. and Pauleau, Y., Dependence of tribological properties on deposition parameters for non hydrogenated amorphous carbon films produced by magnetron sputtering, *Surf. Coating Technol.* ***77***, 548 (1995).

Mounier, E. and Pauleau, Y., Effect of energetic particles on the residual stresses in nonhydrogenated amorphous carbon films deposited on grounded substrates by dc magnetron sputtering, *J. Vac. Sci. Thechnol. A* ***14***, 2535 (1996).

Mounier, E., and Pauleau, Y., Mechanisms of intrinsic stress generation in amorphous carbon thin films prepared by magnetron sputtering, *Diamond Rel. Mater.* ***6***, 1182 (1997).

Nastasi, M., Mayer, J. W. and Hirvonen, J. K., Ch. 5 in *Ion-Solid Interactions: Fundamentals and Applications* (Cambridge University Press, Cambridge, UK, 1996).

Nix, W. D., Mechanical properties of thin films, *Metall. Trans. A* ***20A*** 2217 (1989).

Ohring, M., *The Materials Science of Thin Films* (Academic Press, Boston, MA, 1992), Ch. 2.

Panagopoulos, T. and Economou, D. J., Plasma sheath model and ion energy distribution for all radio frequency, *J. Appl. Phys.* ***85***, 3435 (1999).

Pennebake, W. B., Influence of scattering and ionization on RF impedance of glow discharge sheaths, *IBM J. Res. Develop.* ***23***, 16 (1979).

Power, C. J. and Seah, M. P., Precision, accuracy, and uncertainty in quantitative surface analyses by Auger-electron spectroscopy and X-ray photoelectron spectroscopy, *J. Vac. Sci. Technol. A* ***8***, 735 (1990).

Proctor, A. and Sherwood, P. M., Data-analysis techniques in x-ray photo-electron spectroscopy, *Anal. Chem.* ***54***, 13 (1982).

Ramírez, A. G., Itoh, T. and Sinclair, R., Crystallization of amorphous carbon thin films in the presence of magnetic media, *J. Appl. Phys.* ***85***, 1508 (1999).

Robertson, J., Amorphous carbon, Adv. *Phys.* ***35***, 317 (1986).

Robertson, J., Mechanical properties and coordinations of amorphous carbons, *Phys. Rev. Lett.* ***68***, 220 (1992).

Robertson, J., The deposition mechanism of diamond-like a-C and a-C:H, *Diamond Rel. Mater.* ***3***, 361 (1994).

Robertson, J., Deposition mechanism of cubic boron nitride, *Diamond Rel. Mater.* ***5***, 519 (1996).

Robertson, J., Diamond-like amorphous carbon, *Mater. Sci. Eng.* ***R37***, 129 (2002).

Rohlfing, E. A., Cox, D. M., Kaldor, K. J., Production and characterization of supersonic carbon cluster beams, *J. Chem. Phys.* ***81***, 3322 (1984).

Ronning, C., Dreher, E., Thiele, J. –U., Oelhafen, P. and Hofsäss, H., Electronic and atomic structure of undoped and doped ta-C films, *Diamond Rel. Mater.* ***6***, 830 (1997).

Schafer, J., Ristein, J., Graupner, R., Ley, L., Stephann, U., Frauenheim, Th., Veerasamy, V. S., Amaratunga, G. A. J., Weiler, M. and Ehrhardt, H., Photoemission study of

amorphous carbon modifications and comparison with calculated densities of states, *Phys. Rev. B* ***53***, 7762 (1996).

Schwan, J., Ulrich, S., Theel, T., Roth, H., Ehrhardt, H., Becker, P. and Silva, S. R. P., Stress-induced formation of high-density amorphous carbon thin films, *J. Appl. Phys.* ***82***, 6024 (1997).

Seitz, F. and Koehler, J. S., *Solid State Phys.* ***3***, 305 (1956).

Sherwood, P. M., Appendix 3 in *Practical Surface Analysis by Auger and X-ray Photoelectron Spectroscopy*, edited by Briggs and Seah (John Wiley & Sons, Inc., New York, 1983).

Shirley, D. A., High-resolution x-ray photoemission spectrum of the valence bands of gold, *Phys. Rev. B* ***5***, 4709 (1972).

Siegbahn, K., Nordling, C., Fahlman, A., Nordberg, R., Hamrin, K., Hedman, J., Johansson, G., Bergmark, T., Karlsson, S.-E., Lindgren, I. and Lindberg, B., *ESCA – Atomic, Molecular and Solid State Structure Studies by Means of Electron Spectroscopy* (Almqvist and Wiksells, Uppsala, Sweden, 1967).

Siegbahn, K., Nordling, C., Johansson, G., Hedman, J., Heden, P. F., Hamrin, K., Gelius, U., Bergmark, T., Werme, L. O., Manne, R. and Baer, T., *ESCA Applied to Free Molecules* (North Holland, Amsterdam, Netherlands, 1969).

Sigmund, P., Theory of sputtering. I. Sputtering yield of amorphous and polycrystalline targets, *Phys. Rev.****184***, 383 (1969).

P. Sigmund, Ch. 2 in *Sputtering by Particle Bombardment I*, edited by R. Behrisch (Springer, Berlin, Germany, 1981).

Silva, S. R. P., Xu, S., Tay, B. X., Tan, H. S. and Milne, W. I., Nanocrystallites in tetrahedral amorphous carbon films, *Appl. Phys. Lett.* ***69***, 491 (1996).

Smith, D. L., *Thin-Film Deposition: Principles and Practice* (McGraw-Hill, New York, 1995), Ch. 8 & 9.

Somorjai, G. A., *Principles of Surface Chemistry* (Prentice-Hall, Englewood Cliffs, NJ, 1972), p. 102.

Stachowiak, G. B. and McCormick, P. G., Shape memory behaviour associated with the R and martensitic transformations in a NiTi alloy, *Acta Metall. Mater.* ***36***, 291 (1988).

Taki, Y. and Takai, O., XPS structural characterization of hydrogenated amorphous carbon thin films prepared by shielded arc ion plating, *Thin Solid Films* ***316***, 45 (1998).

Tay, B. K., Shi, X., Tan, H. S. and Chua, D. H. C., Investigation of tetrahedral amorphous carbon films using X-ray photoelectron and Raman spectroscopy, *Surf. Interface Anal.* ***28***, 231 (1999).

Tsai, H. and Bogy, D. B., Characterization of diamondlike carbon films and their application as a overcoats on thin film media for magnetic recording, *J. Vac. Sci. Technol. A* ***5***, 3287 (1987).

Thompson, M. W., Energy spectrum of ejected atoms during high energy sputtering of gold, *Philos. Mag.* ***18***, 377 (1968).

Wang, F. E., Buehler, W. J. and Pickart, S. J., Crystal structure and a unique ``Martensitic'' transition of TiNi, *J. Appl. Phys.* ***36***, 3232 (1965).

Wang, F. E., DeSavage, B. F., Buehler, W. J. and Hosler, W. R., The irreversible critical range in the TiNi transition , *J. Appl. Phys.* ***39***, 2166 (1968).

Wang, F. E., Transformation twinning of *B*2(CsCl)-type structure based on an inhomogeneous shear model , *J. Appl. Phys.* ***43***, 92 (1972).

Wang, F. E., Pickart, S. J. and Alperin, H. A., Mechanism of the TiNi martensitic transformation and the crystal structures of TiNi-II and TiNi-III phases, *J. Appl. Phys.* ***43***, 97 (1972).

Wayman, C. M. and Duerig, T. W., in *Engineering Aspects of Shape Memory Alloys*, edited by Duerig, Melton, Stoeckel and Wayman (Butterworth-Heinemann, London, UK, 1990), pp. 3-20.

Westwood, W. D., Calculation of deposition rates in diode sputtering systems, *J. Vac. Sci. Thechnol.* ***15***, 1 (1978).

Williams, D. B. and Carter, C. B., *Transmission Electron Microscopy I: Basics* (Plenum, New York, 1996).

Williams, D. B. and Carter, C. B., *Transmission Electron Microscopy II: Diffraction* (Plenum, New York, 1996).

Williams, D. B. and Carter, C. B., *Transmission Electron Microscopy III: Imaging* (Plenum, New York, 1996).

Williams, D. B. and Carter, C. B., *Transmission Electron Microscopy IV: Spectrometry* (Plenum, New York, 1996).

Windischmann, H., An intrinsic stress scaling law for polycrystalline thin films prepared by ion beam sputtering, *J. Appl. Phys.* ***62***, 1800 (1987).

Windischmann, H., Intrinsic stress in sputter-deposited thin films, *Crit. Rev. Solid State Mater. Sci.* ***17***, 547 (1992).

Winterbon, K. B., Sigmund, P. and Sanders, J. B., Spatial distribution of energy deposited by atomic particles in elastic collisions, *Mat. Fys. Medd. Dan Vid. Selsk.* ***37***, 1 (1970).

Ye, N., Ch. 5 in *Contact Mechanics of Elastic-Plastic Layered Media With Smooth and Rough Surfaces* (*Dissertation*) (UC, Berkeley, 2002).

Yuan, J., Saeed, A., Brown, L. M. and Gaskell, P. H., The structure of highly tetrahedral amorphous diamond-like carbon. 3. Study of inhomogeneity by high-resolution inelastic scanning-transmission electron-microscopy, *Philos. Mag. B* ***66***, 187 (1992).